Università Politecnica delle Marche
Scuola di Dottorato di Ricerca in Scienze dell'Ingegneria
Corso di Dottorato in Ingegneria Industriale

Problems in measurement of mechanical loads in wind turbines: bending/torsional moments by strain gage bridges and torque by optical transducer

Ph.D. Dissertation of:

Ing. Matteo Bezziccheri

Supervisor:

Prof. Nicola Paone

Assistant Supervisor:

Dr. Christopher James Crabtree

Ph.D. Course coordinator:

Prof. F. Mandorli

XVI edition - new series

Dedicated to

Alice and my family

Abstract

The analysis of mechanical loads today plays a crucial role in the certification of wind turbines (WT). Similarly, mechanical loads measurement is relevant for condition monitoring of wind turbines; as rapid detection of abnormal loads can help preventative maintenance with a direct impact on machine operation and maintenance (O&M) costs. This thesis discusses the complexity of measuring mechanical loads on HAWT wind turbines.

The most important mechanical loads on a wind turbine are bending and torsional moments that are usually measured through strain gage full bridges, as recommended by the standard IEC 61400-13.

This thesis at first discusses the guidelines for the design the strain gage measurement chain, comparing the possible configurations of the full strain gage bridges (parallel or T), as well as the possible electrical connection (4 wires or 6 wires) and showing a typical configuration of the network of DAQ systems. Next, a comparison among the different calibration procedures, analytical, external loads and gravity, is presented. The gravity calibration is often the recommended solution. This work presents static-dynamic models, which allow to calibrate the full strain gage bridges using its own imbalanced masses, and comments on the attainable range of calibration, which is rather limited with respect to expected load range in operation. For each model, an uncertainty analysis of the calibration process will be presented, according to the ISO/IEC Guide 98-3: 2008 "Guide to the Expression of Uncertainty in Measurement".
Even if measurement should take place in isothermal effects, this is not always the case in real world practice. Therefore, the thermal effects on strain gage bridges are also discussed, putting into evidence its influence on calibration and signal uncertainty both for full bridges in T configuration and in parallel configuration.

Among the strain gage measurements that can be performed on wind turbines, the torque measurement on the shaft is often the most uncertain because it is affected by strong crosstalk phenomena. However, many studies have shown that an accurate torque measurement can provide much information about the WT's health and it has been shown to be a successful method for detecting faults in the main drive train components. Although WT torsional effects are important, torque measurement on wind turbine shaft is a complex task today; the available solutions are uncertain (like strain gage) or invasive (like inline torque sensor).

This thesis, in its second part, analyses a novel, contactless torque measurement system consisting of two shaft-mounted zebra tapes and two optical sensors mounted on stationary rigid supports. Unlike conventional torque measurement methods, the system, initially proposed by Durham University, does not require

costly embedded sensors or shaft-mounted electronics. The performance of the system has been analyzed experimentally on a small scale laboratory test bench under both static and dynamic conditions; the technique has been implemented using two different signal processing methods, rising edge and cross-correlation approaches. The results show good agreement with reference measurements from an in-line, invasive torque transducer. The uncertainty according to the ISO/IEC Guide 98-3: 2008 "Guide to the Expression of Uncertainty in Measurement" is shown to be ±0.3% and ±0.8% of full-scale torque for the rising edge and cross-correlation approaches, respectively. Finally, a feasibility analysis and a system scale-up design for two typical WTs with different shaft configurations, 60 kW wind turbine with gearbox and 3 MW wind turbine with direct drive train, has been performed. The expected uncertainty for the two solutions is 2.0% and 0.5%, respectively.

Sommario

L'analis di carichi meccanici svolge oggi un ruolo cruciale nella certificazione di turbine eoliche (WT). Allo stesso modo, la misura dei carichi meccanici è rilevante per monitorare le condizioni di turbine eoliche; poiché, tramite un rilevamento rapido di carchi insoliti, è possibile adottare una manutenzione preventiva con un impatto diretto sulle spese di funzionamento e manutenzione (O&M) della macchina. Questo lavoro discute la complessità di misurare carichi meccanici su grandi turbine eoliche.

I carichi meccanici di maggior rilievo su una turbina eolica sono momenti flettenti e torcenti che, in accordo con lo standard IEC 61400-13, è consigliabile misurare attraverso ponti estensimetrici interi.

Questa tesi all'inizio discute le linee guida per la progettazione della catena di misura estensimetrica, confrontando le possibili configurazioni dei ponti estensimetrici adottabili (parallelo o T), i collegamenti elettrici adottabili (4 fili o 6 fili) e mostrando una tipica configurazione della rete dei sistemi di acquisizione DAQ. A seguire, viene mostrato un confronto tra le diverse possibili procedure di calibrazione: analitica, carichi esterni e squilibri propri. La procedura che sfrutta gli squilibri propri è la soluzione spesso consigliata. Il lavoro presenta modelli statici-dinamici, che consentono di calibrare i ponti estensimetrici usando gli squilibri di massa propri, e commenta gli intervalli di calibrazione raggiungibili per una tipica turbina, che sono piuttosto limitati rispetto ai carichi massimi attesi in esercizio. Per ciascun modello sarà poi presentata una analisi di incertezza del processo di calibrazione, in accordo con la ISO/IEC Guide 98-3:2008 "Guide to the Expression of Uncertainty in Measurement".

Anche se la calibrazione dovrebbe avvenire in condizione isotermiche, questa condizione nella pratica non può essere sempre verificata. Pertanto, vengono discussi gli effetti termici sui ponti estensimetrici, mettendo in evidenza lo loro influenza sull'incertezza di calibrazione e sull'incertezza del segnale sia per ponti in configurazione T che in configurazione parallela.

Tra le misure estensimetriche eseguite su turbine eoliche quella della misura della coppia sull'albero è spesso la più incerta, poiché affetta da forti fenomeni di crosstalk. Tuttavia, un segnale di coppia accurato può fornire molte informazioni sul stato di salute della turbina eolica, studi hanno infatti dimostrato che una analisi dei segnali di coppia permettono di rilevare guasti nei componenti principali del sistema di trasmissione. Nonostante ciò, la misura della coppia sugli alberi di turbine eoliche è ad oggi complessa; le soluzioni di misura adottabili sono incerte (come gli estensimetri) o invasive (come i torsiometri in linea).

Questa tesi nella seconda parte analizza una tecnica di misura della coppia innovativa e senza contatto costituita da due nastri zebrati montati sull'albero e due sonde ottiche su un supporto rigido non rotante. A differenza dei metodi convenzionali di misura della coppia, il sistema, inizialmente proposta dall'Università di Durham, non richiede sensori costosi o il montaggio di elettroniche sull'albero. Le prestazioni del sistema proposto sono state analizzate in un piccolo banco prova da laboratorio durante condizioni statiche e dinamiche; la tecnica è stata implementata usando due metodi di elaborazione del segnale, approccio rising edge e approccio cross-correlation. I risultati mostrano una buona corrispondenza con le misure di riferimento eseguite attraverso un torsiometro in linea. L'incertezza calcolata in accordo con la ISO GUM (Guide to the Expression of Uncertainty in Measurement) è dello ± 0,3% e ± 0,8% della coppia massima misurabile, rispettivamente per gli approcci del rising edge e cross-correlation. Infine, è presentata una analisi di fattibilità e un disegno di scala del sistema per due turbine eoliche con una diversa configurazione dell'albero, turbina eolica da 60kW con sistema di trasmissione con ingranaggio e turbina eolica da 3 MW con sistema di trasmissione ad azionamento diretto. L'incertezza attesa sulla misura della coppia per le due soluzioni è rispettivamente del 2.0 % e 0.5%.

Acknowledgements

Over the three years from November 2014, many people have assisted me in completing the work described in this thesis and I am grateful to them all.

In particular:

- My PhD supervisor, Prof. Nicola Paone, whose academic guidance and encouragement has been a constant source of motivation. I appreciate all the fruitful discussions and feedback received to make my PhD experience productive and stimulating. His constant support and enlightening guidance in the development and completion of this thesis.
- The technicians at Università Politecnica delle Marche. Particularly, Luca Violini, Engr. Claudio Santolini and Piersavio Evangelisti for their patience, motivation, enthusiasm, and immense knowledge. Their guidance helped me in all the time of research and writing of this thesis.
- Prof. Chris Crabtree and Dr. Donatella Zappalà that gave me the opportunity to work with them and to share the project that has been presented in Chapter 6.
- All those, past and present, from within the Mechanical and Thermal Measurement Group at DIISM who have provided an excellent working atmosphere. In particular, Prof. Enrico Primo Tomasini, Prof. Paolo Castellini, Prof. Gianmarco Revel, Prof. Milena Martarelli, Prof. Lorenzo Scalise and all researchers and PhD students.
- Prof. Renato Ricci for his support in dealing with aerodynamic issues.
- Prof. Lucio Demeio and Prof. Ferrante for their assistance in dealing uncertainty analysis.
- Dr. Matteo Claudio Palpacelli for his assistance in developing calibration models.

Publications

<u>Peer reviewed publications</u>

Journal papers

1. Bezziccheri M., Castellini P., Evangelisti P., Santolini C. and Paone N. (2017). Measurement of mechanical loads in large wind turbines: problems on calibration of strain gage bridges and analysis of uncertainty. *Wind Energy,* pp. 1–14, doi: https://doi.org/10.1002/we.2136.
2. Zappalà D., Bezziccheri M., Crabtree C.J. and Paone N. (2017). Non-intrusive torque measurement for rotating shafts using optical sensing of zebra-tapes. *Measurement Science and Technology*, under review.

Conference proceedings

1. Bezziccheri M., Castellini P., Evangelisti P., Santolini C., Paone N. (2015). Uncertainty associated with strain gauge measurements on wind turbines. *EWEA Annual Event, European Wind Energy Association*, (Paris from 17 to 20 November 2015) abstract available at https://www.ewea.org/annual2015/conference/submit-an-abstract/pdf/2911067515994.pdf.

Posters

1. Zappalà D., Bezziccheri M., Crabtree C.J., Paone N., Rendell S. (2016). Wind turbine non-intrusive torque monitoring. *SUPERGEN Wind General Assembly* (Glasgow 26 Maggio 2016).

Table of Contents

VIII

List of Figures

XII

List of Tables

List of Abbreviations

ABB   Asea Brown Boveri
ANN   Artificial Neural Networks
APC   Active Power Control
ASC   Active Stall Control
CM   Condition Monitoring
CMS   Condition Monitoring System
DAQ   Data AcQuisition
DFIG   Double Fed Induction Generator
DLCs   Design Load Cases
EEA   Europian Enviroment Agency
EESG   Electrically Excited Synchronous Generator
EN   European Standard
EU   European Union
FEM   Finite Element Method
GL   Guideline
GPIB   General Purpose Interface Bus
GUM   Guide to the Expression of Uncertainty in Measurement
GWEC   Global Wind Energy Council
HAWT   Horizontal Axis Wind Turbine
IEC   International Electrotechnical Commission
IEEE   Institute of Electrical and Electronic Engineers
IPC   Individual Pitch Control
IRENA   International Renewable Energy Agency
ISO   International Organization for Standardization
JRC   Joint Research Centre
LWK   Landwirtschaftskammer Schleswig-Holstein
MCM   Monte Carlo Method
MCSA   Motor Current Signature Analysis
MLCs   Measurement Load Cases
NI   National Instruments
NREAPs   National Renewable Energy Action Plans
OP_k' Initialized signal of the k-th optical probe
OP_k Signal of the k-th optical probe
O&M   Operations & Maintenance
PDF   Probability Density Function
PMSG   Permanent Magnet Synchronous Generators
PSC   Passive Stall Control
SAW   Surface Acoustic Wave
SCADA   Supervisory Control And Data Acquisition

SCIG	Squirrel Cage Induction Generators
SHM	Structural Health Monitoring
UNI	Italian Organization for Standardization
VAWT	Vertical Axis Wind Turbine
VIs	Virtual Instruments
WECSs	Wind Energy Conversion Systems
WEI	Wind Energy Index
WMEP	Wissenschaftlichen Mess und Evaluierungsprogramm
WRIG	Wound-Rotor Induction Generator
WT	Wind Turbine

Nomenclature

A	Swept area of the rotor	[m²]
AB	Distance between the application section of the strain gages on the blade and the rotation axis of the shaft	[m]
AE	Annual Energy production	[kWh]
AG$_b$	Distance between the application section of the strain gages and the center of gravity of the part of the blade to the right of the strain gages	[m]
aj	Half-width tolerance of xj	
Av	Availability	
bi	Ordinate at the origin of the calibration line of the i-th bridge	$\left[\dfrac{mV}{V}\right]$
C	Shaft damping coefficient	$\left[\dfrac{\text{kg m}^2}{\text{s rad}}\right]$
Ca	Moment of the Aerodynamic Load on the blade	[Nm]
CoE	Cost of Energy	$\left[\dfrac{€}{\text{kWh}}\right]$
Cp	Wind turbine power coefficient	
D_e	Outer diameters in the section of application of the strain gauges	[m]
$Desired\_U_{CMi}$	Desired combined standard uncertainty	[Nm]
D_i	Inner diameters in the section of application of the strain gauges	[m]
E	Young modulus of the measurement object	[Pa]
e	Excitation voltage of the strain gage bridge	[V]
e$_0$	Electric output voltage of the strain gage bridge	[mV]
$\dfrac{e_{oMi}}{e}$	Ratio between electric output and excitation voltage of the i-th strain gage bridge	$\left[\dfrac{mV}{V}\right]$
$\dfrac{e_{0thermal}}{e}$	Apparent electric voltage due to thermal effects	$\left[\dfrac{mV}{V}\right]$
E	Young's modulus in the section of application of the strain gages	[Pa]
EGc	Distance between the strain gages position and center of gravity of the part of shaft to the right of the strain gages	[m]
EGr	Distance between the strain gages section and center of gravity of the system; rotor+hub	[m]
f_c	Sample frequency of the shaft torque signal	[Hz]
f_f	Frequency of failure	$\left[\dfrac{1}{h}\right]$

f_{OP}	Sampling frequency of the optical probe signal	[Hz]
FRC	Fixed Charge Rate	[€]
g	Acceleration of gravity	$\left[\dfrac{m}{s^2}\right]$
$g_i(\eta)$	Probability Density Function of the i-th quantities	
G	Shear modulus of the measurement object	[Pa]
G_b	Center of gravity of the blade	
h	Number of sample for covariance analysis	
I_b	Inertia matrix of the blade	[kg m²]
I_c	Inertia matrix of the part of shaft to the right of the strain gages	[kg m²]
ICC	Initial Capital investment Cost	[€]
I_r	Inertia matrix of the system; rotor+hub	[kg m²]
I_s	Inertia of the shaft	[kg m²]
J_s	Shaft polar moment of inertia of the shaft	[m⁴]
K	Shaft torsional stiffness	$\left[\dfrac{Nm}{rad}\right]$
k	Gauge factor	
k_p	Covarage factor in uncertainty analysis	
L	Distance between the two optical probes	[m]
LRC	Levelized Replacement Cost	[€]
m_i	Slope of the calibration line of the i-th bridge	$\left[\dfrac{mV}{V\,Nm}\right]$
mb	Mass of the part of the blade to the right of the strain gages	[kg]
mc	Mass of the part of shaft to the right of the strain gages	[kg]
Mbe	Blade root edgewise bending moment	[Nm]
Mbf	Blade root flatwise bending moment	[Nm]
Mi_{max}	Expected design loads of the i-th moment	[Nm]
Mi	Mi-th moment	[Nm]
mn	Massa of the system nacelle, hub and rotor	[kg]
mr	Mass of the system rotor and hub	[kg]
MTBF	Mean Time Between Failures	[h]
Mtl	Tower base lateral bending moment	[Nm]
Mtml	Tower mid lateral bending moment	[Nm]
Mtmn	Tower mid normal bending moment	[Nm]
Mtn	Tower base normal bending moment	[Nm]
MTTF	Mean Time To Failure	[h]
Mttl	Tower top lateral bending moment	[Nm]
Mttn	Tower top normal bending moment	[Nm]
MTTR	Mean Time To Recovery	[h]

Symbol	Description	Units
n	Shaft rotational speed	[rpm]
OGn	Distance between tower axis and the center of gravity of the system nacelle, hub and rotor	[h]
OM	Annual Operation and Maintenance cost	$\left[\dfrac{€}{kWh}\right]$
P	Zebra tape period	[m]
P_a	Available power in the wind	[W]
P_{El_a}	Electric active power output from the wind turbine	[W]
P_{min}	Minimum zebra tape period	[m]
ppr	Number of pulses per shaft revolution	
ppr_{max}	Maximum allowable number of pulses per revolution	
P_t	Energy extract from the wind turbines	[W]
R	Strain gage's resistance	[Ω]
r	Shaft radius	[m]
Re	Outer radius in the section of application of the strain gauges	[m]
Ri	Inner radius in the section of application of the strain gauges	[m]
Rm	Mean radius in the section of application of the strain gauges	[m]
$R^2_{\_p}$	Coefficient of determination	
Ru	Ratio between desired combined uncertainty and uncertainty of the reference moment	
r_{12}	Cross-correlation	
$s_{\left(\frac{e_{oMi}}{e}\right)}$	Standard deviation of $\frac{e_{oMi}}{e}$	$\left[\dfrac{mV}{V}\right]$
s_{b_i}	Standard deviations of b_i	$\left[\dfrac{mV}{V}\right]$
s_{m_i}	Standard deviations of m_i	$\left[\dfrac{mV}{V\,Nm}\right]$
s_n	Standard deviations of shaft rotational speed	[rpm]
s_K	Standard deviations of shaft torsional stiffness, K	$\left[\dfrac{Nm}{rad}\right]$
s_{M_i}	Standard deviation of Mi	[Nm]
S_L	Pre-set threshold level of the trigger	[V]
s_j	Standard deviation of xj	
$s_{T_{rotor}}$	Standard deviation of T_{rotor}	[Nm]
s_{θ_r}	Standard deviation of θ_r	[rad]
T_a	Force of the Aerodynamic Load on the blade	[Nm]
$t_{iOP'_k}$	Rising edge time instants	[s]

XX

T$_{mean}$	Mean temperature of the bridge	[°C]
t$_p$	Start time of the initialize signals	[s]
T$_{rotor}$	Shaft torque	[Nm]
T$_{rotor-max}$	Maximum shat torque expected during operation	[Nm]
T$_{rotor\_RANGE}$	Measuring shaft torque range	[Nm]
T$_s$	Stran gage operating temperature minus strain gage calibration temperature (typically 20 °C)	[°C]
u_{α_b}	Uncertainty of α_b	$\left[\frac{1}{°C}\right]$
u_{α_m}	Uncertainty of α_m	$\left[\frac{1}{°C}\right]$
u_{α_r}	Uncertainty of α_r	$\left[\frac{1}{°C}\right]$
U_{CMi}	Combined standard uncertainty of each Mi moment	[Nm]
u_E	Uncertainty of E	[Pa]
u_k	Uncertainty of k	
$u_{M\,calibration-i}$	Uncertainty of the reference moment $M_{calibration-i}$	[Nm]
u$_{MCM}$	Uncertainty obtained by applying the MCM	[Nm]
u_{R_m}	Uncertainty of R$_m$ measurement	[m]
$u(T_{13}, T_{24})$	Covariance of T13 and T24 measurements	[°C]
$u_{T_{13}}$ and $u_{T_{24}}$	Uncertainty of T13 and T24 measurements	[°C]
u_{x_j}	Uncertainty of xj	
$u_{\varepsilon_{sR}}$	Uncertainty of ε_{sR}	
$U_{cal\_M_i}$	Calibration uncertainty of Mi	[Nm]
$U_{sig\_M_i}$	Signal uncertainty of Mi	[Nm]
$U_{t\_M_i}$	Total standard uncertainty of Mi	[Nm]
x$_j$	j-th parameter used in calibration model	
X$_T$	Switching distance of the optical probe	[m]
α	Tilt angle of the nacelle	[°]
α_b	Thermal expansion coefficient of the measurement object	$\left[\frac{1}{°C}\right]$
α_m	Thermal expansion coefficient of the strain gage grid material	$\left[\frac{1}{°C}\right]$
α_r	Temperature coefficient of the electrical resistance of the strain gage grid foil	$\left[\frac{1}{°C}\right]$
β	Blade pitch	[°]
ΔR	Variation of the strain gage's resistance	[Ω]
ΔT	Temperature difference between adjacent strain gages of the bridge	[°C]
Δt	Time shift between pulse trains	[s]

Δt_r	Time shift between rising edge of pulse trains evaluated using the rising edge method	[s]
$\overline{\Delta t_r}(t_j)$	Eight-point averaged time shift evaluated using the rising edge method	[s]
$\Delta t_c(t_j)$	Time shift per zebra tape pulse evaluated using the cross correlation method	[s]
δ_d	Displacement between pulse centre of two optical probes signal	[s]
δt_f	Displacement between falling edge of two optical probes signal	[s]
δt_r	Displacement between rising edge of two optical probes signal	[s]
$\delta\theta_r$	Resolution on θ_r estimation	[rad]
ε_i	Strain measured by i-th strain gage	
ε_{sL}	Apparent strain due to thermal effects: linear error	
ε_{sR}	Apparent strain due to thermal effects: residual error	
ε_{sTOT}	Apparent strain due to thermal effects: overall error	
η	Drive train and generator efficiency	
θ	Rotor azimuth	[°]
θ_a	Absolute angular shift between two optical probes signal	[rad]
$\theta_{a\_c}(t_j)$	Shaft absolute angular shifts evaluated using the cross correlation method	[rad]
$\theta_{a,0}$	Apparent angular shift between two optical probes signal	[rad]
$\theta_{a\_r}(t_j)$	Shaft absolute angular shifts evaluated using the rising edge method	[rad]
$\theta_{full_{scale}}$	Maximum measurable shaft torsion angle	[rad]
θ_{max}	Maximum torsion angle of the shaft expected during operation	[rad]
θ_r	Relative angular shift between two optical probes signal	[rad]
θ_{RANGE}	Measuring range of the shaft torsion angle	[rad]
λ	Tip speed ratio	
ν	Poisson's ratio of the measurement object	
ρ	Air density	$\left[\dfrac{kg}{m^3}\right]$
τ	Pulse trains period	[s]
ϕ	Yaw angle of the nacelle	[°]

$\dot{\omega}$	Angular acceleration of the rotor	$\left[\dfrac{rad}{s^2}\right]$
ω	Angular speed of the rotor	$\left[\dfrac{rad}{s}\right]$
γ	Cone angle of the rotor	$[°]$

INTRUDUCTION

Devastating floods, extreme droughts, thermal expansion of the oceans, glacial erosion, abnormal acidification and abundant elevation of the seas: these are some of the natural disasters, indisputable witnesses of a massive climate change that affects all over the world. The weather records that have been collected, weather balloon and satellite data and other data provides us with overwhelming evidence that global warming is happening and that man's action is definitely the cause. We can do nothing about the sun, nor the water vapour in clouds, so the only thing we can do is to reduce our CO_2 production and stop deforestation. Man exerts a growing influence on climate and on earth's temperatures with activities such as combustion of fossil fuels, deforestation and livestock breeding.

The collected data also give us some idea of where we are heading. Our planetary policies seem to accept the inevitable 2 $\mathcal{C}$ rise by 2050 due to of the environmental damage that we have already caused. However, to aim to limit the increase of 2 °C, renewable energy sources have to be developed. These should allow an economic growth and industrialization without this being at the expense of the well-being of the Planet and of those who live there.

This chapter begins by describing the dependence between climate change and the use of fossil fuel; this is followed by a short discussion of the importance of using renewable energy sources to limit the climate change, where wind energy plays a central role. Therefore, paragraphs 1.3 and 1.4 provide a general overview of the different wind turbine solutions and installed wind power.

1.1 Energy overview

Energy is a foundation stone of the modern economy and it provides an essential ingredient for all human activities. Energy production is a powerful engine of economic and social development, especially in a globalized world. The global energy scene is in a state of continuous change and the forecasting trend for the energy development remains critical because it is strictly dependent by national policy decisions about energy investments. The U.S. Energy Information Administration provides a periodic analysis about the world energy consumption and forecasting trend for years to come. In particular, the International Energy Outlook 2016 (IEO2016) [1] continues to show rising levels of energy demand over the next three decades, with an expected increase in total world energy consumption of 266 quadrillion Btu, rises from 549 quadrillion Btu in 2012 to 629 quadrillion Btu in 2020 and 815 quadrillion Btu in 2040 - 48% increase from 2012 to 2040. As shown in Figure 1, most of the world's energy growth will occur in the countries outside the Organization for Economic Cooperation and Development (OECD); countries for which a long and strong economic growth is expected, which

will lead to an inevitable increase in the energy consumption. Non-OECD energy consumption will increase by 71% between 2012 and 2040 compared to a 18% in OECD countries; where the two main non-OECD countries that will record the largest energy growth are India and China. This forecast will lead by 2040 that almost two-thirds of the world's primary energy will be consumed in non-OECD economies.
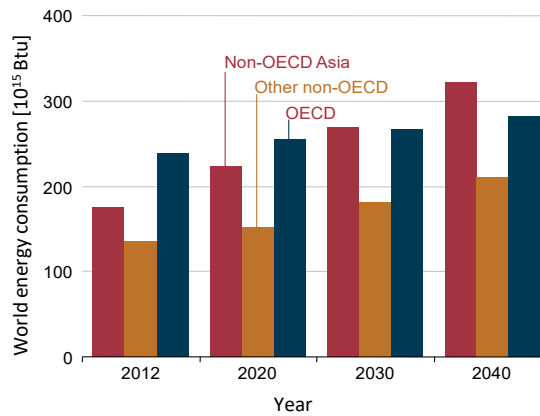
Figure 1 World energy consumption by country grouping, 2012–40 (quadrillion Btu) [1]

For consistency, OECD includes all members of the organization as of January 1, 2016, throughout all the time series included in this report. OECD member countries as of January 1, 2016, were Austria, Australia, Belgium, Canada, Chile, Czech Republic, Denmark, Estonia, Finland, France, Germany, Greece, Hungary, Iceland, Ireland, Israel, Italy, Japan, Luxembourg, Mexico, the Netherlands, New Zealand, Norway, Poland, Portugal, Slovakia, Slovenia, South Korea, Spain, Sweden, Switzerland, Turkey, the United Kingdom, and the United States. For statistical reporting purposes, Israel is included in OECD Europe.

1.1.1   Outlook for world energy markets by source

World energy consumption and forecasting trend for years to come, provides by US Energy Information Administration and reported in IEO2016 [1], predict that the world energy consumption will increase, as shown in Figure 1, through the growth of all energy sources until 2040, as shown in Figure 2.

Renewable sources will be the source of energy that will record the fastest growth in the world during the projection period, with an average annual growth of 2.6%. Nuclear power will be the second fastest growing source of energy, with an expected average annual growth of 2.3%. Finally, for natural gas and coal will be expected an average annual growth of 1.9% and 0.6% per year. Fossil fuels will be the only energy source, of world marketed energy consumption, that will record a fall in average annual growth from 33% in 2012 to 30% in 2040. However, fossil fuels will still account for 78% of energy use in 2040, thus remaining the most used energy source.

Note: Dotted lines for coal and renewables show projected effects of the U.S. Clean Power Plan.

Year
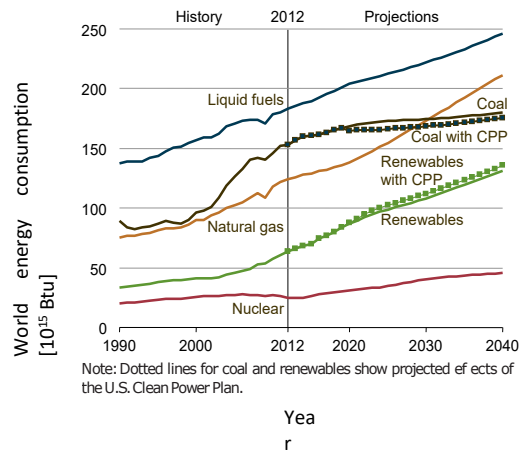
Figure 2 Total world energy consumption by energy source, 1990–2040 (quadrillion Btu) [1]

1.1.2 Energy security and climate change

The climatic change, caused by rising global temperature, is one of the most import problems of the 21st century. It has major implications for the world's social and economic stability as described during the last Climate Conference in Paris in December 2015. The Paris Agreement [2] starts from a fundamental premise: "Recognizing that climate change represents an urgent and potentially irreversible threat to human societies and the planet and thus requires the widest possible cooperation by all countries, and their participation in an effective and appropriate international response, with a view to accelerating the reduction of global greenhouse gas emissions."

The Earth's climate has changed throughout history, as shows in Figure 3. Most of these climate changes are attributed to very small variations in Earth's orbit that change the amount of solar energy our planet receives.
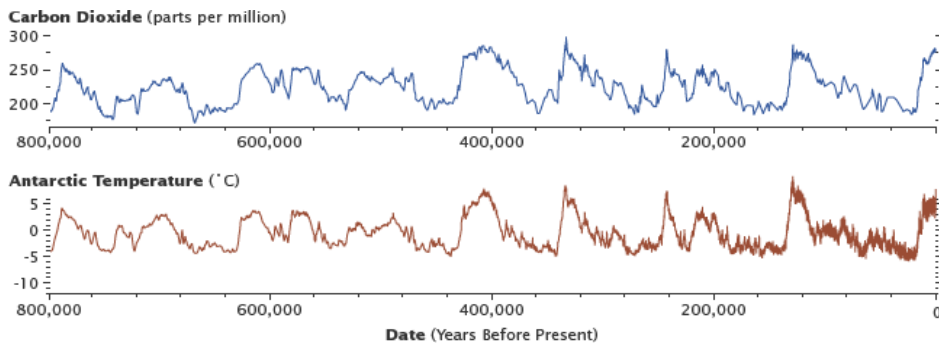
Figure 3 Levels of carbon dioxide in the atmosphere and the Antarctic temperature over the past 800,000 years (Graphs by Robert Simmon, using data from Lüthi et al., 2008, and Jouzel et al., 2007.)

However, the current warming trend is of particular significance because most of it is extremely likely human-induced and proceeding at a rate that is unprecedented in the past 1,300 years [3][4][5][6][7]. In 1824 Joseph Fourier was the first person to discovered that the earth was heating up [8], but Svante Arrhenius, a Swedish scientist, was the first to claim fossil fuel combustion may eventually result in enhanced global warming. Earth receives energy from the sun and some of that is emitted back into the space, a part of this emitted back energy is absorbed by carbon dioxide in the atmosphere and reemitted back towards the ground [8]. Figure 4 shows a comparison between levels of CO_2 in atmosphere and world coal giga-tons of CO_2, the two trends are strongly connected and this allows to affirm that the industrialization has most likely had an effect on CO2 levels and so on the global temperature.
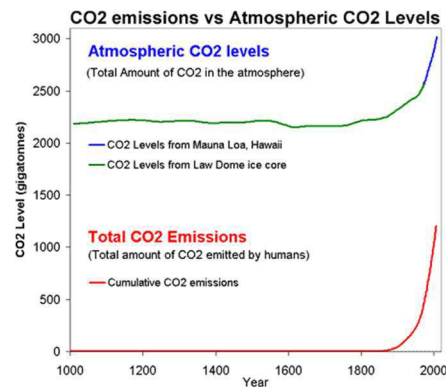
Figure 4 Atmospheric CO2 levels (Green is Law Dome ice core, Blue is Mauna Loa, Hawaii) and Cumulative CO2 emissions (CDIAC)

Earth-orbiting satellites and other technological advancements, collected over many years, have revealed a changing climate. This effect has been expressed in several forms:

- global sea level rose about 17 cm in the last century [9];
- the global average temperature are 1.7 °F or more above the 1880 [10];
- the oceans have absorbed much of this increased heat, with the top 700 meters of ocean showing warming of 0.302 °F since 1969 [11];
- the Greenland and Antarctic ice sheets have decreased in mass. Data from NASA's Gravity Recovery and Climate Experiment show Greenland lost 150 to 250 cubic kilometers of ice per year between 2002 and 2006, while Antarctica lost about 152 cubic kilometers of ice between 2002 and 2005;
- Declining Arctic sea ice [12][13];
- Glacial retreat [14];
- Ocean acidification is increasing by about 2 billion tons per year [15][16];
- Decreased snow cover [17];

The way we produce our energy has major implication for the world's health and economic stability. The awareness of the state leaders can push the adaptation of national energy action plans to reduce energy consumption and to develop solutions to decarbonize the energy system in a sustainable way.

1.1.3 Renewable energy in Europe and role of wind energy

In Europe, the EU's Renewable energy directive sets a binding target of 20% final energy consumption from renewable sources by 2020. To achieve this, EU countries have committed to reaching their own national renewables targets ranging from 10% in Malta to 49% in Sweden. They are also each required to have at least 10% of their transport fuels come from renewable sources by 2020 [18].

Every two years, EU countries report on their progress towards the EU's 2020 renewable energy goals. Findings from the latest EU-wide report in 2015 showing that the majority of Member States are nevertheless expected to meet or exceed their 2020 renewable energy targets based on an assessment of current and planned policies (Figure 5) [19].
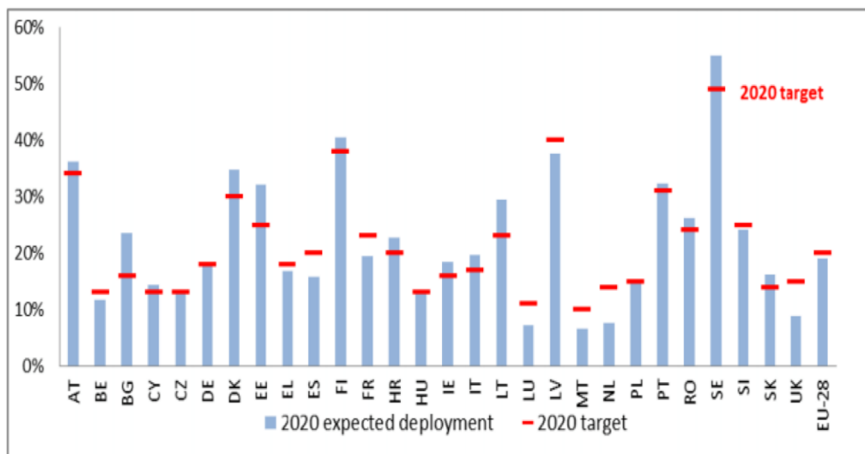
Figure 5 Expected Renewable Energy Standard deployments in Member States and 2020 Renewable Energy Standard targets

Where, the figure projects 2020 with current and planned policies in place, and it does not take into account the policies implemented after 2013 or the necessary additional efforts by Member States in order for them to comply with the legally binding targets.

Table 1 gives a more detailed comparison of the estimated and planned, based on National Renewable Energy Action Plans (NREAPs), deployment levels for each renewable energy technology at EU level in 2014 and by 2020. It also aggregates

(by sector and for renewable energy in total) model projected deviations from the NREAP target levels - comparing expected and planned deployment [19].

	Projected deployment 2014	NREAP target 2014	Projected 2020 deployment		2020 target	Deviations			
			Min.	Max.		2012	2014	2020 Min.	2020 Max.
Technology category	Mtoe	Mtoe	Mtoe	Mtoe	Mtoe	%	%	%	%
RES electricity	**72.5**	**73.3**	**91.9**	**94.9**	**103.7**	**2.1**	**-1.1**	**-13.0**	**-8.5**
Biomass (solid and liquid)	9.1	10.3	12.2	12.6	14.7	-8.2	-11.2	-19.3	-14.3
Biogas	4.3	3.5	5.1	5.1	5.4	35.2	22.1	-7.9	-6.2
Geothermal	0.5	0.6	0.9	0.9	0.9	-9.5	-13.0	-21.8	-0.9
Hydro large-scale	26.1	26.5	27.7	27.8	27.4	-1.0	-1.4	0.9	1.5
Hydro small-scale	4.2	4.0	4.8	4.9	4.5	-1.0	4.0	6.9	9.6
Photovoltaics	7.7	3.9	10.1	10.4	7	94.2	96.8	38.8	47.6
Concentrated solar power	0.3	0.7	0.3	0.4	1.6	-21.2	-52.6	-78.3	-76.5
Wind onshore	18.9	20.3	28.2	30.1	30.3	-4.4	-7.0	-8.7	-0.7
Wind offshore	1.3	3.4	2.4	2.6	11.5	-38.1	-62.7	-80.3	-77.0
Marine/Ocean	0.1	0.1	0.2	0.2	0.5	-19.2	-38.9	-56.2	-54.3
RES heating & cooling	**87.6**	**80.5**	**105.6**	**107.5**	**108.9**	**10.6**	**8.8**	**-4.2**	**-1.3**
Biomass (solid and liquid)	73.7	68.1	84.9	86.5	85.3	9.6	8.3	-1.6	1.4
Biogas	2.5	2.5	3	3	4.5	16.5	0.4	-33.7	-32.5
Geothermal	0.7	1.2	1.3	1.3	2.6	-34.4	-41.6	-50.9	-50.4
Heat pumps	8.5	6.2	12.8	12.9	10	33.4	37.7	25.5	29.3
Solar Thermal	2.2	2.6	3.7	3.7	6.4	-1.7	-15.3	-45.6	-41.8
RES transport (biofuels only)	**16.6**	**18.4**	**18.5**	**19.1**	**29.5**	**-2.5**	**-9.7**	**-37.2**	**-35.0**
1st generation biofuels	14.6	17.6	16.2	16.9	27.1	-11.2	-16.9	-40.0	-37.7
2nd generation biofuels	2.0	0.8	2.3	2.3	2.4	211.0	143.7	-5.5	-4.9
RES total	**176.7**	**172.3**	**216.0**	**221.5**	**242.1**	**5.7**	**2.6**	**-12.0**	**-8.5**

Table 1 Projected deployment and deviation from planned EU technology deployment 2014 and 2020

Given that, the majority of Member States are nevertheless expected to meet or exceed their 2020 target, the EU Commission has already published a proposal of new renewable energy target (at least 27%) by 2030. Furthermore, even if wind energy will not reach the goals 2020 (with predictable deviation less than 8.7% for the onshore and less than 80.3% for the offshore), the Commission has identified wind energy as one of the key strategic energy technologies. Indeed, the Commission expects that wind energy will be one of the main electricity generating technologies of the 2050 Energy Roadmap and they will provide between 31% and 48% of electricity production in Europe.

1.2   Wind turbine Background

In the 1st century AD a Greek engineer, Heron of Alexandria, creates for the first time, in known history, a wind-driven wheel used to power a machine. However,

INTRODUCTION

the first known wind turbine used to produce electricity has been built in Scotland only in 1887; it has been created by Prof James Blyth of Anderson's College.

Since 1887, the wind energy technology, thanks to years of innovation and scientific research based on aerodynamic, mechanic, electric and acoustic aspects, has evolved up to the modern wind turbines and the global cumulative installed capacity has increased. Focusing in the last 15 years, the global cumulative installed wind capacity at the end of 2016 is 20 times greater than the installed wind capacity at the end of 2001, as shown in Figure 6 [49].
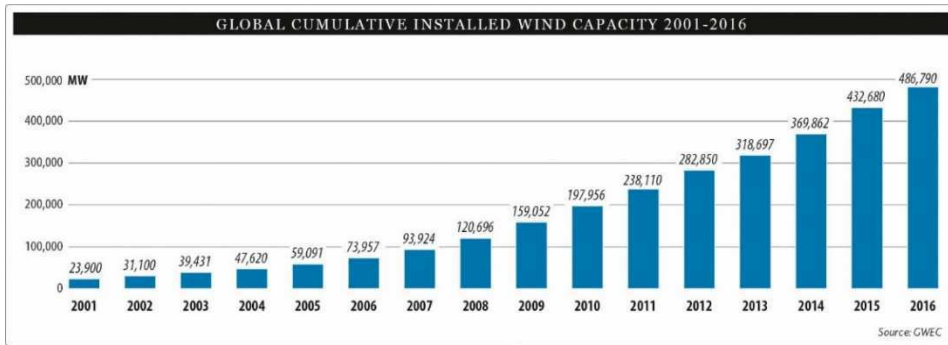
Figure 6 Global cumulative installed wind capacity 2001-2016. Source GWEC [49]

According to Figure 7 [41], the global wind energy council will expected also an increasing in the next years and a scenario in line with the global wind capacity trend is expected in the EU countries, as shown in Table 2.

GLOBAL CUMULATIVE WIND POWER CAPACITY					
	2013	2015	2020	2030	2040	2050
New Policies scenario					
MW	318,128	396,311	610,979	964,465	1,324,814	1,684,074
TWh/a	620	972	1,499	2,535	3,482	4,426
Moderate scenario					
MW	318,128	413,039	712,081	1,479,767	2,089,261	2,672,231
TWh/a	620	1,013	1,747	3,889	5,491	7,023
Advanced scenario					
MW	318,128	420,363	800,615	1,933,989	3,024,473	4,042,475
TWh/a	620	1,031	1,964	5,083	7,948	10,624

Figure 7 Global cumulative wind power capacity. Source GWEC [41].

	2014			2020 Target (Central scenario)			Low 2030 scenario			Central 2030 scenario			High 2030 scenario		
	Onshore	Offshore	Total	Onshore	Offshore	Total	Onshore	Offshore	Total	Onshore	Offshore	Total	Onshore	Offshore	Total
Austria	2,095	-	2,095	3,400	-	3,400	5,000	-	5,000	5,800	-	5,800	6,650	-	6,650
Belgium	1,247	713	1,959	3,000	1,500	4,500	2,650	2,200	4,850	3,300	3,000	6,300	4,000	3,800	7,800
Bulgaria	690	-	690	1,500	-	1,500	1,000	-	1,000	1,220	-	1,220	1,440	-	1,440
Croatia	347	-	347	600	-	600	1,600	-	1,600	1,800	-	1,800	2,000	-	2,000
Cyprus	147	-	147	300	-	300	447	-	447	483	-	483	581	-	581
Czech Republic	282	-	281	1,000	-	1,000	1,040	-	1,040	2,200	-	2,200	4,320	-	4,320
Denmark	3,603	1,271	4,845	3,700	2,800	6,500	3,300	2,650	5,950	4,600	3,530	8,130	6,000	5,320	11,320
Estonia	303	-	303	700	-	700	365	-	365	433	750	1,183	500	1,500	2,000
Finland	607	26	627	2,500	26	2,526	5,000	26	5,026	8,500	26	8,526	12,000	26	12,026
France	9,285	-	9,285	18,500	1,500	20,000	19,000	6,000	25,000	26,250	9,000	35,250	28,000	15,000	43,000
Germany	38,369	1,049	39,165	45,000	6,500	51,500	60,000	15,000	75,000	62,500	17,500	80,000	65,000	22,500	87,500
Greece	1,980	-	1,980	4,500	-	4,500	8,000	-	8,000	9,000	-	9,000	12,000	500	12,500
Hungary	329	-	329	600	-	600	925	-	925	973	-	973	1,051	-	1,051
Ireland	2,246	25	2,272	4,000	25	4,025	5,500	25	5,525	6,892	800	7,692	8,390	1,200	9,590
Italy	8,665	-	8,663	12,000	-	12,000	10,768	-	10,768	13,600	-	13,600	16,768	500	17,268
Latvia	62	-	62	200	-	200	234	-	234	308	-	308	430	-	430
Lithuania	279	-	279	600	-	600	878	-	878	1,110	-	1,110	1,200	1,000	2,200
Luxembourg	58	-	58	100	-	100	123	-	123	141	-	141	169	-	169
Malta	-	-	-	30	-	30	30	-	30	49	-	49	80	-	80
Netherlands	2,565	247	2,805	4,000	1,400	5,400	5,872	6,000	11,872	6,067	6,500	12,567	6,391	7,000	13,391
Poland	3,834	-	3,834	10,000	-	10,000	7,900	500	8,400	11,800	1,350	13,150	13,500	2,200	15,700
Portugal	4,913	2	4,915	5,700	25	5,725	5,924	27	5,951	6,373	27	6,400	7,012	27	7,039
Romania	2,954	-	2,954	3,200	-	3,200	4,500	-	4,500	5,000	-	5,000	6,000	-	6,000
Slovakia	3	-	3	300	-	300	300	-	300	331	-	331	486	-	486
Slovenia	3	-	3	30	-	30	33	-	33	49	-	49	75	-	75
Spain	22,982	5	22,987	26,000	5	26,005	35,000	5	35,005	44,500	5	44,505	52,000	500	52,500
Sweden	5,220	212	5,425	6,000	212	6,212	8,600	202	8,802	13,300	1,000	14,300	18,000	2,000	20,000
UK	7,953	4,494	12,440	11,500	9,500	21,000	12,300	12,000	24,300	17,000	23,000	40,000	20,000	35,000	55,000
Total	121,021	8,044	128,744	168,960	23,493	192,453	206,291	44,635	250,926	253,578	66,488	320,066	294,043	98,073	392,116

Table 2 Capacity scenarios per country (MW)[39]

1.3   Onshore and Offshore Wind Turbines

Depending on the location where the turbine is allocated, it is possible to classify wind turbines as onshore or offshore: onshore refers to turbines located on the ground, while offshore turbines are found in sea or freshwater. Environmental costs, landscape and acoustic constraints, investment costs, maintenance costs, and full load hours are the main factors which affect the installation of a wind turbine and their impact are different in onshore and offshore wind turbines. The following sections will present a brief description of the main differences of the two installation solutions

1.3.1   Onshore Wind Turbines

Onshore wind energy is one of the most mature of all the renewable technologies. Back in the early 2000's, all wind power was generated by wind turbines located on land because it is cheaper. They require less infrastructure and less advanced and specialized technology. Furthermore, the power generation can be located near shorelines, with a reduction for transmission lines costs.

The onshore wind power capacity installed in EU was equal to 121.021 MW at the end of 2014 (Table 2), that correspond to approximately 260 TWh electricity production. However, the generated energy is only a few percent of the available energy from wind on land in EU. In particular, the European Enviroment Agency (EEA) in [38] assumes that the technical potential of onshore wind turbine in Europe is equal to 39000 TWh. Where, the technical potential is the amount of the

electrical energy that can be produced in UE taking into account all limitation, such as biodiversity protection (the deaths of birds and bats that fly into rotor blade), social preference (i.e. noise and visual impact) and regulatory restrictions. Furthermore, the European Environment Agency estimates a technical potentiality of 2500 TWh in all UE mountainous areas [38].

1.3.2 Offshore Wind turbines

In 1991, the first offshore windfarm has been created. A windfarm of 11 450kW turbines has been built in Vindeby, in the southern part of Denmark. However, the offshore wind turbine did not become popular until the 2000, when the UK's Department of Trade and Industry launched the 'Offshore Wind Capital Grants Scheme' to promote the deployment of offshore wind. Currently, offshore wind turbine is become an alternative or supplement to onshore, several advantages have led the growth of offshore application, such as:

1. Offshore wind speeds are typically much more energetic (Figure 8) and much more constant during the year, therefore the offshore wind turbines typically have significant higher load hours (Figure 9). Furthermore, the offshore winds usually increase during the afternoon when the grid needs are the highest [40]. The offshore wind turbines are usually designed to optimize the power output for a reduced wind range, especially for the afternoon wind speeds. This means that, they will have more efficiency in comparison to onshore solutions and provide the maximum power during the network needs, i.e. in the afternoon;
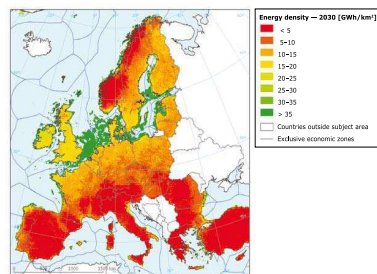
Figure 8 Distribution of wind energy density (GWh/km^2)in europe for 2030 (80 m hub height onshore, 120 m hub height offshore)[38]
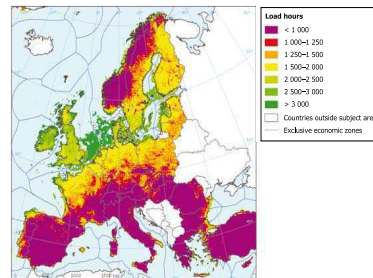
Figure 9 Distribution of full load hours in Europe (80 m hub height on shore, 120 m hub height offshore)[38]

2. No noise pollution, wind turbines have many components that generate noise [44]. Turbine noise is one of the main complaints made by the opponents of onshore wind turbine [45]. As a result, the onshore wind turbine manufactures have to design the wind turbine instead to limit the level noise [61]. Contrary to onshore wind turbine, no noise limitation is

applied on offshore wind turbine. This makes the wind turbine more economically and allows building turbines with downwind rotors[43];

3. Less injuries to Birds, wind turbines cause frequently deaths and injuries of bath and birds. Few studies have shown that birds have been found dead where large turbines are located;

4. Reduce the visual impact, the wind turbines can be seen from the land if they are located up to 10 km from the coast. Therefore, in some countries it is prohibited to build wind farms within a defined distance from the coast (for example, in Netherlands is prohibited to build wind farms within 22 km from the coast) [38]. Furthermore, for the offshore wind turbine could be also used lattice towers [43]. This towers, lighter and cheaper, are rare for aesthetic reasons in onshore installation [46] [47];

The vast majority of offshore wind capacity is installed in United Kingdom [42], thanks to the large number of offshore wind energy projects which were funded in the last five years, as shown in Figure 10. According to Figure 11, at the end of 2013 over 50% of global offshore power production is attributed to the UK.

In Europe, the installed offshore wind capacity is still low, equal to 8.044 MW at the end of 2014 (Table 2), but a rapid increase is expected in the next years. In particular, European Wind Energy Association will expect an increase of 725% at the end of 2030 for a central scenario.

	2000	2001	2002	2003	2004	2005	2006	2007	2008	2009	2010	2011	2012
UK	4	0	0	60	60	90	90	100	187	270	357	184	1271
Denmark	0	40	160	200	0	0	0	0	0	448	0	0	0
Netherlands	0	0	0	0	0	0	108	0	120	0	0	0	0
Sweden	0	11	10	0	0	0	0	110	0	0	30	0	0
Belgium	0	0	0	0	0	0	0	0	30	0	165	0	185
Germany	0	0	0	0	5	0	3	0	5	60	0	48	0
China	0	0	0	0	0	0	0	0	0	0	303	51.5	99.3
Accumulated (MW)	36	87	257	517	607	697	898	1108	1475	2252.8	3109.7	3393.1	4947.7

Installation Year

Figure 10 Worldwide installed offshore wind capacity[42]
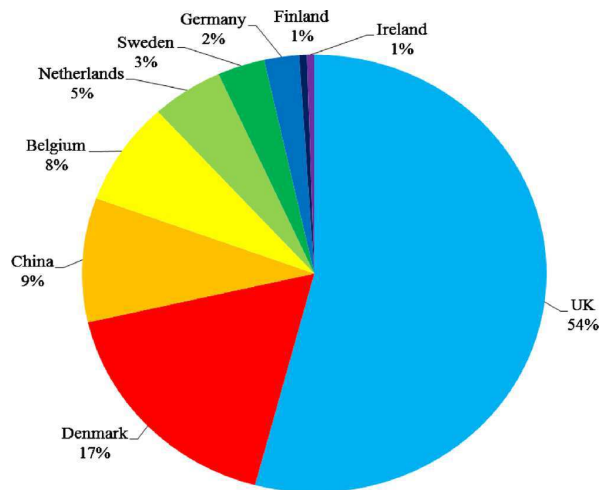
Figure 11 International breakdown of installed offshore wind capacity [42]

Despite the great potential of offshore installation in Europe, the European Environment Agency estimates a technical potential equal to 5100 TWh due to the high price of its installation [38]; it costs between 2.5-3.5 times more the wind turbine built on land. Furthermore, the application in offshore environment bring with them a considerable number of disadvantages, related to the adverse and difficult condition of sea which cause an increase of wind turbine cost. For example:

1. Offshore environments are corrosive for electrical and structural equipment; therefore cathodic and humidity protection are required[43];
2. Storms are much more common than onshore environment, therefore some precautions need to be taken to prevent catastrophic damage during this events [40];
3. Operation and maintenance cost for offshore wind turbine make up a large proportion of the overall cost of energy [48]. A maintenance on offshore wind farm usually involves a helicopter and highly trained technicians; this implies an increase of cost and risk, all while battling the unpredictable weather of the open seas[40];
4. The offshore foundation is more expensive than onshore foundation[43];
5. A transmission lines have to be built to connect offshore farm to the onshore grid. These lines are expensive due to the added costs associated with installing power lines under water [40].

1.4   VAWT and HAWT Wind Turbines

Based on the orientation of the rotating axis of the machine, wind turbines can be classified into two core types, which are the horizontal axis wind turbine (HAWT) and the vertical axis wind turbine (VAWT). The next two paragraphs aim at presenting a comparison of these two different types of wind turbine.

1.4.1 Vertical Axis Wind Turbines (VAWT)

They have axis of rotation perpendicular to the ground and therefore they do not need to be aligned with the wind. Their lower efficiencies make their employ recommended for small wind turbines and in urban areas, where the turbulence is greater and then the alignment becomes difficult. However, the HAWT technology is still dominating this market. In particular, at the end of 2011, 74% of small wind turbine manufacturers developed HAWT, 18% invested in VAWT while only 6% adopted both technologies [36];

1.4.2 Horizontal Axis Wind Turbine (HAWT)

HAWTs have axis of rotation parallel to the ground. In this case, the rotor needs to be aligned with the wind and this is done with tail or with an active yaw on large wind turbine. This configuration is preferred than VAWT for multi megawatt wind turbines thanks to their greater power generation and higher efficiencies.

This thesis discusses the complexity of measuring mechanical load on HAWT; therefore, from this point onwards, this chapter will mainly focus on the state of the art of this configuration.

The basic parts of a horizontal axis wind turbine are:

1. Foundation (Figure 12);
2. Tower (Figure 12);
3. Rotor and rotor blades (Figure 12);
4. Nacelle with drive train (Figure 12);
5. Gearbox;
6. Generator;
7. Coupling and brake;
8. Electronic equipment.
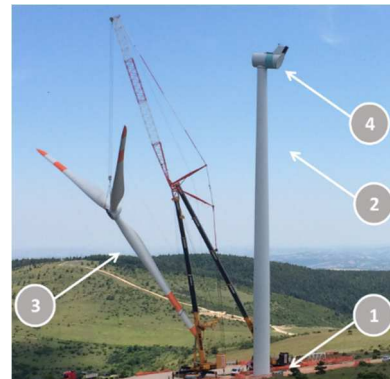
Figure 12 Crucial parts of a HAWT

For more of these parts, following is presented the evolution and market penetration of different technological solutions during 2005–2014, in accordance with [20].

1.4.2.a Evolution of rotor diameter, hub height and rated power

The design and length of the blades are one of the factors that more influence the performance of a wind turbine. Indeed, they have a significant effect on swept area and then on the power extracted by the wind turbine. This has led to an increase in the blade length, from 15 m usual in the late 1980s to 80 m at the beginning of

2017. Figure 13 shows the market trend of rotor diameter during 2005-2014 for onshore wind turbines with horizontal-axis [20]. This improved has also been done considering mechanical and acoustic problems that appeared with the increase in blade length. For example, an increase in the blade length will increase its deflection due to wind force, which may lead to dangerous situation of collision of blade on the tower.

The improvement has been possible by evolving its manufacturing process. Currently, the material of the blade include as well epoxy resins reinforced mainly with glass fibers and seldom with the lighter but more expensive carbon fibers.
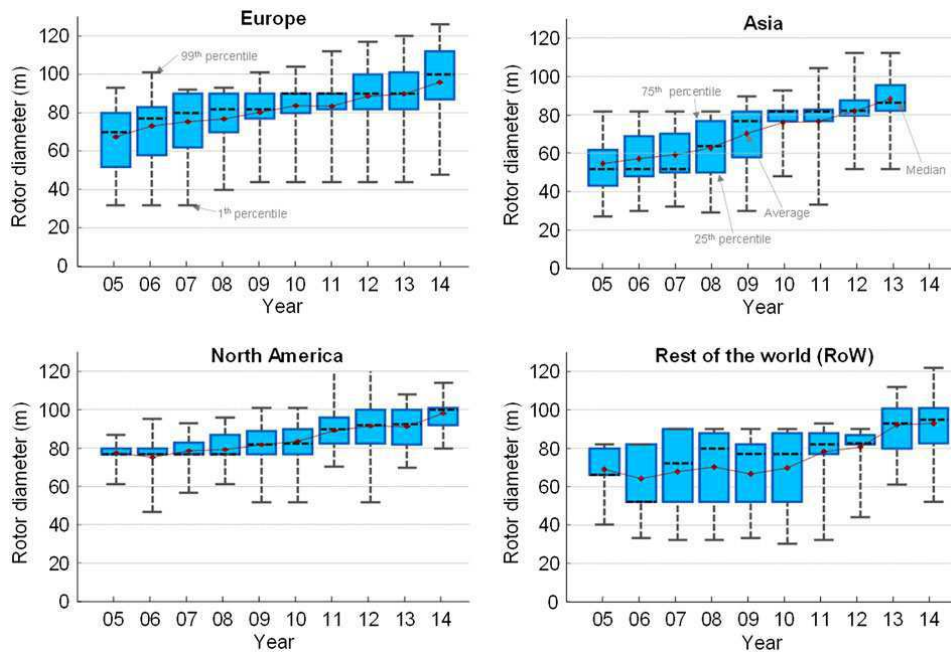
Figure 13 Box plot representation of rotor diameters of onshore wind turbines annually installed [20]. Sorce:JRC data

Concerning the tower, from power extraction point of view, it is better that the tower is as high as possible. Indeed, a high tower will allow to minimize turbulence and maximize the performance of the turbine by exposing the rotor to higher wind speed. However, since that the costs of the tower increase with its height, the design of the tower should be done by taking into account both energetic and economic issue. Figure 14 shows the market trend of hub heights annually installed during 2005-2014 for onshore wind turbine [20].

The most common towers are made in steel; however, some alternative techniques are being born to satisfy the demand of taller tower. For example, hybrid steel–concrete towers, with the tower base made in concrete and the upper part in steel [21].

The rated power of onshore wind turbines is improved as shown in Figure 15, thanks to technological improvements applied on the blades and on the towers in the last years. Where, rated power is defined as the maximum electrical power that the generator can provide.
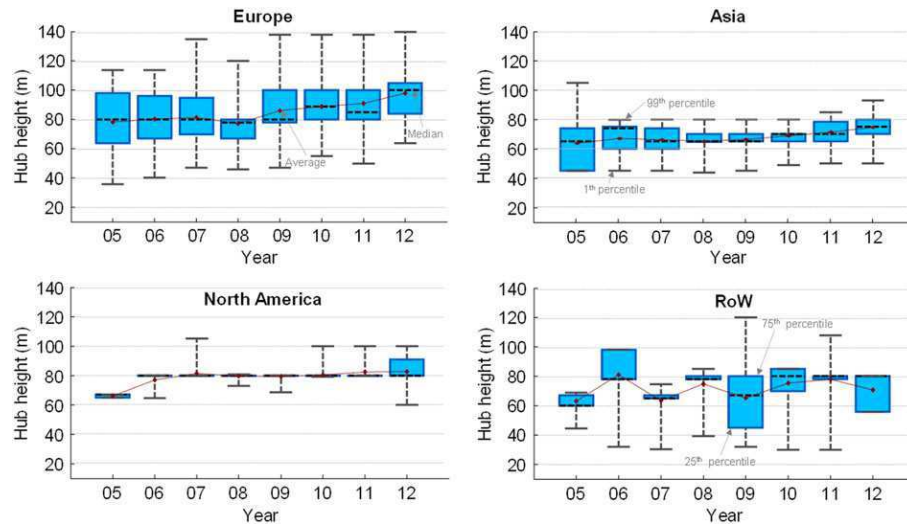
Figure 14 Box plot representation of hub heights of onshore wind turbines annually installed [20]. Source: JRC database
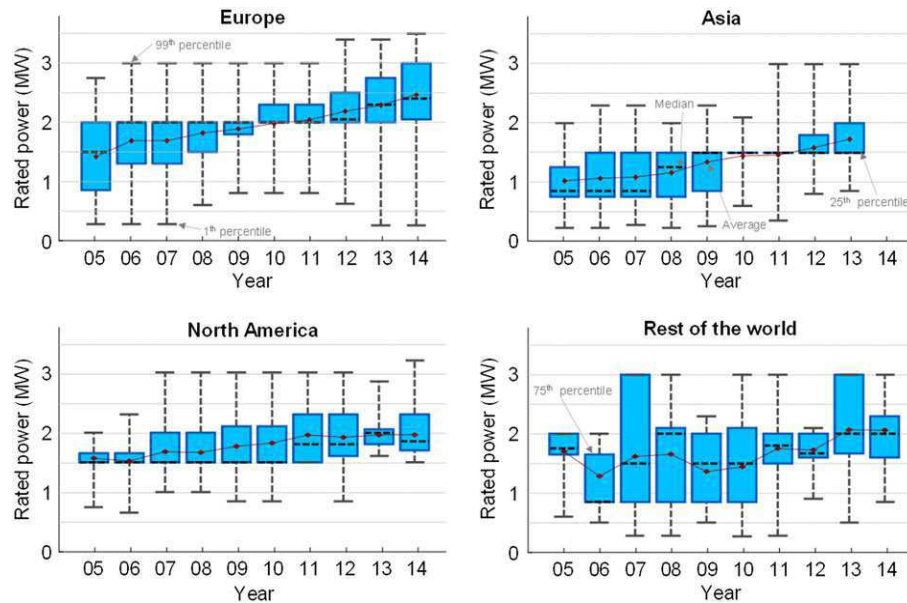
Figure 15 Box plot representation of rated power of onshore wind turbines annually installed [20]. Source: JRC database

1.4.2.b   Evolution of the drive train configurations

The HAWT can be also classified into six categories according to the generating systems and the techniques adopted to control the power production, as described in [20][22]. According to Figure 16, the six drive train configurations are:

• <u>Type A</u>: fixed speed control. An asynchronous squirrel cage induction generator (SCIG) is directly connected to the grid via a transformer. In a fixed speed control, the wind fluctuations are converted into mechanical stress and line losses, making this technique the least used.

• <u>Type B</u>: variable speed control with variable rotor resistance. This type of control uses a wound rotor induction generator (WRIG) connected in series with a variable resistance. The resistance modifies the current in the rotor and then the speed of the generator, typically in a range of +/-10 % around synchronous speed. In comparison to type A control, this solution provides higher control flexibility but the electrical losses are still relatively high and they have a circumscribed response to grid requirements.

• <u>Type C</u>: doubly-fed induction generator (DFIG). Similar to type B the current in the rotor is changed to allow a speed control. However, this configuration uses a partial-scale frequency converter for a speed control, typically in a range of +/-30 % around synchronous speed, that allows a reduction in the electrical losses and a better response to grid requirements.

• <u>Type D</u>: variable speed control of a drive train wind turbine with a full-scale frequency converter. The generator, that can be electrically excited (EESG) or permanent magnet excited (PMSG), is connected to the grid through a full-power converter. The full-power converter allows a full control of the rotational speed of the generator and it avoids to use a gearbox. This configuration connects the hub to the generator via a direct drive train, with a greater reliability and lower maintenance cost associated to gearbox failures [24].

• <u>Type E</u>: variable speed control of a gearbox-equipped wind turbine with a full converter and medium-/high-speed synchronous generator (EESG or PMSG).

• <u>Type F:</u> variable speed control of a gearbox-equipped wind turbine with a full converter and high-speed asynchronous generator (SCIG).
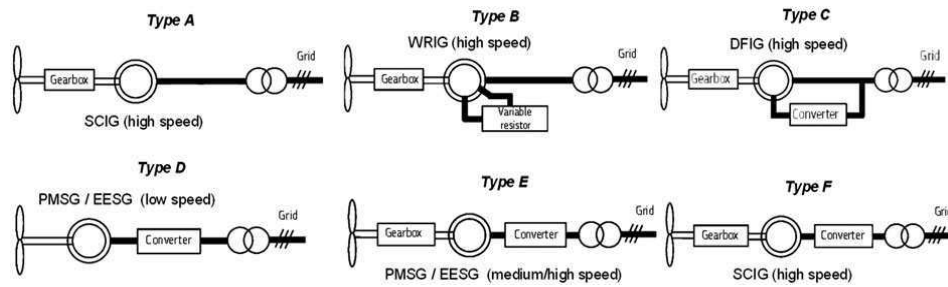
Figure 16 Wind turbine types according to drive train configuration [20]

For the six drive train configurations described above, Figure 17 shows the market share for onshore HAWT installed during 2005-2014 [20]. According to JRC data, the share is not similar all over the world; indeed, the different price of raw materials in different continents making that some drive train configurations are more competitive than other. For example, the increasing price of the row material for permanent magnet generators in Europe and North America has been reflected on a reduction of a type D-PM drive train configuration [11]. Anyway, all over the world, it can be observed that type C configuration dominates the market with an increasing trends of types D, E and F while types A and B have recorded downward trends.
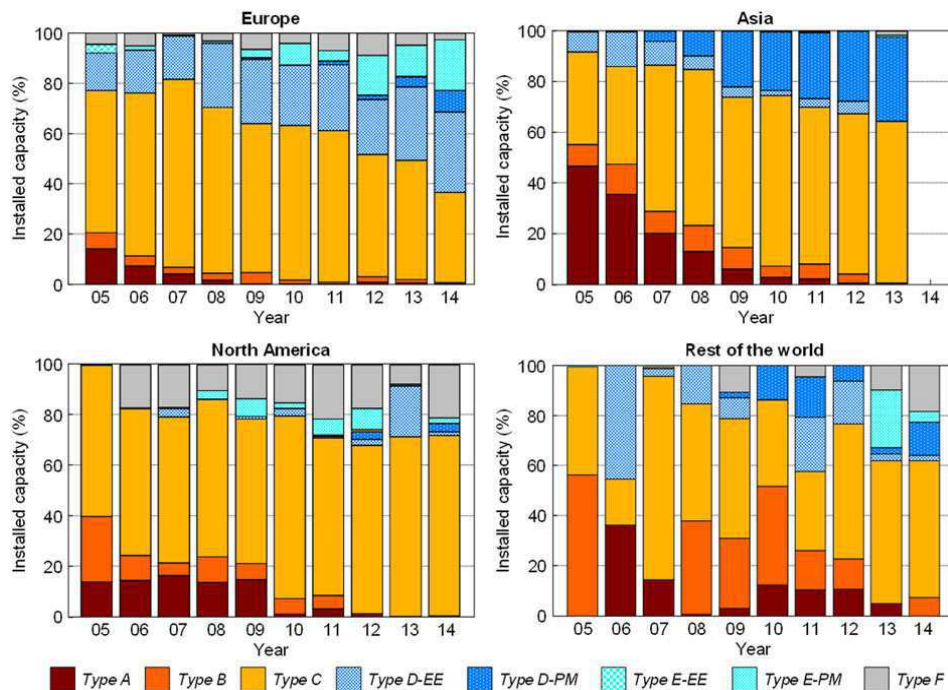
Figure 17 Evolution of the share of installed capacity by wind turbine configuration [20]. Source: JRC database

1.4.2.c   Evolution of power control

The increasing penetrations of wind energy all over the world has raised a growing interest in their control with the purpose to extract more energy from wind, to reduce the mechanical loads and to reduce wind turbine damage and costs. Therefore, the quality of power control has a direct impact on the operation and maintenance costs of wind turbine, as discussed in [23].

In order to understand the approaches to control the extracted power in a HAWT a quick overview of the power conversion is presented.

Wind turbines work to convert the available power in the wind into shaft torque and then electrical energy. The available power in the wind, P_a [W], is define as:

$$P_a = \frac{1}{2}\rho A v^3 \tag{1}$$

where ρ is the air density [Kg/m^3], A is the swept area of the rotor [m^2] and v is the wind speed [m/s].

Using the principles of conservation of momentum and energy, a complete conversion of available power can be achieved when the wind behind the wind turbine became stationary. However, since that the wind is the result of movement of air, a stationarity of wind behind the wind turbine can be reached only in no wind condition. Therefore, the wind turbine cannot extract all the energy from the wind. In 1919, Albert Betz proved that the maximum possible energy that can be extract cannot be more than 16/27, defined as Betz Limit, of the available power in the wind, P_a. However, no wind turbine has ever achieved that limit.

Actually, the energy extract from the wind turbines is define as:

$$P_t = C_p * P_a = C_p * \frac{1}{2}\rho A v^3 \tag{2}$$

Where C_p is the power coefficient and it is a function of blade pitch β and the tip speed ratio λ (i.e. the ratio between the linear speed of the tip blade and incoming wind speed). Therefore, C_p is the only parameter that power controls can change to varying power of the wind turbines.

The operating region of a wind turbines and its power control are typically divided in four regions as shown in Figure 18 [25]:

- <u>Region 1</u>, for wind speed below the cut in, the generator is turned off;
- <u>Region 2</u>, for wind speed between cut in and rated wind speed, the rotor yaw is keep perpendicular to the wind direction and the blade pitch is set at the value that produces the maximum C_p (i.e. $\beta^*=0°$). In this region, the primary goal is to maximize the power available in the wind;

- Region 3, for wind speed between the rated and cut out wind speed, pitch controller is used to regulate generator speed and to keep the HAWT at its rated power. Where the pitching should be done lightly to avoid huge loads on the drive train and on the blades;
- Region 4, for wind speed above cut out wind speed, the blade pitch is set at the value that produces the minimum C_p (i.e. $\beta^*=90°$) and the turbine is shut down to prevent damage.
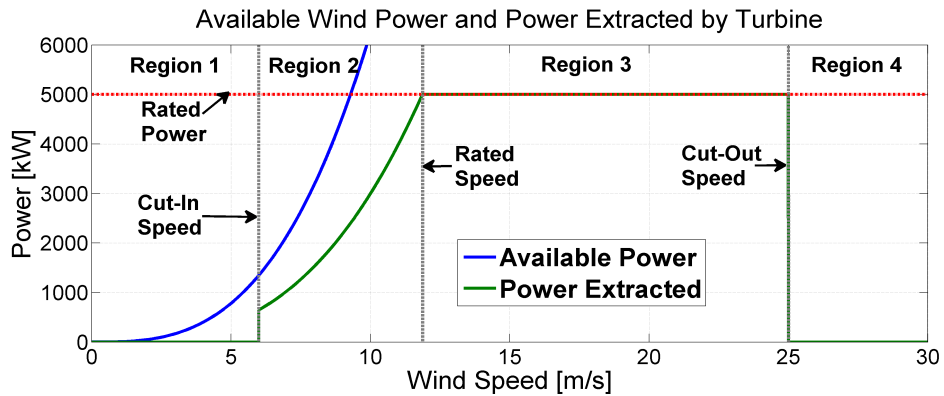
Figure 18 Wind power, turbine power, and operating regions for an example 5 MW turbine[25]

In these four regions, the primary goal of power controls is to check speed and power of the HAWT by varying the generator load torque and the blade pitch angles based on measurements of the generator shaft speed. This demonstrates how is important to measure shaft speed, usually by encoder, and shaft torque. Where, shaft speed and shaft torque have not need to be measure with high frequency, since the controls must be performed at low frequencies to avoid huge loads on wind turbine.

Wind turbine configurations can also be classified according to the power control criterion. The advantages and disadvantages of each configuration are described below:

- Passive stall control (PSC): In the years 1980-1990, passive stall control has been more used thanks its relative low cost and its simplicity. It consists on attached the blades to the hub in an optimum (nominal) attack angle. When the wind speed is less than rated wind speed, the turbine blades, with the nominal attack angle, capture the maximum possible power wind. While, for wind speeds higher than rated wind speed the design of the blade makes the airflow to stall limiting the energy captured. The drawbacks of this control are its inability to maximize the energy production for wind speed higher than rated wind speed, the high stress on

the blade in case of extreme wind and its inability to control the power during the start-up and the connection with the grid [26][27][28];

- Active stall control (ASC): In this control, when the wind speed is higher than rated wind speed, the blade pitch increases the attack of the blade, in order to achieve stall conditions, keeping the wind turbine power equal to rated power. The drawbacks of this control are the highest price of the controller [26][29][30], smother power output and assisted start-up [20];

- Pitch control (PC): In PC, blade pitch angle is decreased when the wind speed became higher than rated wind speed. A decrease of blade pitch allows to reduce the power captured by the blade, instead of stalling in ASC. The main advantages are the more facility to control transient events (as for example the start and emergency stop control) and an increase of the power up to 2% [31]. However, PC requires more sophisticated and faster control system than ASC [20];

- Individual pitch control (IPC): Many IPC strategies have been presented in the last years. They allow to reduce the impact of some load, due for example wind-shear, tower shadow, yaw misalignment and turbulence [32], on the structural fatigue damage and then on Operations & Maintenance (O&M) costs of wind turbines.

  The IPC is a control that provide an individual signal to control each blade, typically in response to measurements of flap-wise blade root bending moments. The most IPC strategies can be grouped in two distinct classes [33].

  The first class used the flap-wise blade root bending moments to reduce the loads on the non-rotating turbine structures (such as tower, nacelle and main bearing). Therefore, a coordinate transformation is required and the most used is the Colman transform[34].

  The second class used the flap-wise blade root bending moments to reduce the loads on the rotating turbine structures.

  In [33] is shown that the two classes give equivalent performance in terms of load reduction.

  The drawback of IPC control is the complexity of the algorithms, but it will become early the most widely used control technique thanks its great advantages.

For the four power control criterion described above, Figure 19 shows the market share for onshore HAWT installed during 2005-2014 [20]
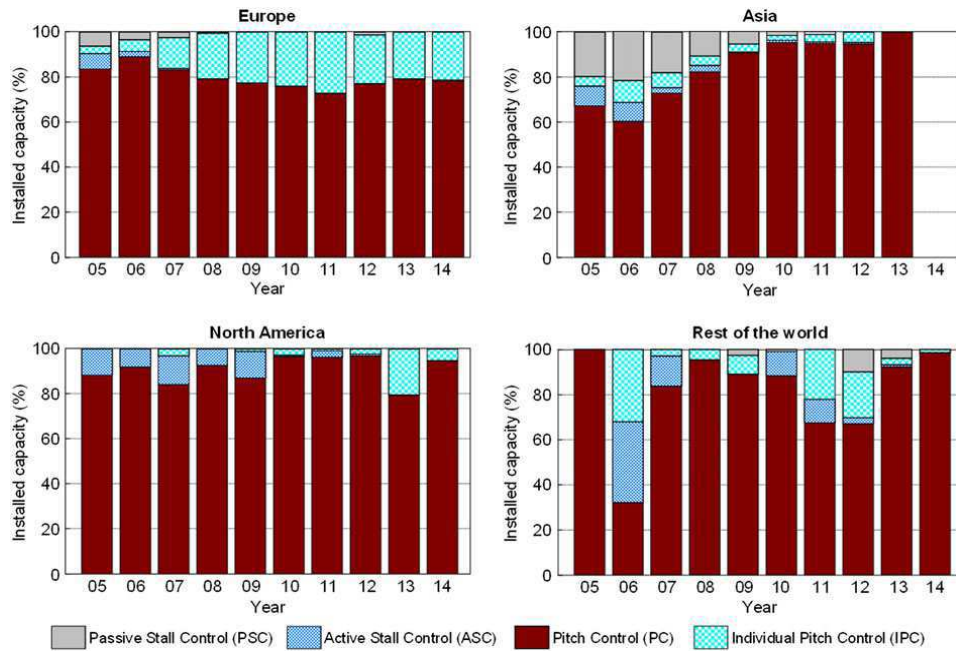
Figure 19 Evolution of power control approach of onshore wind turbines annually installed. Source: JRC database

In addition to the power control systems described above, grid operators have forced turbine manufacturers to develop controls in able to provide a regulation of the generated power based on the required power by the grid. Indeed, an unbalance between required and generated power will cause a frequency problem; in particular, if generation is greater than grid load the grid frequency will go up and conversely in the case of grid load exceeds generation. This control, Active Power Control (APC), has motivated new research opportunities and many papers have been published in recent years [35].

1.4.2.d   Share of onshore HAWT capacity installed by IEC wind classes

Turbine wind class is the parameter that represents and reassumes all possible wind turbine sites; the quantities that define a class are average annual wind speed (measured at the turbine's hub height), speed of extreme gusts that could occur over 50 years and how much turbulence there is at the wind site [37]. These classes have to consider during wind turbine design process engineers.

Table 3 reports the target values for the three wind turbine classes (IEC I, IEC II and IEC III).

Turbine Class	IEC I High Wind	IEC II Medium Wind	IEC III Low Wind	S
Annual average wind speed	10 m/s	8.5 m/s	7.5 m/s	Values specified by the designer
Extreme 50-year gust	70 m/s	59.5 m/s	52.5 m/s	
Turbulence classes	A 18%			
	B 16%			
	C 12%			

Table 3 Wind turbine classes [37]

A further wind turbine class, class S, is defined for special winds or other external conditions or a special safety class. The design values for the wind turbine class S shall be chosen by the designer [37].

Figure 20 shows the evolution of onshore HAWT installed during 2005-2014 according to different wind classes. A declining role of class I is shown; probably because windy sites were taken before 2005.
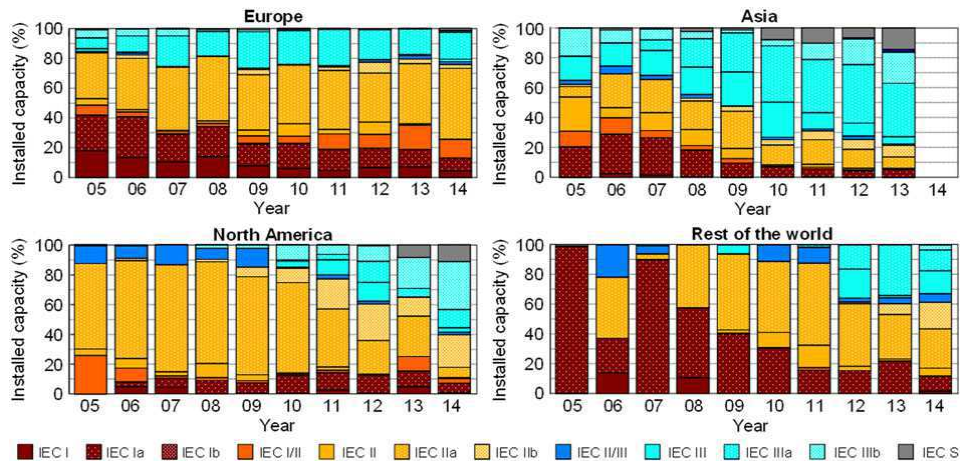
Figure 20 Evolution of the share of onshore installed capacity by IEC wind classes. Source: JRC database

1.5 Objectives of this thesis

The main objective of this thesis is to present procedures and measurement techniques applicable to the analysis of mechanical loads on HAWT wind turbines. The analysis of mechanical loads can be carried out for the purpose of: a) Design process, b) Certification and c) Continuous monitoring of structural loads in specific conditions for condition monitoring.

Concerning the certification process and design process, the standard IEC 61400-13 sets the basic requirements for a measurement campaign and it defines: 1) Wind

turbine load cases to be measured (MLCs), 2) Quantities to be measured, 3) Measurement techniques, 4) Processing guidelines.

The recording and analysis of mechanical quantities on wind turbines is a very complex task also for the continuous growth in size and power of these machines. The mechanical quantities that have to be recorded on wind turbines are bending and torsional moments, which should be measured by full strain gage bridges, as recommended by the standard. The main issues associated with the strain gage application are the calibration procedure and the uncertainty analysis. These problems will be discussed in this thesis and guidelines will be presented to deal with them.

Concerning the direct determination of structural loads in specific conditions for condition monitoring, one of the most important mechanical quantities that should be analysed is the main shaft torque. Indeed, many studies have shown that an accurate torque measurement can provide much information about the WT's health and it has been shown to be successful in detecting faults in the main drive train components. Although WT torsional effects are important, torque measurement on wind turbine shaft is a complex task today; the available solutions are uncertain (such as strain gage) or invasive (like inline torque sensors). Therefore, another aim of this thesis is to present a new contactless torque measurement system that allows to overcome the limits of existing solutions.

1.6   Structure of thesis

The objectives declared in the previous paragraph have been achieved in this thesis that is structured to reflect the direction, progress and results of the research since November 2014.

This introduction, Chapter 1, has briefly discussed the overview of the global energy market, highlighting how the expected increasing energy demand, driven mainly by the countries non-OECD, cannot be pursued through increased fossil fuels if we want to respect the Paris Agreement. Therefore, the expected development of renewable sources in the coming years is shown, with the wind energy in the foreground. Finally, this chapter has presented a quick description of what are the current wind turbine solutions and which is the market trend, focusing on HAWT.

Chapter 2 is a comprehensive review which summarises the status of WT standards and the overall architecture process for wind turbine mechanical design and turbine/project certification. Focusing the analysis on the: 1) Wind turbine load cases to be measured (MLCs), 2) Quantities to be measured, 3) Measurement techniques, 4) Processing guidelines.

Chapter 3 provides a discussion of WT reliability. Some reliability studies are presented and they show the failure rate of the turbine components and their

impact on the O&M costs. Furthermore, the current state of the art of commercial available WT CMSs, their advantages and limitations are then summarised. With a special study of the drive train condition monitoring techniques.

In Chapter 4, the focus moves from background literature in the field to describe the procedures that have to be followed to select a measurement chain and to calibrate the strain gage bridges. This chapter discusses the question for a wind turbine with a rated power output greater than 1500 kW and a rotor diameter greater than 75 m.

Chapter 5 then examines the practicalities and problems to evaluate calibration uncertainty and measurement uncertainty of WTs. For each moment, according the model presented at the previous chapter, an uncertainty analysis of the calibration process will be presented, in agreement with the ISO/IEC Guide 98-3: 2008 "Guide to the Expression of Uncertainty in Measurement". The chapter shows typical results obtained from a wind turbine with a rated power output greater than 1500 kW and a rotor diameter greater than 75 m. Furthermore, the thermal effects on strain gage bridges are also discussed, putting into evidence the influence of temperature on calibration and signal uncertainty both for full bridges in T configuration and in parallel configuration.

In Chapter 6, the focus moves from the certification process to the development of a non-intrusive torque measurement for rotating shafts of wind turbines, aimed at both certification and condition monitoring of the machine; work done at Durham University. This chapter includes detailed information on the laboratory test rig that has been built to ensure a worthwhile and advantageous experimental system, presents the measurement technique and compares two signal processing methods for torque measurement. The performance of the proposed system has been proven experimentally under both static and dynamic conditions. Finally, a feasibility analysis and a system design for two real shaft configurations and real wind turbines has been performed.

Chapter 7 presents the conclusions of this research. It also contains a discussion of future work, including investigation of potential new areas for WT-driven induction generator.

Finally, a list of references has been used in this research is presented at the end of this thesis.

2 WIND TURBINE DESIGN AND CERTIFICATION – MEASUREMENT OF MECHANICAL LOADS

Measurements of mechanical, electrical and operation quantities of wind turbine are gaining greater importance recently. Measurements quantities are useful a) as support for the design process, b) to direct determination of structural loads under specific conditions, and c) as support for a certification process.

This chapter begins by describing the status of WT standards and the overall process for wind turbine mechanical design and turbine/project certification. This is followed, in paragraph 2.5, by a discussion of the mechanical load measurements, focusing on the: 1) Wind turbine load cases to be measured (MLCs), 2) Quantities to be measured, 3) Measurement techniques, 4) Processing guidelines.

2.1 Status of WT standards

Design and certification of wind turbines is based on an interaction between design targets and measurement results as will be following described in sections 2.2 and 2.3. Design targets and measurement results must be defined and measured in accordance with IEC 61400. An overview of the IEC standard and certification procedure is given in Table 4, according to [52]. In particular, for each standard, it is given the date of publication, the edition number and title.

The International Electrotechnical Commission has published several standards for wind turbines, that can be classified in two categories: Design requirements and Performing testing.
The IEC 61400-1, IEC 61400-2, IEC 61400-3 and IEC 61400-4 standards establish the set of design requirements that should be followed to ensure that wind turbines are appropriately engineered from hazards within the planned lifetime. These standards concern most aspects of the turbine life, mainly as requirements for the safety system, environmental conditions, load case definitions, safety factors and site conditions before construction. While the standards from IEC 61400-11 to IEC 61400-26 define the procedure that must be followed to perform tests.
However, regarding the procedure for wind turbine design, it is also important to mention the GL's wind guideline, originally published in 1993 and revised in 2005 and 2010.

Standard	Date	Edition	Title
IEC 61400-1	2005	3	Design Requirements
IEC 61400-1 Amendment 1	2010	3	Design Requirements
IEC 61400-2	2013	3	Small wind turbines
IEC 61400-3	2009	1	Design requirements for offshore wind turbines

IEC 61400-4	2012	1	Design requirements for wind turbine gearboxes
IEC 61400-11	2012	3	Acoustic noise measurement techniques
IEC 61400-12-1	2017	2	Power performance measurements of electricity producing wind turbines
IEC 61400-12-2	2013	1	Power performance of electricity-producing wind turbines based on nacelle anemometry
IEC 61400-12-2 Corrigendum 1	2016	1	Power performance of electricity-producing wind turbines based on nacelle anemometry
IEC 61400-12-3	2006	1	Wind farm power performance testing
IEC 61400-13	2015	2	Measurement of mechanical loads
IEC/TS 61400-14	2005-03	1	Declaration of apparent sound power level and tonality values
IEC 61400-21	2008-08	2	Measurement and assessment of power quality characteristics of grid connected wind turbines
IEC 61400-22	2010	1	Conformity testing and certification
IEC 61400-23	2014	2	Full-scale structural testing of rotor blades
IEC 61400-24	2010	1	Lightning protection
IEC 61400-25-1	2006	1	Communications for monitoring and control of wind power plants - Overall description of principles and models
IEC 61400-25-2	2015	2	Communications for monitoring and control of wind power plants - Information models
IEC 61400-25-3	2015	2	Communications for monitoring and control of wind power plants - Information exchange models
IEC 61400-25-4	2016	2	Communications for monitoring and control of wind power plants - Mapping to communication profile
IEC 61400-25-5	2017	2	Communications for monitoring and control of wind power plants - Compliance testing
IEC 61400-25-6	2016	2	Communications for monitoring and control of wind power plants - Logical node classes and data classes for condition monitoring
IEC 61400-26-1	2011	1	Time-based availability for wind turbine generating systems
IEC TS 61400-26-2	2014	1	Production-based availability for wind turbines
IEC 61400-27-1	2015	1	Electrical simulation models - Wind turbines

Table 4 Status of IEC standard and certification procedure [52]

2.2 Approach for wind turbine mechanical design

The design approach is a methodical series of steps that designers use to develope wind turbines. It is a decision making process highly iterative, which requires the comparison of project data with measured data before a correction is applied to the project. The iterative process can be applied to many aspects of the wind turbine (electrical, mechanical, noise emission, aerodynamics and operating parameters), however mechanical design is the most critical in the overall design and is therefore what will be described in detail below.

The design process regarding mechanical quantities can be split, as shown in Figure 21, up into three steps: *Define the load cases*; *Determination of component design loads and design stresses*; *Serviceability analysis and limit state analysis*. These 3 steps can be split again up into two groups according to the kind of standards and guidelines. In particular, steps 1 and 2 use Wind Energy Specific Standards and Guidelines, while Common Standards and Guidelines are used for step 3.
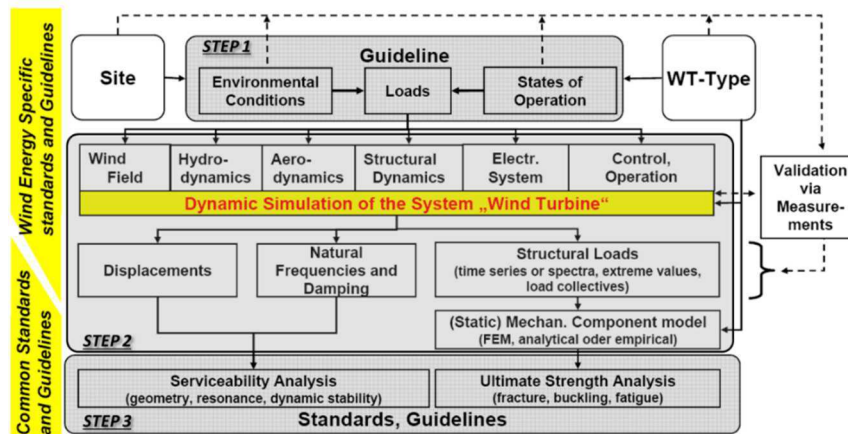
Figure 21 Wind turbine design process [53][51]

Step 1: *Define the load cases*

Definition of the Design Load Cases (DLCs). DLCs are all machine conditions and meteorological conditions (wind speed and turbulence) that have to be simulated during WT design to establish, at next step, the design loads. DLCs are defined by the GL's wind guidelines or by the standards from IEC 61400–1 to IEC 61400–4. In particular, IEC Design Load Cases are defined for eight situations [50] (See also Table 5):

- Power production under normal conditions;
- Power production with an operational fault;
- Start up;
- Normal shut down;

- Emergency stop;
- Parked (Rotor stopped or idling);
- Parked with operational fault;
- Transport, maintenance and repair.

These DLCs must be repeated for different wind velocity and turbulence intensity.

The IEC specified load cases are minimum requirements and the wind turbine manufacturer can add DLCs if it finds appropriate during the design process, although all damaging load cases of wind turbines should be covered under the eight categories.

Design situation	DLC	Wind condition		Other conditions	Type of analysis	Partial safety factors
1) Power production	1.1	NTM	$V_{in} < V_{hub} < V_{out}$	For extrapolation of extreme events	U	N
	1.2	NTM	$V_{in} < V_{hub} < V_{out}$		F	*
	1.3	ETM	$V_{in} < V_{hub} < V_{out}$		U	N
	1.4	ECD	$V_{hub} = V_r - 2$ m/s, V_r, $V_r +2$ m/s		U	N
	1.5	EWS	$V_{in} < V_{hub} < V_{out}$		U	N
2) Power production plus occurrence of fault	2.1	NTM	$V_{in} < V_{hub} < V_{out}$	Control system fault or loss of electrical network	U	N
	2.2	NTM	$V_{in} < V_{hub} < V_{out}$	Protection system or preceding internal electrical fault	U	A
	2.3	EOG	$V_{hub} = V_r \pm 2$ m/s and V_{out}	External or internal electrical fault including loss of electrical network	U	A
	2.4	NTM	$V_{in} < V_{hub} < V_{out}$	Control, protection, or electrical system faults including loss of electrical network	F	*
3) Start up	3.1	NWP	$V_{in} < V_{hub} < V_{out}$		F	*
	3.2	EOG	$V_{hub} = V_{in}, V_r \pm 2$ m/s and V_{out}		U	N
	3.3	EDC	$V_{hub} = V_{in}, V_r \pm 2$ m/s and V_{out}		U	N
4) Normal shut down	4.1	NWP	$V_{in} < V_{hub} < V_{out}$		F	*
	4.2	EOG	$V_{hub} = V_r \pm 2$ m/s and V_{out}		U	N
5) Emergency shut down	5.1	NTM	$V_{hub} = V_r \pm 2$ m/s and V_{out}		U	N
6) Parked (standing still or idling)	6.1	EWM	50-year recurrence period		U	N
	6.2	EWM	50-year recurrence period	Loss of electrical network connection	U	A
	6.3	EWM	1-year recurrence period	Extreme yaw misalignment	U	N
	6.4	NTM	$V_{hub} < 0,7 \ V_{ref}$		F	*
7) Parked and fault conditions	7.1	EWM	1-year recurrence period		U	A
8) Transport, assembly, maintenance and repair	8.1	NTM	V_{maint} to be stated by the manufacturer		U	T
	8.2	EWM	1-year recurrence period		U	A

The following abbreviations are used in Table 2:	
DLC	Design load case
ECD	Extreme coherent gust with direction change (see 6.3.2.5)
EDC	Extreme direction change (see 6.3.2.4)
EOG	Extreme operating gust (see 6.3.2.2)
EWM	Extreme wind speed model (see 6.3.2.1)
EWS	Extreme wind shear (see 6.3.2.6)
NTM	Normal turbulence model (see 6.3.1.3)
ETM	Extreme turbulence model (see 6.3.2.3)
NWP	Normal wind profile model (see 6.3.1.2)
$V_r \pm 2$ m/s	Sensitivity to all wind speeds in the range shall be analysed
F	Fatigue (see 7.6.3)
U	Ultimate strength (see 7.6.2)
N	Normal
A	Abnormal
T	Transport and erection
*	Partial safety for fatigue (see 7.6.3)

Table 5 Design Load Cases (DLCs) [37]

Step 2: Determination of component design loads and design stresses

For each DLCs listed in Table 5, simulations have to be performed by using dedicated programs like e.g. BLADED, Flex5, HawC, FOCUS, ADAMS, SAMCEF and SIMPACK [51]. These programs allow to create a database of wind turbine loads classified as [54]:

- Static loads like e.g.:
  - ✓ Weight;
  - ✓ Steady rotation.
- Dynamic loads like e.g.:
  - ✓ Transients (e.g. start /stop manoeuvres, accelerations, grid connection, grid fault, change in average wind speed);
  - ✓ Cyclic /periodic (e.g. wind shear, tower shadow, blade mass);
  - ✓ Stochastic (e.g. turbulence).

From the database of wind turbine loads, the designer defines the component design loads based on the worst case scenario. Specifically, the project parameters that must be taken into account when dimensioning the components are: maximum loads; number of stress cycles for fatigue design; excitation frequencies due to wind or rotating parts for dynamic analysis; usually multiple DLCs are required to design a single component.

Step 3: *Serviceability analysis and limit state analysis*

Validation of project data (Displacements, Natural Frequency and Damping) with measured values is accomplished at the last step. In order to allow this comparison, the measurement process involves the acquisition of mechanical, meteorological,

electrical and WT operation quantities for specific machine operating conditions (Measurement Load Case MLCs). The load measurement program shall be congruent with the design load cases used in the design assessment of the wind turbine. Therefore, the load measurement program shall include all normal and abnormal operating conditions (e.g. emergency shut down, loss of grid, protection system fault, etc.) for the design wind speed range and intense turbulence range. This procedure, regulated by IEC 61400-13, is described in section 2.4. The validation of project data with measured values must be accomplished through the following modes [51]:

1. Component design strength: Comparison between the maximum design loads and the maximum measured loads. A safety factor must be considered in the comparison. In particular, the IEC provides the list of partial safety factors for loading, materials and component classes;
2. Limit state analysis: Load spectra corresponding to lifetime operation. Since acquired data are not statistically significant to describe lifetime operation of the machine (designed for 20 years), the number of cycles of the load spectra obtained from measurement campaign have to be weigh with the Weibull distribution. Where, Weibull distribution gives a graphical representation of how often the wind blows at a certain speed. This allows to compare measured load spectra comparable with the design load spectra;
3. Resonance analysis: Resonance analysis allows to identify resonance problems, usually due to the interaction between wind turbine drive train components. A Campbell diagram is often used to performed this analysis. The resonance analysis only considers internal component dynamics. The results of resonance analyses are not linked to the wind turbine external loadings [51].

If the project data and the measurement results are consistent, for each of the three modes listed above, the wind turbine design can be approved.

2.3 Turbine and project certification practice

According to the international standard ISO/IEC 17000 [56], certification is the attestation related to the conformity of products, processes, systems or persons. The decision to issue the certificate is based on the verification of the suitability, adequacy and effectiveness of selection and determination activities, and the results of these activities to the fulfilment of specified requirements. The certification shall be carried out by third-party test institutes accredited according to ISO 17025 [57].

Certification of wind turbines play an important role in minimizing the number of design errors, minimizing cost of energy, maximizing reliability and building up

confidence in the industry among manufacturers, developers, owners, finance and insurance companies, and regulatory authorities. International standards and guidelines are in force to carry out Type Certification and Project Certification of wind turbine. The most important guideline to certificate onshore and offshore wind turbines and wind farms is the IEC TS 61400-22 [55].

2.3.1 Wind turbine type certification

Type Certificate provides the verification to a generic wind turbine and is not related to a certain site. According to [51], to obtain a Type Certificate the modules shown in Figure 22 are to be carried out.
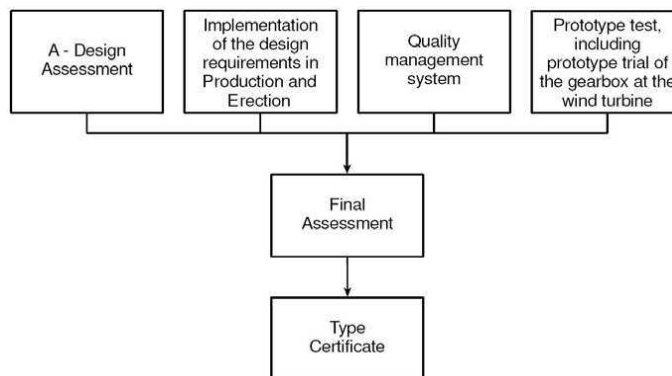
Figure 22 Modules of Type Certification [51]

The type certification, regulated by the GL-IV-1 / GL-IV-2 guidelines or the IEC 61400-22 standard or national standard, is usually composed of 4 modules:

- *Design Assessment*, it consists of a complete examination of the Design Requirements according to the standards from IEC 61400–1 to IEC 61400–4 or GL's wind guideline. In particular, the following documents in the form of specifications, calculations, drawings, descriptions and/or parts lists are to be assessed:
  ✓ control and safety concept;
  ✓ load case definitions / load assumptions;
  ✓ safety system;
  ✓ rotor blades and blade test reports;
  ✓ mechanical structures including nacelle housing and spinner;
  ✓ machinery components;
  ✓ electrical installations, including lightning protection;
  ✓ tower and, optionally, foundation;
  ✓ manuals for erection, commissioning, operating and maintenance;
  ✓ other optional items like personnel safety.

- *Implementation of the design-related requirements in Production and Erection (IPE)*, the manufacturer of the components and the manufacturer of the wind turbine shall ensure, to the certification body, that the requirements set in the technical documentation are observed during production and erection of the wind turbine.
- *Quality management system*, the designer and manufacturer shall ensure, to the certification body, that meet the requirements of ISO 9001 with regard their work.
- *Prototype tests*, Tests and measurements have to be carry out to validate the design calculations, to optimise control, performance and noise behaviour and to verify the performance of the safety and control systems. These tests and measurements are regulated by standards as shown in Table 6.

Topics for Measurements	Codes or standards to be applied
Noise Emissions (other tests)	IEC 61400-11 [61]
Power Performance Measurements (Power Curve)	IEC 61400-12 [60]
Load Measurements	IEC TS 61400-13 [50]
Electrical Characteristics (other tests)	IEC 61400-21 [62]
Blade Tests	IEC TS 61400-23 [63]
Safety and Function Tests/Commissioning	GL Wind Guideline [64]

Table 6 Wind turbine standards for prototype tests

2.3.2 Project certification

Project certification is carried out for wind turbines having successfully received type certification and for locations for which the necessary data are available. Basically project certification is intended for projects covering more than one single wind turbine such as wind farms onshore as well as offshore [58]. According to [51], to obtain a project certificate the modules shown in Figure 23 are to be carried out.
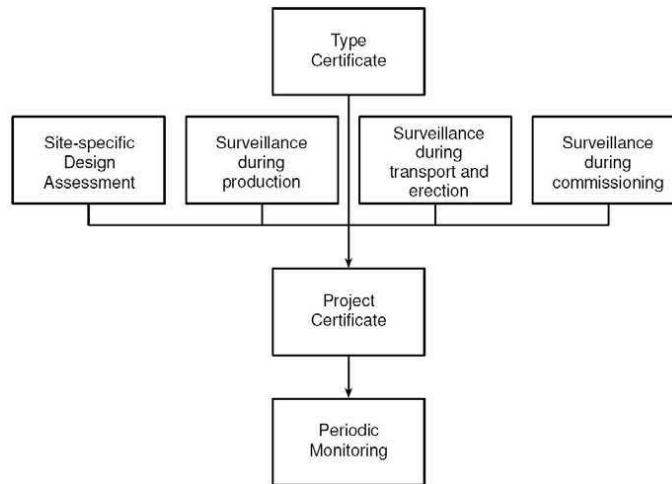
Figure 23 Modules of Project Certification [51]

The project certification, regulated by the GL-IV-1 / GL-IV-2 guidelines or the IEC 61400-22 standard or national standard, is usually composed of 4 modules:

- *Site-specific design assessment*, it consists to checking and comparing the site conditions with the parameters used for the design assessment in type certification of wind turbine.
- *Surveillance during production*, the surveillance during production inspects and tests materials and components, according to ISO 9001 Quality Management System. The manufacturer shall ensure this surveillance otherwise surveillance may be done by a certification body.
- *Surveillance during transport and erection*.
- *Surveillance during commissioning*, before operation phase, all components related to operation and safety are being inspected and/or tested through previously approved procedures.

The certification body issues the project certification and it does not expire as long as the Periodic Monitoring is carried out at regular intervals. Major modifications, conversions or repairs not approved by the certification body affect the validity of the certificate [58].

2.4 Mechanical validation via measurements

In certification and product design processes, design data shall be compare with measurements. Several standards are currently used to measure physical quantities of wind turbines (electric, aerodynamic, acoustic and mechanical). In this thesis, the main focus is on mechanical measurements, standardized by IEC 61400-13. Some criticisms are subjected into the standard [37], as I have declared in [59],

mostly solved or declared in the new version [50] updated in 2015, during my second year of PhD.

Hereafter are reported, according to the new standard, the four basic requirements to perform a mechanical measurement campaign; while an application of the standard in a real case will be presented in chapters 4 and 5 of the thesis.

1)   Wind turbine load cases to be measured (MLCs)

The Measurement load cases (MLCs), that define load measurement program, shall be congruent with the design load cases (DLCs) defined and used in the general design assessment of the wind turbine. The MLCs define the main external conditions and the operational conditions of the turbine during the measurement campaign. The external conditions include meteorological quantities such as wind speed, turbulence intensity and air density. The operational conditions include operational quantities such as rotational speed, yaw misalignment, electrical power and blade pitch angle. The operational conditions depend on the wind turbine configuration and shall be specified for each particular case.

The standard identifies 7 MLCs:

1. Power production;
2. Parked;
3. Start-up;
4. Normal shutdown;
5. Emergency shutdown;
6. Grid failure;
7. MLCs for dynamic characterization.

That are classifiable in 3 groups: MLCs during steady-state operation (Power production and Parked), MLCs during transient events (Start-up, Normal shutdown, Emergency shutdown, Grid failure) and MLCs for dynamic characterization. Capture matrix, one for each MLC, specifies the minimum number of 10-minute time series that have to be acquired.

The IEC specifies the minimum MLCs and time series for each MLC that have to be measured; however, the accredited certification institute can add MLCs or number of time series to increase the reliability of the results.

2)   Quantities to be measured

Mechanical load magnitudes (Table 7), wind inflow (Table 8) as well as WT operational parameters (Table 9) must be recorded for each MLCs during the certification process. The standard defines mandatory and recommended quantities but it is not restrictive in terms of quantities to be measured. In fact, the

accredited certification institutes can add some quantities if it finds appropriate during the certificate process.

Different quantities have to be measured according to the turbine in analysis. In particular, the parameters given in Table 7 are referred to wind turbines with a rated power output greater than 1500 kW and a rotor diameter greater than 75 m; which represents the case under analysis in this thesis.

Load quantities [50]	Level of importance [50]	Sampling Frequency (not prescribed by IEC) [51]
Blade flatwise bending moment distribution	2 blades mandatory, 1 blade recommended	≥ 64 samples/s
Blade edgewise bending moment distribution	2 blades mandatory, 1 blade recommended	≥ 64 samples/s
Blade root flatwise bending moment (Mbf)	2 blades mandatory, 1 blade recommended	≥ 64 samples/s
Blade root edgewise bending moment (Mbe)	2 blades mandatory, 1 blade recommended	≥ 64 samples/s
Blade torsional frequency and damping	Recommended	≥ 64 samples/s
Pitch actuation loads	One blade mandatory	≥ 64 samples/s
Rotor tilt moment (Mtilt)	Mandatory	≥ 64 samples/s
Rotor yaw moment (Myaw)	Mandatory	≥ 64 samples/s
Rotor torque (Mx)	Mandatory	≥ 64 samples/s
Tower base normal moment (Mtn)	Mandatory	≥ 64 samples/s
Tower base lateral moment (Mtl)	Mandatory	≥ 64 samples/s
Tower mid normal moment (Mtmn)	Recommended	≥ 64 samples/s
Tower mid lateral moment (Mtml)	Recommended	≥ 64 samples/s
Tower top normal moment (Mttn)	Mandatory	≥ 64 samples/s
Tower top lateral moment (Mttl)	Mandatory	≥ 64 samples/s
Tower torque (Mttt)	Mandatory	≥ 64 samples/s

Table 7 Wind turbine load quantities for turbines with a rated power output greater than 1500 kW and rotor diameter greater than 75 m

Meteorological quantities [50]	Level of importance [50]	Sampling Frequency (not prescribed by IEC) [51]
Wind speed at hub height	Mandatory	≥ 1 samples/s
Vertical wind shear (below hub height)	Mandatory	≥ 1 samples/s

Vertical wind shear (above hub height)	Recommended	≥ 1 samples/s
Vertical wind veer	Recommended	≥ 1 samples/s
Upflow angle / flow inclination angle near hub height	Recommended	≥ 1 samples/s
Turbulence intensity (horizontal) at hub height	Mandatory	≥ 1 samples/s
Wind direction at hub height	Mandatory	≥ 1 samples/s
Air density	Mandatory	≥ 1 samples/s
Turbulence intensity (3D) at hub height	Recommended	≥ 1 samples/s
Icing potential	Recommended	≥ 1 samples/s
Atmospheric stability	Recommended	≥ 1 samples/s

Table 8 Meteorological quantities

Operation quantities [50]	Level of importance [50]	Sampling Frequency (not prescribed by IEC) [51]
Electrical power	Mandatory	≥ 1 samples/s
Rotor speed or generator speed	Mandatory	≥ 64 samples/s
Yaw misalignment	Mandatory	≥ 1 samples/s
Rotor azimuth angle	Mandatory	≥ 64 samples/s
Pitch position of all instrumented blades turbine controller output	Mandatory for all instrumented blades Recommended for all blades	≥ 64 samples/s
Pitch speed	Mandatory	≥ 64 samples/s
Brake status	Mandatory	≥ 1 samples/s
Brake moment (if not possible, brake pressure) [a]	Recommended	≥ 1 samples/s
Wind turbine status	Mandatory	≥ 1 samples/s
NOTE Pitch speed can be derived from pitch position		
[a] If the mechanical braking device is part of the primary braking system (e.g. at stall controlled turbines), the measurement of the brake moment is mandatory.		

Table 9 Wind turbine operation quantities

3)   Measurement techniques

The standard IEC 61400-13 defines the guidelines to be followed for measuring mechanical loads, including sensor selection, application practices, calibration procedures, and uncertainty analysis. While, IEC 61400-12, IEC 61400-21 and IEC 61400-22 defines the guidelines for meteorological, electrical and operating measurements.

The load sensors that can be used for wind turbine applications include, but are not limited to:

- strain gauge bridges;
- load cells / torque tubes (including piezoelectric cells).

For wind turbines, it will be seldom possible to place a load cell in a main load path. The strain gauges applied to the structure are selected as the recommended type of sensor, although a calibration procedure is required and the measurement uncertainty may not always be satisfactory. These aspects will be discussed in detail in Chapter 4.

The sampling frequency is prescribed to be at least eight times higher than any significant frequency in the relevant signal, while analogue filters with a cut-off frequency of at least three times higher than any significant frequency in the relevant signal shall be used. About that, in Table 7, Table 8 and Table 9 are reported the recommended sampling frequency for each measured quantity according to [51].

4)   Processing guidelines

The processing guidelines refer to procedures for data validation and selection, data analysis and presentation and reporting formats.

3 MONITORING OF WIND TURBINES

As described in chapter 0, wind turbines are one of the major sources of renewable electricity generation and are set to play a main role in the future energy scenarios for many countries. A growing interest in recent years has emerged around the possibility of exploiting the wind resource offshore. However, the limitations associated with offshore installations are the longer times and greater costs of repair related to faults; in general, according to [77], the operational expenditure of wind turbines amounts to approximately 20-35% of their life-cycle cost.

Maintenance strategies have to be performed to achieve a reduction of cost of wind energy, based on condition monitoring. These strategies verify machine conditions and ensure that there aren't deviations from the normal behaviour, since deviations are often produce to developing faults.

This chapter is structured in four sections. section 3.1 provides the definitions of reliability, cost of energy and maintenance strategies. Section 3.2 presents a statistical analysis of the reliability and failure of wind turbines. Section 3.3 defines the structure of Wind Turbine Monitoring systems. Finally, Section 3.4 presents a review on the state-of-the-art of data acquisition techniques for condition monitoring of wind turbines; in particular, challenges and limitations of the current systems. Specifically, section 3.4 introduces before the techniques currently used and subsequently the further techniques, all with a major focus on drivetrain condition monitoring.

3.1 Concepts and Definitions

Development and deployment of wind turbine technology can only take place through a continuous improvements of diagnostic systems. Diagnostic systems allow a predictive evaluation of failures, avoiding long machine stops that cause an increase in O&M costs and in the Cost of Energy. Therefore, diagnostic systems will have a major impact on lowering turbine reliability and will be a critical factor for the economic success of a wind power project.

3.1.1 Reliability

Reliability is the probability that the designed system will function correctly under stated condition for a given time [66][67]. In general, the reliability can be defined at zero-time conditions and in service. In the first case, it is the ability of the system to work properly when it is new and it depends on the system design and manufacture technique used to generate it. While, the reliability in service is function of time, beginning at zero time, and depends by degrade of its parts during use [65].

Reliability is usually expressed as the probability of success, i.e. the mean time between failures (MTBF), or the frequency of failure $f_f(t)$ [68]. Where MTBF $f_f(t)$ are given by equation (3) and (4), respectively:

$$MTBF = \frac{Operational\ hours\ (h)}{Number\ of\ failures} \tag{3}$$

$$f_f = \frac{1}{MTBF} \tag{4}$$

Figure 24 shows a typical failure rate $f_f(t)$ versus time in wind turbine and in general mechanical system [68][69], well known as "bathtub curve".
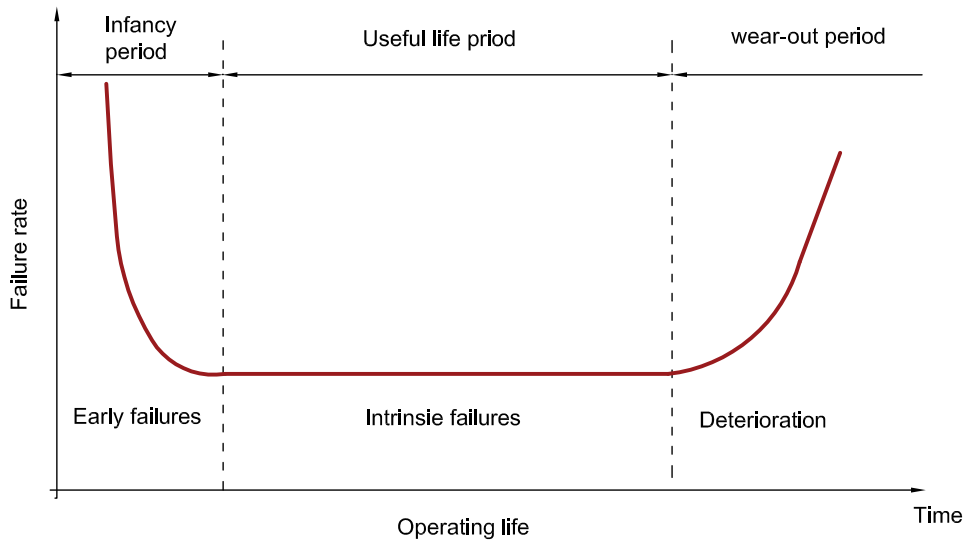
Figure 24 Typical bathtube curve

The bathtub curve is characterized by three failure rate patterns, a decreasing failure rate, constant failure rate and an increasing failure rate. This three failure rate descried three different zone:

- *Infancy period zone* is normally characterized by a high failure rate. This is normally due to poor design, the use of substandard components, or lack of adequate controls in the manufacturing process;
- *Useful life period zone* is characterized by a constant failure rate. These failures occur when the stress levels exceeded the design levels due to random, chance causes or a no good preventive maintenance practices;
- *Wear-out period zone* is characterized by an increasing failure rate as the result of system deterioration due to age or use.

However, the most relevant parameter to measure the reliability is the availability. The availability *Av(t)*, given by equation (5), is define as the probability that a component or system is capable of functioning at time [70].

$$Av = \frac{MTTF}{MTTF + MTTR}$$
(5)

Where *MTTF* is the mean time to failure and *MTTR* is the mean time to recovery.

The reliability is a primary parameter in wind energy. Indeed, it affects the capacity of Wind Turbine to work and to extract the maximum energy available from the wind during its life. Reliability can be improved by the implementation of wind turbine monitoring structure (i.e. SCADA, SHM and CMS), as described below.

3.1.2 Cost of Energy

Cost of energy is a widely used metric for comparing power plant system alternatives. The CoE is given by equation (6) [69][71], where *ICC* is the Initial Capital investment Cost; *FRC* is the annual Fixed Charge Rate; LRC is Levelized Replacement Cost; A*E* is the Annual Energy production in *kWh*; and *OM* is the annual Operation and Maintenance cost.

$$CoE = \frac{ICC * FCR + LRC + OM}{AE}$$
(6)

The OM costs, that include the costs for insurance, periodic and unscheduled maintenance, spare parts, grid connection and administration, are the only variable costs and then the only parameters that can change the energy profit. The OM costs generally increase during the system life because the possibility of failures increase year by year.

Concerning WT, the OM costs are relatively low compared to thermal power plants because of zero fuel costs. In particular, OM costs still account for 20-25% of CoE [72] and they are obviously dependent on the maintenance strategy, effectiveness of the monitoring structure adopted by the user, the selection of technology and the characteristic of the site. In particular, Table 10 reports the OM costs for offshore and onshore installation in Europe [73] and onshore installation in North America [74]. Obviously, the OM costs of offshore wind are double than onshore wind due to the higher costs for accessing and maintaining the site at sea [73].

Region	Onshore	Offshore
	USD/kWh	
North America	0.005 ÷ 0.015	-
Europe	0.013 ÷ 0.025	0.027 ÷ 0.054

Table 10 OM cost in North America and Europe [73],[74]

The costs of wind energy production have to be at least compatible with the costs of energy production from conventional sources to make wind turbine system commercially acceptable. Figure 25 compares the weighted average CoE and range of renewable power generation technologies in different regions of the world. The CoE of WT is in line with the other renewable power generation technologies. However, there are significant differences in cost in different regions due to the very site-specific nature of renewable resources. In particular, China and India have the most competitive renewable wind energy generation thanks to the large number of project that have allowed to reduce the cost and to make wind energy a very competitive technology even for sites where the wind resource is not ideal [74].
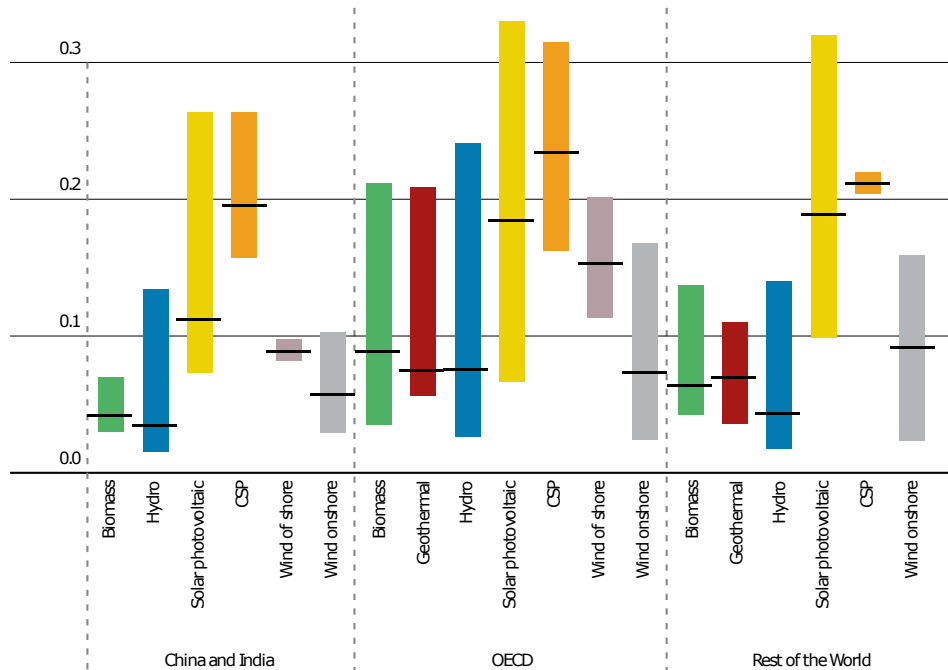
Source: IRENA Renewable Cost Database.

Figure 25 Cost of electricity by region and technology and their weighted average 2013/2014[74]

The wind speed offshore is higher than onshore, so the offshore WT are usually more efficient than onshore WT. However, this more efficient is not able to compensate its higher cost and the CoE for offshore WT is typical higher than

MONITORING OF WIND TURBINES

onshore WT. According to Figure 25 [74], the CoE range for onshore and offshore WT are [0.02 ÷ 0.17] and [0.08 ÷ 0.21], respectively.

Figure 26 shows an interesting comparison among the CoE for the power generation technologies in 2014 and 2025. IRENA [74] expects a general decrease of all renewable resources and it evaluates onshore wind energy the cheapest energy technology in future. Where, the CoE reduction will be driven by the development of larger wind farm and technological improvements; improvements that include monitoring systems to understand failure rates, forestalling failures, managing efficient repairs and replacements.
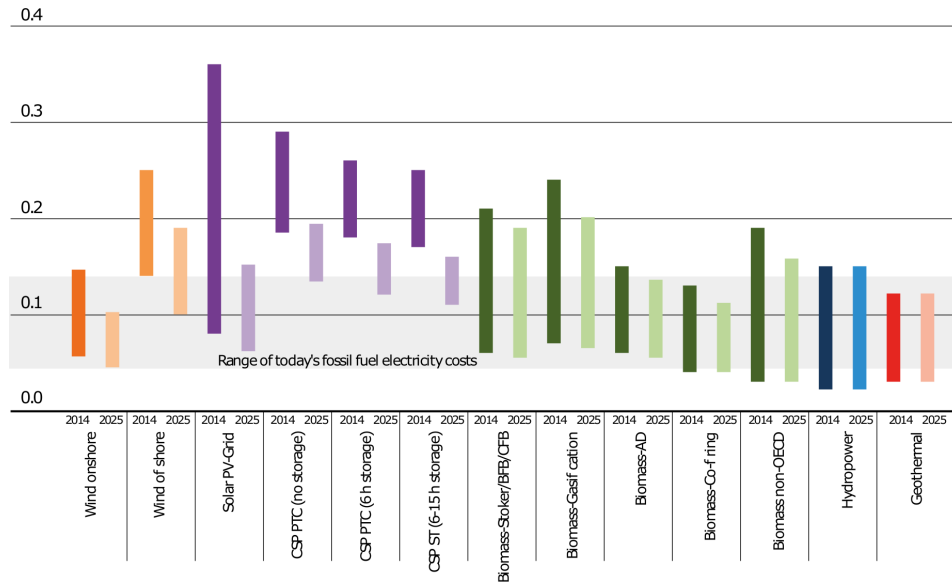
Figure 26 CoE ranges by renewable power generation technology, 2014 and 2025 [74]

3.1.3 Maintenance strategies

Today, industry is forced to increase the efficiency of its products through the implementation of maintenance strategies in order to be competitive [76]. Maintenance strategies is a management method used to achieve the maintenance objectives, i.e. the targets assigned to or accepted by the management and maintenance department. These targets may include availability, cost reduction, product quality, environment preservation, safety [75].

In most industries, as well as WT industry, maintenance strategy can be classified into three main groups, according to EN 13306 [75]:

- Preventive or periodic maintenance (time-based);
- Predictive maintenance (condition-based);

- Reactive or corrective maintenance (run to failure).

The three strategies have a different influence on asset condition [77] and different cost [69], see Figure 27 and Figure 28.

In preventive or periodic maintenance strategy, parts of the system are replaced or repaired according to their expected breakpoints, usually defined as total operating hours, machinery age, number of start-ups and shut-downs. The advantages of this strategies are: schedulability, an efficient spare-part management, low potential failure and therefore a low repair cost. However, the waste of lifetime in cases when components could have lasted longer increases the prevention cost [77].

In reactive or corrective maintenance strategy, repair or replacement are performed after a breakdown. Unlike what happens for periodic maintenance, this strategy uses the whole life of the component and the prevention cost is low. However, the machine is typically affected with long downtimes with the risk of a secondary and catastrophic failure [77]. Therefore, typically reactive and corrective maintenance strategy have high repair costs.

Predictive maintenance can be considered a good compromise between the two solutions described above. In this case, expert operators define the expected operating hours of machine components based on condition monitoring analysis. The condition monitoring is based on an early detection of faults followed by maintenance that prevents severe damage [77]; in practice, it allows to prevent 99% of failures [78]. This strategy is the most cost-effective maintenance strategy because minimize the total cost (i.e. the sum of prevention cost and repair cost) even if it requires resource and research investment.
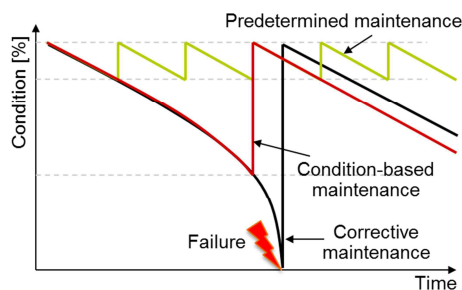
Figure 27 Influence of the maintenance strategy on asset condition [77]
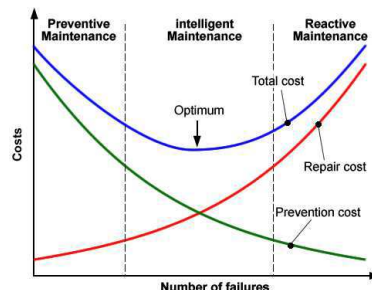
Figure 28 Costs associated with the three maintenance strategies [69]

3.2 Reliability and failure statistics of wind turbine

WTs reliability, as well as any machine, is affected by the reliability of their components. Studies and publications on WTs reliability have been made in recent years; the most important projects are Finisch Wind Turbine Statistics, Swedisch Wind Turbine Statistics, Windstats (Germany & Denmark), WMEP and Realwind.

These projects have allowed to develop databases containing failures in several wind farms overall project lifetime. Some publications have been made, however, the first databases, such as the Finisch Wind Turbine Statistics, Swedisch Wind Turbine Statistics, Windstats (Germany & Denmark) and WMEP, had important limitations. Data are taken from mixed WT populations with an old technology and a power lower than the modern turbines. ReliaWind project attempted to address the limitations of the first databases by considering around 350 operating turbines that met the following requirements: onshore WF with at least 15 turbines, rating greater than or equal to 850 kW, variable speed, pitch regulated and operating for a minimum of two years [79]. Figure 29 and Figure 30 show the percentage distribution of failure and downtime with wind turbine sub-assemblies from ReliaWind project, from approximately 35000 downtime events.

The Power Mode and Rotor Modules are the subassemblys component of the machine responsible for the most failures and machine shutdowns.

The failure trend obtained through the ReliaWind project are comparable with the WMEP, LWK and the Swedish results while a different downtime trend have been obtained. In particular, ReliaWind downtime trend shows much greater emphasis on the rotor and power modules because it is believed these newer WTs have not yet experienced major gearbox, generator or blade failures to date in service [80]. Therefore, downtime trend obtained through the ReliaWind project could not be representative of the real problem and so it is still necessary take in reference the results obtained through previous projects.
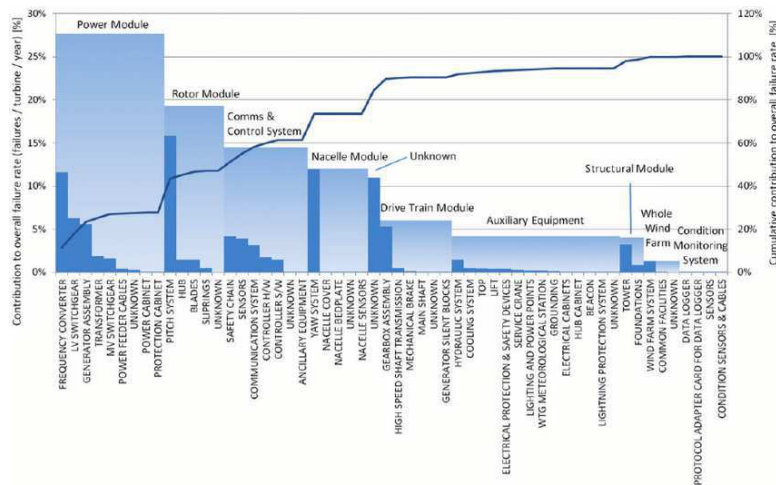
Figure 29 Distribution of normalised failure rate by sub-system and subassembly for WTs of multiple manufactures from the ReliaWind survey [79]
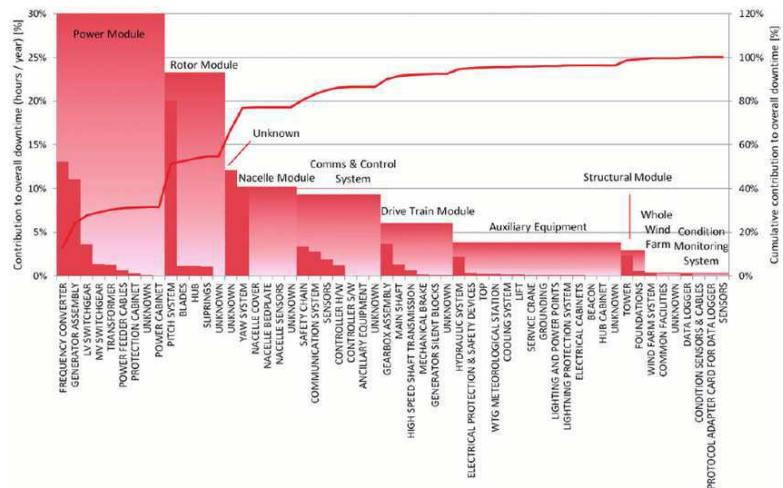
Figure 30 Distribution of normalised downtime by sub-system and subassembly for WTs of multiple manufactures from the ReliaWind survey [79]

Figure 31 reports the downtime trends from WMEP, LWK & Scandinavian projects; it shows that gearbox and blade failures are the main drivers of the most hours of machine shutdown [81]. This is not due to their intrinsic design weakness but rather the complexity of changing them in the field, entailing the use of cranes and the need for prior planning [80]. Furthermore, in [82] has been shown that 75% onshore WT failures are responsible for only 5% of the downtime while 25% of failures cause 95% of the downtime. This is because the 75% of failures are often associated with electrical faults (converter, electric pitch system, control equipment switch, …), which are often relatively easy to fix via remote or local resets in onshore environment. These figures are likely to be dramatically changed as WTs go offshore, indeed the 75% of failures will not repair quickly due to limited accessibility and difficult of travel and access to the farm.
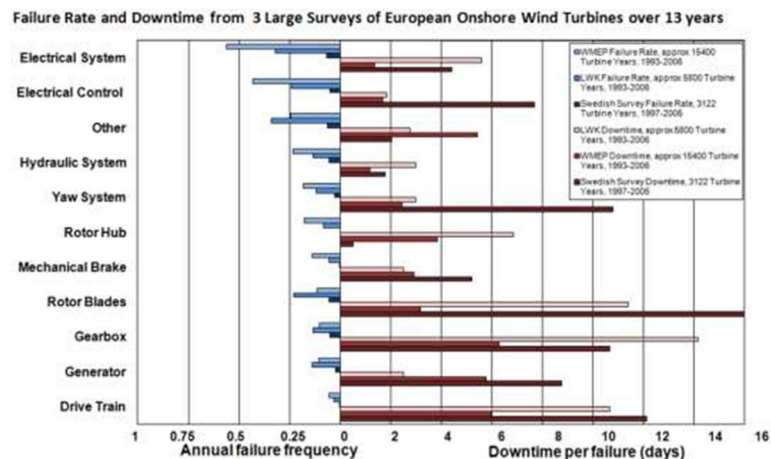
Figure 31 WT failure rate & downtime per failure from results for onshore WTs from 3 surveys (WMEP, LWK &Scandinavian) including >24000 turbine-years of operation [81]

MONITORING OF WIND TURBINES

As described above, the four major WT reliability projects are related to onshore installations and not many publications have been made for offshore installations. In [83] has been presented a reliability analysis of 3 years of available data from Egmond aan Zee offshore WF in the Netherlands (NoordzeeWind, 2007-2009). Figure 32 shows the annual stops frequency and downtime per stop in days for 13 subassemblies for offshore wind turbines. Even if stops and failures are different concepts, the overall distribution of Figure 31 and Figure 32 are more similar, i.e. the subassemblies with high stop and failure rates not always being the worst causes of downtime. In particular, the gearbox and generator contributed only 6.7% and 2.8% respectively of total stops but 55% and 15% respectively of the downtime. While, the control system dominates the number of stops, 36%, but caused only 9.5% of the total downtime.
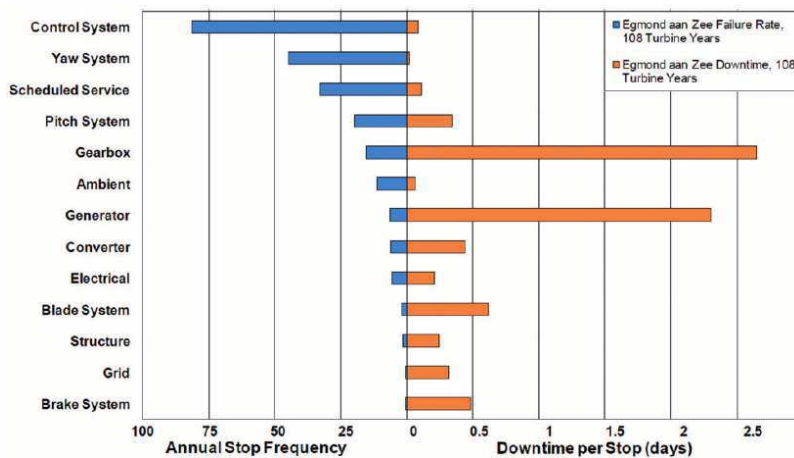
Figure 32 Stop rate and downtime data from Egmond aan Zee WF over 3 years [83].

The reliability of WT, besides depend on the reliability of its subassemblies, depends by several parameters, such as WT size and atmospheric conditions.

The dependence of WT reliability on its size is investigated in [84]. The work utilized failure rates data over 11 years from 12 onshore WT models from the LWK survey. The results of this analysis, summarized in Figure 33, show that the failure rate increase when WT size increase. Based on this result, it seems that it may be difficult to decrease initial failure rate as turbines continue to grow in capacity, although reliability improvements are always being introduced.
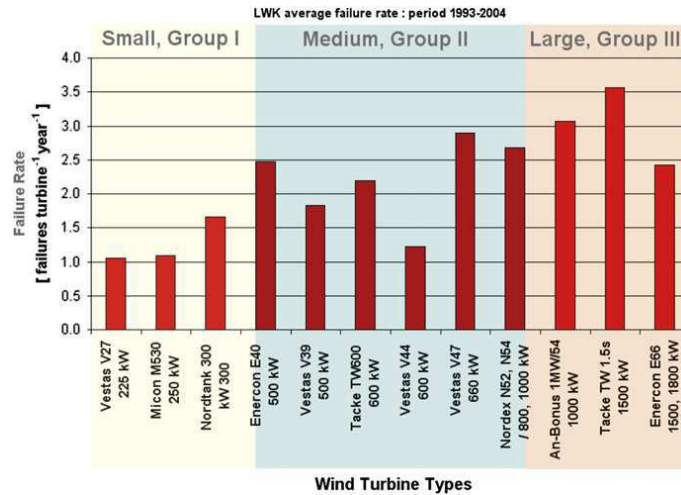
Figure 33 Distribution of failure rates between different WT models [84]

Finally, environmental condition has a strong impact on WT performance in term of damage. In particular, the reliability of WTs depend on wind speed[85][86]. In [86] has been carried out a physical check on the variation of the failure rate with Wind Energy Index (WEI) based on analysis of Danish WT field data from Windstats. Where WEI is defined as:

$$WEI = \frac{\text{Actual monthly energy production from a collection of wind turbines}}{\substack{\text{Long term expected monthly energy production from} \\ \text{those turbines in the presence of average weather}}} \qquad (7)$$

The results of this analysis, given in Figure 34, show that the failure rate is height when WIE is height and vice versa, so it proves a dependency between the failure rate and the WEI.
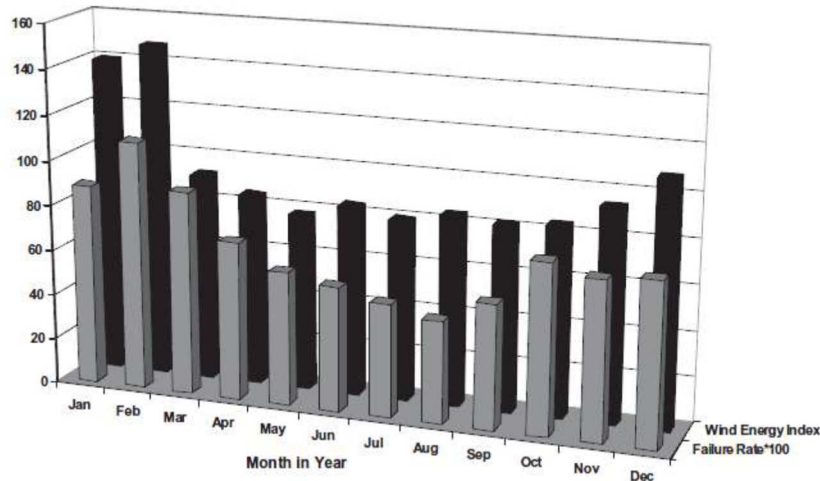
Figure 34 Correlation between failure rate & WEI [86]

In conclusion, at the state of the art the number of WT failures is typically 1-3 failures per turbine per year [87]. This failure rate is acceptable for onshore WTs, while it becomes unacceptable for offshore WTs due to the complexity of access to the site. For offshore WTs, a failure rate of 0.5 would be desirable.

The improvements on offshore reliability must be pursue through design and operational measures. They should prevent failure, mitigate the damage, reduce repair & maintenance costs and avoid unplanned maintenance. Finally, a standardized methodology is needed for reliability data collection and analysis; this can be achieved through close collaboration between manufacturers, operators and research institutes [88].

3.3   Wind Turbine Monitoring Structure

Monitoring is a systematic or continuous process of observing, measuring and recording activities of a machine. The output information from a monitoring system are compared with assigned thresholds or statistical values for a diagnosis of the operating status of the machine.

According to [89], the operational reasons for monitoring wind turbines are:

- To obtain commercially important information such as confirmation that the turbine is operating and the amount of energy being generated;
- To confirm the health of the overall WT structure and its safety;
- To detect subassembly faults or failures through alarms systems;
- To find the exact nature and location of any fault or failure and schedule maintenance.

Each of the 4 operational reasons listed above may be associated to a monitoring structure class: Supervisory Control and Data Acquisition (SCADA), Structural Health Monitoring (SHM), Condition Monitoring (CM) and Diagnosis. The four classes are shown in Figure 35 [89] and they are described in detail in the following sections. In the modern WT, the data coming from the four classes are merged among for enhanced fault-detection performance [77].
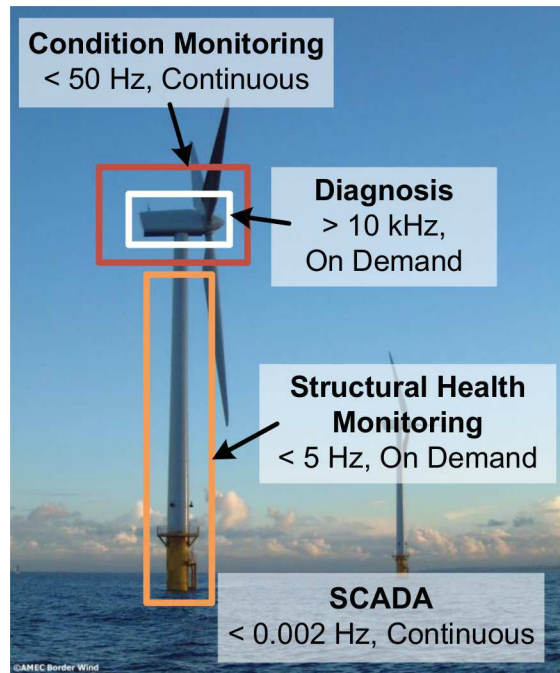
Figure 35 Structural health and condition monitoring of a wind turbine [89]

3.3.1 Supervisory Control and Data Acquisition (SCADA)

SCADA is a data-collection system to provide real-time and historical information to supervise and control of the entire wind park and the individual wind turbines. These data, containing informations about the state of the WT and its subassemblies, are often recorded using high sample frequency and then a statistical analysis at 10 minutes intervals is performed. Typically, the minimum data set includes wind speed, wind direction, active power, reactive power, ambient temperature, pitch angle and rotational speed, according to [77]. However, the modern SCADA often recordes much more signals, as for example gearbox lubrication oil temperature, temperature values, electrical quantities etc. For all recorded signals the SCADA system transmits maximum, mean, minimum and standard deviation values.

The availability of high-frequency acquisitions data from SCADA system have driven the operators to use these data to perform condition monitoring. Several studies have been carried out in recent years and, according to [77] and [90], the condition monitoring techniques based on SCADA systems can be grouped into three categories: Signal Trending, Artificial Neural Networks (ANN) and Physical Models.

In [90] is reported an analysis of performance and limitation of the Physical-Model approach. The analysis compares the detect failures on historical data with the real failures of wind turbines allowing to understand how many and how long before

MONITORING OF WIND TURBINES

failure the method can detect a fault. In total, the method detected correctly 24 out of the 36 real failures with three false alarms (i.e. the method detected a failure without a real damage on the WT). The majority of these faults have been detected within six months before the failure. In particular, Figure 36 shows the range and distribution of the advance detection period for the four main failures (i.e. main bearing, gearbox, generator bearings and generator windings).
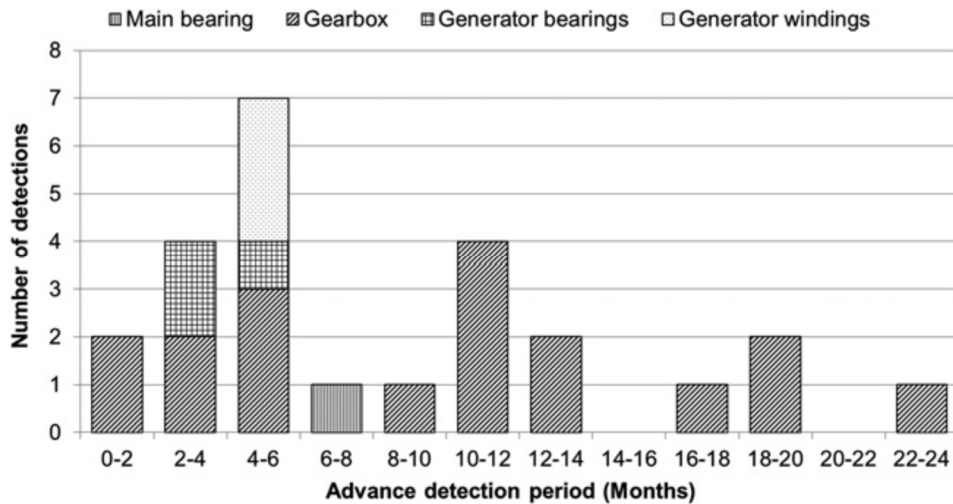
Figure 36 Distribution of advance-detection periods for faults detected based on SCADA data (Physical-Model approach) in the validation study [90]

The results from Physical-Model approach did not demonstrate a good performance of SCADA system to detect faults and then, at present stage, it cannot replace CM system, this is in line with [77][91][92]. However, studies are underway to develop condition monitoring techniques from SCADA systems, since it would significantly reduce the costs of monitoring a wind turbine.

3.3.2 Structural Health Monitoring (SHM) and Condition Monitoring (CM)

Wind turbine is exposed to harsh environmental conditions and fluctuating mechanical and aerodynamic loads. The operating conditions of the wind turbine are the source of the reduction of wind turbine reliability and can give rise to system fault or failure, in particular of the turbine's drivetrain and actuators. According to [93], gearboxes are commonly faced with abrasive wear, micropitting, scuffing, and macropitting issues; while, the nacelle yaw and blade pitch mechanisms commonly suffer from false brinelling and fretting damage.

Fault is defined as a significant change of the system parameters beyond acceptable/allowed limits reflected in a negative impact on overall system performance [94]. Therefore, the impact of a fault can be tolerable. Contrary,

system failure is a complete loss of the functionality whereas the system is not capable to perform predefined functionalities [95]. Usually in Wind Energy Conversion Systems (WECSs), a fault is indicative of a developing failure [101]; therfore a condition monitoring is required to identify faults before catastrophic damage occurs with a reducing of O&M costs [97] and the risk of premature breakdowns [96].

The monitoring system of a wind turbine can be classified into two categories: Structural Health Monitoring (SHM) and Condition Monitoring (CM). A SHM system detects the integrity of WT structural components as the support structure (tower, structure and foundation) or rotor blades, while systems for monitoring other components, as for example drive train, are usually called Condition Monitoring (CM) [77]. For the simplicity, both monitoring systems will be named CM from this point onward.

As shown in Figure 37, CM is performed in three main steps: data acquisition using sensors, signal processing using various data processing techniques and feature extraction via the retrieval of parameters that will aid in establishing the current status of the monitored equipment [69]. Several techniques and sensors have been developed over the years for all four main components of the wind turbine (i.e. foundations, tower, gearbox and blades). Standard ISO 61400-25-6 [105] provides a description of sensors type, sensors position and sensor orientation that can be used for the condition monitoring of WT. However, the wind energy industry requires condition monitoring techniques with high reliability, which corresponds to a low risk of false alarms or missed faults. At the state of the art, there are no solutions able to reach these targets [128]. Therefore, data fusion is often recommended [129]; it combines information from multiple sensors (and possibly from different monitoring techniques), compensating the wrong analysis on a single one techniques and increasing the reliability of the overall CM system.

3.3.3 Diagnosis, Prognosis and Maintenance

When a change of the system parameters occur, CM sent an alarm signal to the SCADA [99], which is the trigger for further and more detailed investigation. In particular, using the same sensors used in CM systems but with higher sample-frequency, faults can be detected (diagnosis) or predicted (prognostic) and the appropriate maintenance strategy have to be chosen [69] to deploy the minimum resources required, ensure system reliability and recover from breakdowns [102].
In particular, if a fault is detected suitable corrective maintenance actions have to be applied. The two main approaches are: palliative maintenance, which is a provisional solution to failures, and curative maintenance for standing solution to failures [69]. While, if a fault is predicted, preventive maintenance is carried out

before the fault occurs. In this case, four different approaches can be used: time-based or scheduled maintenance, current-state based or conditional maintenance, parameter-projection-based or forecasting maintenance, status-based or proactive maintenance [69]. However, these four maintenances actions require an estimation of the State-of-Health and a prediction of the remaining lifetime of the system. Where, the main remaining lifetime prediction strategies adopted in the wind turbine are condition-based [98], which compares the current system state (measured through CM system) with the designed conditions, and reliability-based [100], that instead combine the system state in two successive instances.

The framework of the interaction between condition monitoring, diagnosis, prognosis and maintenance systems described above is shown schematically in Figure 37.
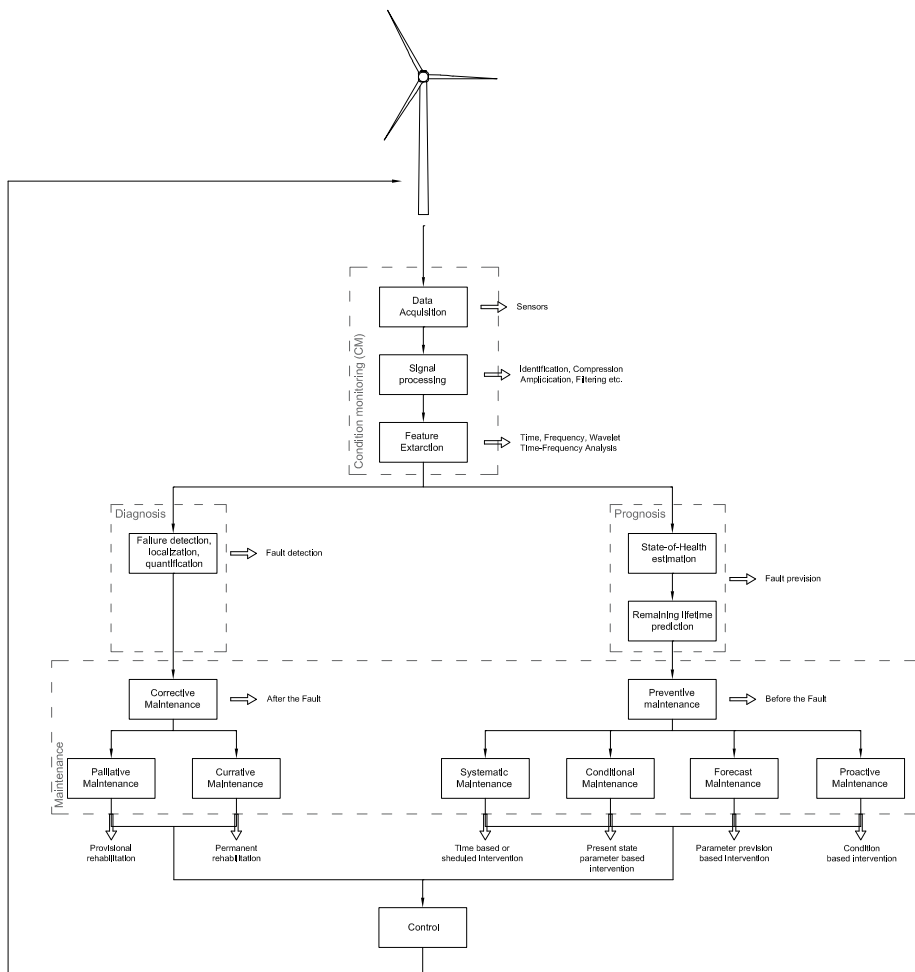
Figure 37 Framework of the interaction between condition monitoring, diagnosis, prognosis and maintenance systems, according to [94] and [69].

3.4 State of the art of drivetrain CMS for wind turbines

As already described in the introductory chapter, one of the focus of this research is to develop a new drivetrain condition monitoring technique. CMSs for the drivetrain have been the main focus for the wind industry [77]. This is because the drivetrain failure causes the highest annual downtime among all turbine components, due to the high failure rate combined with a time-consuming, highly expensive and difficult replacement procedure [130].

CMS can be certified by Germannischer Lloyd [103]; for drivetrain, the certification is mainly based on vibration-based CMS and considers Oil-based CMS as a suitable addition for vibration-based CMS but not as a standalone solution. A detailed description of CMS for drive train is provided in the following sections, they will describe the required instrumentation, the diagnostic method applied and the advantage of each solution. In particular, sections 3.4.1 and 3.4.2 introduce the vibration-based and oil-based drive train CMS, respectively, while in section 3.4.3 further techniques are discussed.

3.4.1 Vibration-based CMS

Vibration measurement is a low-cost and one of the typical CMSs applicable to monitoring rotating parts of WT, i.e. drive train. This CMS make use of the fact that most damages in rotating machine change the vibration characteristics of the structure, like stiffness and damping [106][107].
The standard ISO 13373-1 [104] provides an overview of the vibration transducer with their dynamic features. The sensors usually applied for vibration-based CMS include laser vibrometers, velocity sensors, accelerometers, spectral emitted energy sensors and displacement sensors. The issues that should be taken into account in evaluating the most appropriate solution are frequency range, dynamic range and the sensitivity of the sensor [77]. According to GL Certification Guideline [103], Table 11 reports an overview of sensor types, sensor number, position and orientation, although a specific position cannot be recommended due to the large variety of wind turbine design.

Concerning vibration-based drive trains CMS, damage detection algorithms make use of the fact that a structural change is reflected in a change of natural frequency and/or mode shape and, according to [106], the algorithms can be classified in four categories:

1. mode shape-based techniques;
2. curvature shape-based techniques;
3. frequency-based techniques;
4. combined shape-based and frequency-based techniques.

These four algorithms extract information from vibration signals with time domain analysis methods and/or frequency domain analysis methods. Where the main time-domain analysis are *Statistical and parameter-based methods*, *Trend analysis*, *Time synchronous averaging*, *Planet separation method* and *Amplitude demodulation*. While the main frequency-domain analysis are *Fast-Fourier Transform and spectrum analysis*, *Order analysis*, *Cepstrum analysis*, *Envelope curve analysis*, *Spectral kurtosis filtering* and *Wavelet analysis*. A more detailed description about each method and its implementation can be found in [77].

Component of the wind turbine	Necessary number of sensors per component	Direction of measurement	Frequency range
Rotor bearing	1 (+1 optional)	Radial + Axial	0.1Hz… ≥10kHz
Gearbox	4+1	Radial + Axial	0.1Hz… ≥10kHz at low speed shaft 10Hz… ≥10kHz at high speed shaft
Generator bearing	2	Radial	10Hz… ≥10kHz
Tower with nacelle	(2 optional)	Axial in wind direction and transversal to the axial direction	0.1Hz… ≥100Hz
Rotor blade	(2 optional)	In rotor axis direction and transversal to the rotor axis	0.1Hz… ≥10kHz

Table 11 Minimum sensor requirements for vibration-based CM according to the GL Certification Guideline 2013 [103] [77]

3.4.2   Oil-based CMS

One of the most promising techniques for monitoring WT drivetrain is oil analysis [108]. Oil analysis can be applied online and offline on hydraulic and/or lubrication oils to determine the chemical properties and content of oil, coolant or lubricant. The purposes of oil-based CMS are:

1) monitoring the properties of the oil in order to safeguarding the quality of the lubrication, the effectiveness of the filter system and to determine the necessity of an oil change;

2) safeguard the components involved. Indeed, wear debris content can indicate developing faults.

Although online oil analysis entails time consuming and relatively expensive technique, such as spectrometers, analyser or Scanning Electron Microscopes, is considered one of the most promising condition monitoring techniques for WT. The market offers a large number of sensors for Oil-based CMS [109]. According to [77], Table 12 gives an overview of commercially available sensors.

Type of sensor	Output signal	Status of implementation in wind turbines
Water-content sensors	Water saturation (%)	Only laboratory tests, validation for wind turbines required
Particles-concentration sensors	Particles size distribution according to ISO 4406	Laboratory tests and experimental test in a wind turbine
Wear-debris sensors	Quantity of particles per unit of time and size	Part of standard CMS of some wind turbine manufactures
Dielectric constant sensors	Dielectric constant	Laboratory tests for several industry applications
Viscosity sensors	Kinematic viscosity	Laboratory tests for wind turbine applications
Oil-properties sensors	Viscosity, temperature, density, dielectric constant	Experimental test in some wind turbines
Oil-quality sensors	Color code, quality index	Laboratory tests for wind turbine applications

Table 12 Overview of commercially available sensors for oil condition monitoring, according to [77]

3.4.3 Further techniques for drive train condition monitoring

As discussed previously, the most common CM techniques for drive train are based on vibration and oil analysis. The limitations of the two main techniques have drove research institute to develop new CM systems. In the following sections is presented a brief description for the main alternative CM systems, in particular acoustic emission, thermography and measurement of electrical or mechanical parameters.

3.4.3.a   Acoustic emission

Acoustic emission has some similarities with vibration monitoring and then acoustic sensors have some similarities with vibration sensors but with a significant difference. While vibration sensors are able to detect movement of the structure, acoustic sensors are able to measure the waves generated sudden release of energy due to strain or damage within or on the surface of a solid material, or by the interaction of two media in relative motion [110]. The detection of faults and their localization requires a high number of distributed sensors [111], usually piezoelectric-sensors, with a frequency range between 20 kHz and 10 MHz [112] [113].

To detect faults, acoustic emission signals are usually characterized in terms of amplitude and energy [96]. In [115] is shown the success to fault detection by a statistical analysis of acoustic emission signal. However, it is still necessary to develop a capture method to monitor faults progression [113].

Although this technique is very costly due to the cost of the acquisition system, a lot of applications have been born in recent years for bearing and gearbox monitoring to detect faults such as pitting, cracking or deboning in the initiation phase [115][113][112]. The advantages of this technique in comparison with vibration-based CM are:

- greater flexibility and low attention in sensor placement;
- wider bandwidth of frequency is considered which can give an indication of starting defects;
- more robust for low-speed operation of WT.

This section has discussed the application of acustic emission technology for drive train monitoring, however it is fair to point out that the tecnique shows also a excellent behaviour for rotor blades monitoring [114].

3.4.3.b   Thermography

Thermography is a technique in which an infrared camera is used for detecting and measuring temperature variations on the surface of a structure or body part and transforming them into visible signals (images). Energy transferred to the material induces specific temperature distribution around damaged areas allowing damaged area detection in early stage and stress analysis [94]. Although the fault detection is more easy for external damage, thermography shows also a good behaviour for internal damage. As for example the detection of delamination, debonding, matrix cracking, and fiber pulling out, that are probable internal damage for wind turbine blades [116].

Concerning drivetrain, this method has already been implemented to monitoring thermal power plants [117] [118]. In [117] [77] the thermography application on wind turbines is suggested, in particular for monitoring:

- Electrical system (power electronics, control system);
- Transformer;
- Nacelle (fire detection);

Like acoustic emission CMS, thermography can be considered a complementary method of vibration-based CMS and oil-based CMS, but cannot replace them, either for on-line CMS and off-line CMS.

Cameras and diagnostic software are starting to become available, however at the present the technique is not particularly well-established for on-line process monitoring due two main limitations:

1. high cost of IR cameras [119];
2. thermography monitoring is usually performed manually and should be done when the equipment is fully loaded, this entails risks and then saftey issues.

This section has discussed the application of thermography technology for drive train monitoring, however it is fair to point out that also it shows excellent behaviour for rotor blades monitoring [116], in particular for fatigue testing [120][114].

3.4.3.c   Electrical parameters

All of the CM techniques described above require their own data acquisition system and analysis software [96]. In contrast, the electrical current and voltage are continuously measured and an additional acquisition system is not necessary. Therefore, the advantages of CMS based on electrical parameters are the low cost [121] and its non-intrusive nature.

Monitoring based on electrical parameters have been used to detect gearbox tooth damages, generator and bearing problems. Two techniques are applied to identify this faults; Motor Current Signature Analysis (MCSA) and frequency analysis. MCSA allows to detect generator problems [77], as for example stator phase inductive unbalance, rotor phase resistive unbalance, phase resistive unbalance and turn-to-turn faults, and gearbox tooth damage [122][123][124][125][126]. While, bearing faults are usually identified by using current frequency and amplitude demodulation algorithms of one-phase stator current. Indeed, a bearing fault induces shaft torque variation in the generator with a modulation of amplitude and frequency of the current signal [77]. However, the extraction of bearings fault is not easy because their frequencies are fluctuating [127]; the two main solutions that

can be applied to overcame this problem are phase-locked loop and wavelet analysis.

3.4.3.d   Shaft torque signal

Torque is a fundamental operating parameter of rotating mechanical systems. In case of wind turbines, the study of drive train torque allows to optimize WT control in order to increase the power, with a direct impact on annual energy production [131], and to carry out CM on drive train.

During the last decade, wind turbine CMS based on shaft torque signal has recorded a great interest [132][96] [127][133] because shaft torque contains information on the mechanical response to wind before any generator effects. This condition monitoring technique allows to detect rotor electrical asymmetry and machine winding faults [134][135][136] but it is particularly efficient to detect gearbox failures [133] and rotor imbalance [130][137]. For gearbox faults usually vibration analysis algorithms are used. However, at present these algorithms cannot predict if and when the faults will occur in the gearbox and neither when the total failure is expected if the fault is already detected [130]. To overcame this limits, the new algorithms measure shaft torque and analyse the fatigue loads of the gearbox. While for rotor imbalance, usually power spectra density analysis are used [130]; where the effects of rotor imbalance on the WT can be subdivided into two groups: blade mass imbalance and aerodynamic asymmetry.

Despite the great potential to use shaft torque signals for wind turbine condition monitoring, their application is still limited to the laboratory environment. The main obstacle to industrial application is the costly, intrusive nature and unacceptable accuracy of the required measurement equipment. Following is reported a list of the main torque transducers, available for wind turbine shafts application, with the advantages and disadvantages of each solution:

1. Flange torque transducer. Flange torque transducer is designed to mount in-line between a driving source and an absorber or load. The core of the torque transducer is instrumented with a strain gage torsional bridge. When the shaft is turned a torsional stress occurs, which causes a proportional resistance change in the strain gages, resulting in a voltage shift in the sensor's output signal. This transducer has usually a higher accuracy (superior temperature stability and minimal linearity deviation and hysteresis) than other solutions. This results are achieved thanks the possibility to perform a calibration procedure in laboratory; even if, in case of torque transducer with a capacity larger than 1.1 MN the traceability of a calibration is not guaranteed [138]. The main disadvantages of this solution are the high cost and its intrusiveness. Indeed, the transducer

cannot be applied to an existing machine but requires a redesign of the shaft;

2. Strain gage sensors. Shaft torque can be measured by a full bridge with pairs of gages at the opposite sides of the shaft; gages measure at 45° from shaft axis, as required for torque. Strain gage can be directly glue on the shaft surface without to need a shaft redesign; a cylindrical section should be chosen, far enough from other components in order to avoid local stress concentration. The main disadvantages of this solution are: difficult to install it (the gluing should be done by a highly skilled staff); require a telemetry system for signal transmission; the uncertainty is large, typically around 5%; strain gage sensors suffer from crosstalk and may be influenced by local strain distributions, which cannot be compensated, not even through calibration; a calibration procedure have to be performed on field; strain gage solution is impractical for long-term use on operating WTs, due to limited life of strain gages;

3. SAW torque transducer. SAW sensors act as 'frequency dependent' strain gauges. Like strain gage solution, shaft torque can be measured by a full bridge with pairs of SAWs glued at 45° from shaft axis and at the opposite sides of the shaft. A solution of a batteryless non-contact SAW torque sensor suitable for aftermarket installation on wind turbine drivetrains has been presented in [139]. The advantages of this transducer are: the gluing is more easy than strain gage but should be still done by a highly skilled staff; SAW calibration can be performed on a test bench in laboratory. While, the disadvantage of this solution, that hinder its massive implementation, is the short reading range. This foremost limitation of the SAW based sensor system occurs when the reply signal strength at the reader becomes too weak for reliable recognition and identification [140];

To overcome the limits of the previous described solutions, a novel non-intrusive and simple contactless torque and speed measurement system have been developed during the PhD [141]. The technique consists of two zebra tape codes directly glued around the shaft with two optical sensors mounted on non-rotating supports. As the shaft rotates, each optical sensor, mounted on a non-rotating component, generates a pulse train signal proportional to the light intensity reflected by the zebra tape stripes. When a torque is applied to the shaft, the relative rotation of the ends of the shaft section results in a time shift, between the two pulse train signals. The principle of the proposed method is to quantify the shaft relative twist angle, by measuring the phase difference between the two pulse signals, and thence deriving the applied torque, from a known torque-twist relationship.

This technique operates entirely contact-free and allows torque measurement on standard installations, across their operational life, avoiding the use of permanently installed in-line intrusive torque meters, by simply instrumenting the existing shaft with the two zebra tapes located as far as possible from each other. The use of optical sensors and zebra tapes on rotating shafts is not new; however literature reports only application for torsional vibration measurement [142][143], while this thesis proposes their use for torque measurement. Chapter 6 gives a more detailed explanation of the technique.

The advantages of this technique are: the low cost; non-intrusiveness; the possibility to measure simultaneously torque and speed; the possibility to measure torsional vibration [142][143]; the possibility to install it on an existing machine without having to redesign the shaft; a good accuracy. The disadvantage of this solution, that hinder the implementation on all turbines, is the linear dependence between angular shift and distance between the zebra tapes. This limitation prevents the application of the technique in WT with short shaft.

4 MEASUREMENT OF MECHANICAL LOADS IN LARGE WIND TURBINES: PROCEDURES TO SELECT THE MEASUREMENT CHAIN AND TO CALIBRATE THE STRAIN GAGE SENSORS

The standard IEC 61400-13 defines the guidelines to be followed for measuring mechanical loads, including sensor selection, application practices, calibration procedures, uncertainty analysis and thermal compensation. The strain gauges applied to the structure are selected as the recommended type of sensor. However, given the continuing increase of dimensions of wind turbines, the difficulty to perform a correct load sensor calibration, so to meet the certification requirements, remains a complex task and a problem which deserves attention, as has been addressed in recent literature [146][147].

This chapter describes the procedures that have to be followed in the design of a measurement chain and calibration of typical strain gage bridges installed on wind turbine with a rated power output greater than 1500 kW and a rotor diameter greater than 75 m, as I have described in [156].

Calibration is the process through which it is possible to establish a physical relationship between the electrical signal output from the sensor and the mechanical load input acting on the structure. According to IEC 61400:13, commonly used methods are Analytical calibration, Gravity loads and External load. In particular, this chapter, in paragraph 4.4.3, focuses mainly on calibration by using Gravity loads and it suggests the models for load sensor calibration of bending bridges through unbalanced masses of the turbine. The loads generated through these unbalances, for some turbine sections, will only cover part of the measurement range; in particular, for bottom tower bending moments, the fraction of the full scale may be really small, lower than 5%, because unbalanced masses are able to cause only small bending moments relative to those generated by aerodynamic actions during operation. In these cases, a combination of Analytical and Gravity loads calibration methods is required.

4.1 Mechanical loads quantities to be measured

Mechanical load magnitudes must be recorded for each MLCs during the certification process. The standard defines mandatory and recommended quantities, but this list is not restrictive; indeed, the accredited certification institutes can add some, if it finds appropriate during the certificate process.

Load quantities have to be selected in accordance with the turbine in analysis. In particular, the parameters given in Table 13 are referred to wind turbines with a

rated power output greater than 1500 kW and a rotor diameter greater than 75 m; which represents the case under analysis in this thesis.

Load quantities [50]	Level of importance [50]	Sampling Frequency (not prescribed by IEC) [51]
Blade flatwise bending moment distribution	2 blades mandatory, 1 blade recommended	≥ 64 samples/s
Blade edgewise bending moment distribution	2 blades mandatory, 1 blade recommended	≥ 64 samples/s
Blade root flatwise bending moment (Mbf)	2 blades mandatory, 1 blade recommended	≥ 64 samples/s
Blade root edgewise bending moment (Mbe)	2 blades mandatory, 1 blade recommended	≥ 64 samples/s
Blade torsional frequency and damping	Recommended	≥ 64 samples/s
Pitch actuation loads	One blade mandatory	≥ 64 samples/s
Rotor tilt moment (Mtilt)	Mandatory	≥ 64 samples/s
Rotor yaw moment (Myaw)	Mandatory	≥ 64 samples/s
Rotor torque (Mx)	Mandatory	≥ 64 samples/s
Tower base normal moment (Mtn)	Mandatory	≥ 64 samples/s
Tower base lateral moment (Mtl)	Mandatory	≥ 64 samples/s
Tower mid normal moment (Mtmn)	Recommended	≥ 64 samples/s
Tower mid lateral moment (Mtml)	Recommended	≥ 64 samples/s
Tower top normal moment (Mttm)	Mandatory	≥ 64 samples/s
Tower top lateral moment (Mttl)	Mandatory	≥ 64 samples/s
Tower torque (Mttt)	Mandatory	≥ 64 samples/s

Table 13 Wind turbine load quantities for turbines with a rated power output greater than 1500 kW and rotor diameter greater than 75 m, according to IEC 61400 – 13 Edition 2015 [50].

For each of these quantities, it is necessary to design a measurement chain and perform a calibration process; but, in this chapter, this analysis will be restricted only to mechanical moments that are highlighted in grey in Table 13.

Concerning *Rotor tilt* and *Rotor yaw, they* are the bending moments M_{y_n} and M_{z_n} in the non-rotating co-ordinate system of the rotor, respectively, according to Figure *38*. These moments cannot be measured but have to be computed from the *Shaft parallel* and *Shaft normal* bending moments, according to equations (8) and

MEASUREMENT OF MECHANICAL LOADS IN LARGE WIND TURBINES

(9), if strain gauges can be applied to the shaft. Where, *Shaft parallel* and *Shaft normal* are the measured bending moments M_{y_h} and M_{z_h} in the rotating co-ordinate system of the hub, respectively, according to Figure *39*.

$$Rotor\ tilt = Shaft\ parallel * \cos(\theta) - Shaft\ normal * \sin(\theta) \qquad (8)$$

$$Rotor\ yaw = Shaft\ parallel * \sin(\theta) + Shaft\ normal * \cos(\theta) \qquad (9)$$

Where θ is rotor azimuth and $\theta = 0$ when the blade is vertical and pointing up, according to the standard IEC 61400:13 [50].
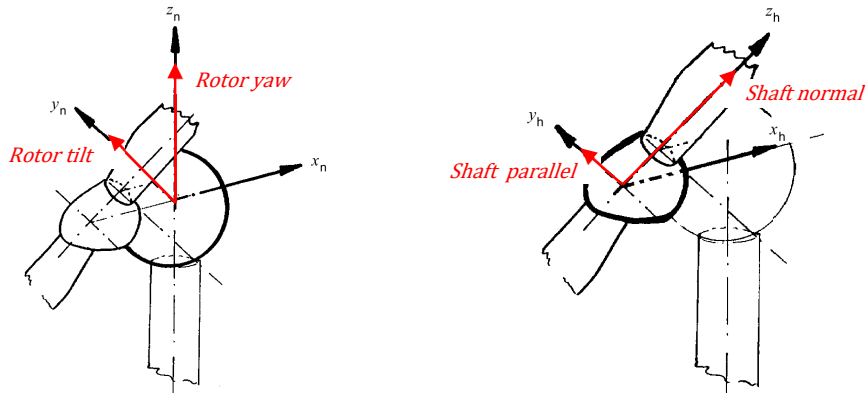
Figure 38 Nacelle co-ordinate system [50]   Figure 39 Hub co-ordinate system [50]

Therefore, the analysis that will be described below will be limited to the problems of measuring *Shaft parallel* and *Shaft normal* bending moment, while no analysis will be performed for *Rotor yaw* and *Rotor tilt* moment.

4.2 Selection of load sensor, electrical connection and measurement section

For each of the load quantities to be measured, it is necessary to define the load sensor, the electrical configuration and the measurement section. Topics discussed below.

A load sensor is a device that directly or indirectly measures the load of a system or component. Typical devices include, but are not limited to:

– strain gauge bridges;

– load cells/torque tubes (including piezoelectric cells);

– accelerometers, velocity, rotation and displacement transducers.

For wind turbines, it will seldom be possible to place a load cell in a main load path. For this reason, strain gauges applied to the structure are selected as the recommended type of sensor by the standard [37] and therefore this thesis will mainly discuss topics related to their use.

A specific strain gage full bridge has to be realized in the appropriate section of the machine and with the proper geometric configuration; in all cases full bridges are suggested because of their linearity, high sensitivity and because they compensate undesired inputs, such as axial loads, orthogonal moments and thermal effects. However, the compensation of undesired inputs occurs only in case of a perfect installation, perfect structural symmetryand only if the parameters of all the 4 strain gages are exactly the same.

In order to measure bending moments acting on the turbine, two typical bridge configurations are used: parallel strain gages (Figure 40-a) or T configuration (Figure 40-b). The parallel solution provides a bridge factor equal to 4, which allows to maximize sensitivity to the desired input moment, and it cancels out all effects due to axial forces, torsion and orthogonal bending moments, but requires the two sides of the bridge to be isothermal. The T configuration has a bridge factor equal to 1.6 and compensates thermal differences between the two sides of the bridge, provided the material is isotropic. Typically, on steel parts, such as the tower, it is preferred to use a T configuration [145][147][148], because it is superior in thermal compensation, even if its bridge factor is lower than the parallel configuration. While, for composite material blades, a parallel configuration could be preferred [150], because of the anisotropic behaviour of the material. At the next chapter, the thesis will discuss the thermal effects on strain gage bridges in real field installation of a large wind turbine.

a) *parallel bridge configuration and circuit*   b) T bridge configuration and circuit
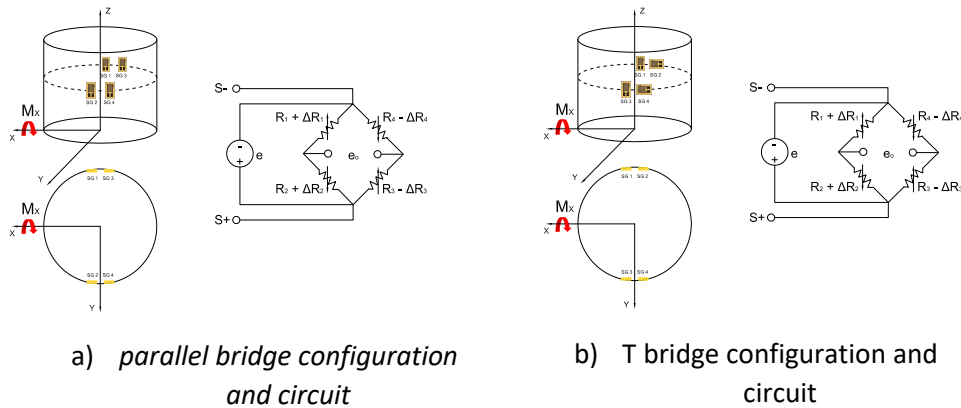
$$e_0 = \frac{e*k}{4}(\varepsilon_1 + \varepsilon_3 - \varepsilon_2 - \varepsilon_4)$$ where: K = gauge factor; ε_i = strain measured by i^{th} strain gage.

Figure 40 Typical full bridges used in wind turbine type testing for bending moments [145]

While, in order to measure torsional moments, the configuration shows in Figure 41 is usually applied. This configuration has a bridge factor equal to 4 and compensates thermal differences between the two sides of the bridge, provided the material is isotropic.

$$e_0 = \frac{e * k}{4} (\varepsilon_1 + \varepsilon_3 - \varepsilon_2 - \varepsilon_4)$$

where:

K = gauge factor;

ε_i = strain measured by i^{th} strain gage.
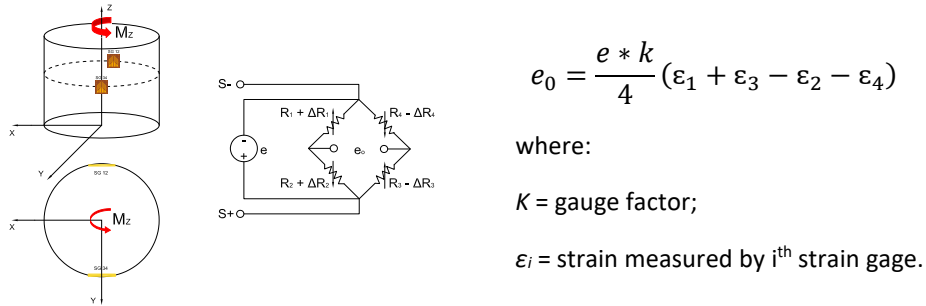
Figure 41 Typical full bridge used in wind turbine type testing for torsional moments

According to Italian standard UNI 10478-4 [153], the electrical connection of a full strain gage bridges, in the case of long cable connections, can be made using 4-wire or 8-wire, as shown in Figure 42.

Type of conncetion	Electrical circuit	Note
eight-wire		Not recommended
Four-wire		

Figure 42 Eight-wire and four-wire connection of full-bridge circuit

In particular, the standard recommends to use a four-wire connection (closed on the structure) compared to the eight-wire connection (closed on the instrument). In the first case, the resistance of cables is external to the bridge and then the thermal response due to the cables is eliminated; while in the second case thermal effects are compensated only if the cables are the same for the eight arms of the bridge, have the same length and are exposed to the same temperature variations. However, when using a four-wire connection, the lead resistances are drawn in the supply leads. These cause a partial voltage dropping off in the cable, as a result, the output signal is smaller and the measurement system is less sensitive. To overcome this problem, two additional leads to control the excitation voltage at the bridge are required; then, 6-wire bridge is preferable, according to Figure 43 [154]. If the cable resistance varies as a result of the influence of temperature or change in cable length, the amplifier makes internal readjustments until the set point value is again reached. This allows to use very long cables (up to 500 m) without affecting the sensors' sensitivity.
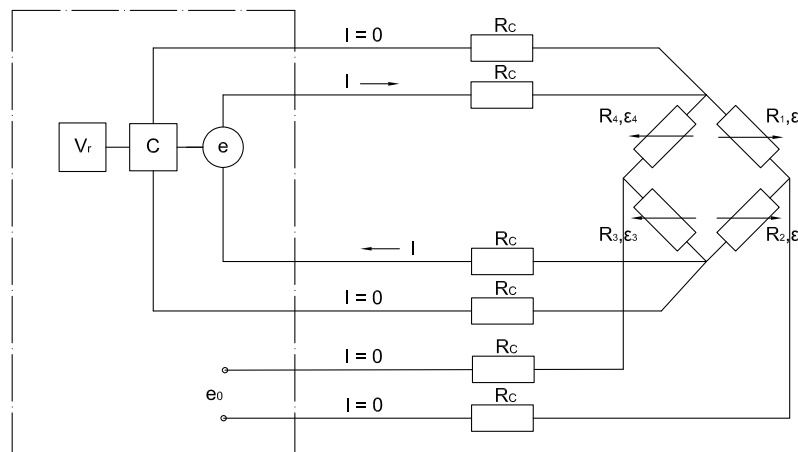
Figure 43 Six-wire connection of full-bridge circuit

Considering the large distances that there might be between full strain gauge bridges and Data AcQuisition (DAQ) in wind turbines, it is advisable to use the six-wire connection, as shown in Figure 40 and Figure 41. However, regardless of the type of bridge configuration and the electrical connection adopted, the calibration procedures described below can be applied.

The last issue to be evaluated during the gluing of the strain gages is the selection of the measurement section. It would be advisable to avoid zones with stress concentration that could be due by geometric discontinuities (as for example sharp corners, holes, changes in the cross-sectional area of the object) or proximity to supports (as for example bearings, flanges, bushings ...). In this sense, iteration between the accredited certification institutes and WT manufacturer's finite

MEASUREMENT OF MECHANICAL LOADS IN LARGE WIND TURBINES

element results is necessary. In some cases, however, it could be impossible to find a section which is completely free of stress concentration and this will add uncertainty to the measurement.

In wind turbine strain gage measurements, usually stress concentration could affect tower bottom bridges due to the geometric discontinuities of the door, tower top bridges due to the flange, shaft bridges due to bearings and blade root bridges due to the bushings. However, in all these cases the assessment, if the strain gage bridges have actually been installed outside the stress concentration regions, can be done by performing sensors calibration through unbalanced masses of the turbine, according to the model presented in paragraph 4.4.3. For example, for tower bending bridges a variation of the angle of yaw of the nacelle of 360 ° allows to generate sinusoidal moment due to the mass of the system nacelle, hub and rotor. If the output signal match the expected trend, the measurement section will be outside the stress concentration regions. Figure 44 and Figure 45 show the output signal from bending bridges glued respectively at 0.3 and 1.5 tower diameters from the top tower for a yaw revolution. It is evident that the signal recorded in Figure 44 is disturbed, while the one in Figure 45 is much more similar to a sinusoids this demonstrates that the section at 0.3 diameters from the tower top is in a stress concentration region and then unsuitable for the measurement.
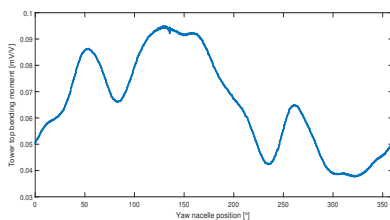
Figure 44 Tower top bending moment before reinstallation
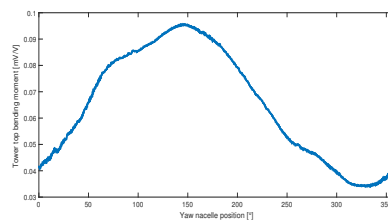
Figure 45 Tower top bending moment after reinstallation

Concerning this installation error, the new version of the standard [37] recommends to apply strain gauges at a distance of at least one diameter from the top tower, which it was not required in the old standard version in force when I started my PhD.

4.3 Network of DAQ systems

The strain gage full bridges for measuring the mechanical loads, preferably with a 6-wire connection, are usually connected to three data acquisition systems that form a DAQ network; a typical network of DAQ systems is reported in Figure 46. Two DAQ systems at tower top and at tower bottom are connected by Ethernet to the embedded pc which controls the data acquisition systems. A third DAQ is in the rotating hub and is connected by a Wifi LAN to the computer. The DAQ mounted in the hub is usually subject to interference, sometimes severe such as lightning and

electromagnetic discharge due electrified blades, and in general electromagnetic interference due to the generator, which can generate noise during measurement or even worse damage it; therefore, a ruggedized version is advisable.

All DAQ systems are synchronously sampling the output from the bridges at least 64 Hz, as recommended in [51]; a common time stamp is provided by a GPS clock.
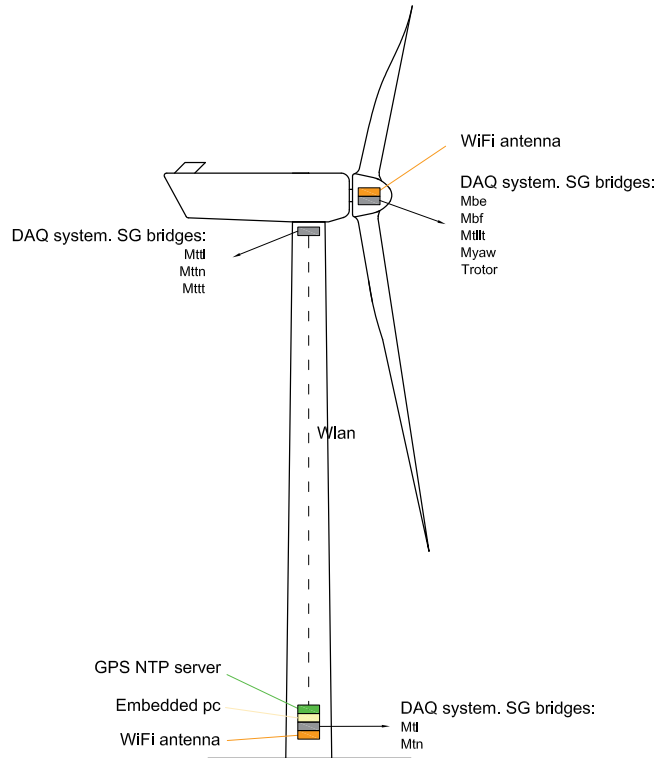
Figure 46 – The network of DAQ systems installed in the turbine

The configuration of the DAQ system network shown in Figure 46 is one of the possible solutions; variants can be applied according to the turbine being instrumented. In particular, if sliding contacts for transmitting high speed data are available, this solution is often preferable to Wifi solution due to the possible disconnection problems that can lead to data loss.

4.4   Suitable calibration methods

Calibration is the process through which it is possible to establish a physical relationship between the electrical signal output and the mechanical load input acting on the structure. This relationship is expressed mathematically by the coefficients of the calibration line, usually obtained by linear regression of input-output data.

In order to establish this relationship each bridge has to be calibrated versus a known reference input moment. Unfortunately, such an approach becomes

particularly complex in case of large wind turbines, due to their large dimensions (a 2 *MW* turbine is about 80-100 *m* tall, with 40-50 *m* long blades), and to the large magnitude of the loads necessary to cover the expected range in operation. Furthermore, in order to accurately apply a known input load, wind effects should be negligible or accurately predicted, and this is difficult to realize on-field.

Methods usually adopted to calibrate strain gage bridges on wind turbines, according to Table 14 [50], are: Analytical calibration, External load calibration and Gravity loads calibration. The three methods allow to reach different percentage of loads expected in operation and a different uncertainty, a comparison between analytical versus load-based calibration has been presented [148]. For each method, following is presented the calibration procedure.

Measured Quantity	Analytical	External load	Gravity
Blade bending moments		S	S, O
Main shaft torque[a]	S	S	
Main shaft bending	S	S	S, O
Tower bending moments	S	S	S, O
Tower torque[a]	S	S	
S = suitable for slope			
O = suitable for offset			
[a] For suitable methods for determining the offset, see 8.2.3.4 and 8.2.5.			

Table 14 Summary of suitable calibration methods [50].

In addition to what is shown in Table 14, for torsional bridge shaft, the standard also proposes to calibrate the sensor by measuring power output and rotor speed, taking into account the drive train efficiency and the turbine's power consumption. This type of calibration will be discussed in detail in section 4.5.

4.4.1 Load sensor calibration through analytical calibration

Analytical calibration allows to calibrate only the Wheatstone bridge and the associated DAQ system. It consists in applying a known change in resistance which simulates a specific strain of the strain gage. This deformation can be related to a known input moment through the use of Finite Element Method (FEM), using the properties of the materials and the geometry of the structure; method presented and discussed in [149]. However, the capacity of a FEM model to accurately describe the turbine deformation strongly depends on the accuracy to which are known material properties and part geometry. For this purpose, an accurate on-site measurement of the thickness and of the diameter of the metal structure must been done at the section where strain gages are mounted. The main advantages of this method are the simplicity and rapidity with which the calibration is performed, as well as the ability to cover the full measurement range expected during

operation. While the disadvantage is related to the great uncertainty of this technique and therefore it is often not advised by the standard authority.

Analytical calibration is usually applied to tower and shaft if a non-satisfactory calibration can be achieved by using external load calibration or gravity loads calibration methods. Conversely, this solution is never applied to blades, since the non-homogeneity of the material makes it impossible to convert simulated strain into mechanical moment.

Following, it is discussed the procedure that have to be executed for Analytical calibration of bending and torsional moment.

4.4.1.a   Analytical calibration for bending moment bridges

The analytical calibration has to be performed by putting the bending bridge in the unloaded position. In particular:

- for the shaft this implies to have the four strain gages on the neutral axis; the nacelle is oriented orthogonal to wind direction, to minimize loads.
- similarly, for the tower bending bridges, this implies to put the nacelle yaw perpendicular to the tower bending bridge.

The steps that have to be executed to realize the calibration process, according to the scheme reported in *Figure 47* ,are:

1. Acquisition of the bending strain gage bridge output $\frac{e_0}{e}$ during the application of the shunt calibrator;
2. Calculation of the equivalent strain ε to the variation of resistance introduced with the calibrator, according to equation (10).

$$\varepsilon = k * \frac{\Delta R}{R} \qquad (10)$$

   Where:

   a) k: Gauge factor of the bending strain gage bridge;
   b) ΔR: Variations of resistance introduced with the calibrator;
   c) R: Resistance of the bending strain gauge bridge.

3. Calculation of the equivalent bending moment M corresponding to the simulated strain introduced in step 2, through FEM analysis or the equation reported in *Figure 47*.

   Where:

   a) ε: Strain introduced in step 2;
   b) E: Young's modulus;
   c) $J = \frac{\pi}{64}\left(D_e{}^4 - D_i{}^4\right)$, where D_e and D_i are respectively the outer and inner diameters in the section of application of the strain gauges.

d) D_i: inner diameter in the section of application of the strain gauges.

4. Construction of the calibration curve $\frac{e_0}{e} = f(M_i)$.
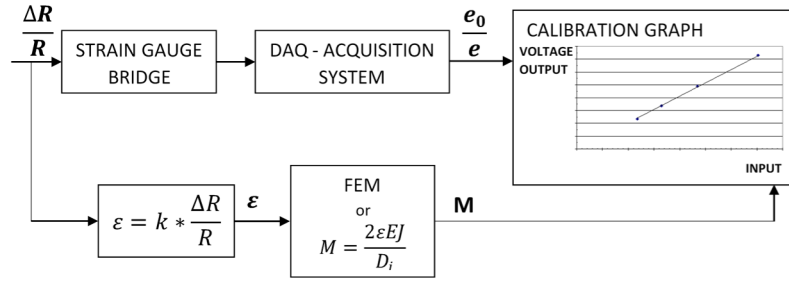
Figure 47 Scheme for Analytical calibration on the strain gauge bridges for measuring bending moments

4.4.1.b Analytical calibration for torsional moment bridges (Main shaft torque and Tower torque)

The following steps, according to the scheme reported in *Figure 48*, have to be executed to realize the calibration process:

1. Acquisition of the strain gage bridge output $\frac{e_0}{e}$ during the application of the shunt calibrator;

2. Calculation of the equivalent strain to the variation of resistance introduced with the calibrator, according to equation (10).

   Where:

   a. k: Gauge factor of the torque strain gage bridge;
   b. ΔR: Variations of resistance introduced with the calibrator;
   c. R: Resistance of the torque strain gauge bridge.

3. Calculation of the equivalent torque moment M_i to the strain introduced in step 2, through the following equation.

$$
\begin{aligned}
M &= \frac{\varepsilon\, E}{(1+v)} * \frac{2\pi\left(\frac{R_e + R_i}{2}\right)^2 (R_e - R_i)\left(1 + \frac{1}{4}\left(\frac{2(R_e - R_i)}{R_e + R_i}\right)^2\right)}{1 - \frac{1}{2}\left(\frac{2(R_e - R_i)}{R_e + R_i}\right)} \\
&= \frac{\varepsilon\, E}{(1+v)} * \frac{2\pi (R_m)^2 (t)\left(1 + \frac{1}{4}\left(\frac{t}{R_m}\right)^2\right)}{1 - \frac{1}{2}\left(\frac{t}{R_m}\right)}
\end{aligned}
\tag{11}
$$

   Where:

   a. ε: Strain introduced in step 2;
   b. E: is the Young modulus;
   c. v: is the Poisson's ratio;

    d. R_e and R_i are respectively the outer and inner radius in the section of application of the strain gauges;

    e. R_m is the mean radius, $Rm = \frac{R_e + R_i}{2}$;

    f. t is the thickness, $t = R_e - R_i$;

4.   Construction of the calibration curve $\frac{e_0}{e} = f(M_i)$.
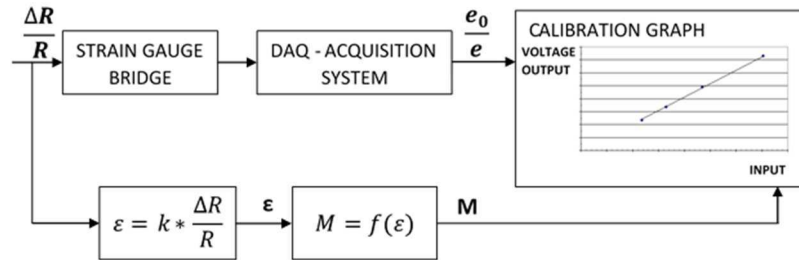
Figure 48 Scheme for Analytical calibration on the strain gauge bridges for measuring torque

4.4.2 Load sensor calibration through external load

Unlike analytical calibration, the calibration through external load and unbalanced masses of the turbine calibrates the entire measurement chain.

The external load calibration method involves applying large and accurately known mechanical loads to the turbine, comparable to those expected during operation. Figure *49* Blade and Shaft moments genereted by external mass hangs to the bladeFigure 49 and Figure 50 show the procedure to perform load sensor calibration through external load. In particular, a mass can be hung to the blade to generate blade bending moments, shaft bending moments and shaft torque as shown in Figure 49, while the tower can be pulled by ropes to generate known tower top bending moments, tower torque and tower bottom bending moments.

These loads M, which represent the input of the calibration process, will be correlated with the output signal on each bridge $\frac{e_0}{e}$ in order to construct the calibration line. The limitations related to this solution are the difficulty to apply huge loads even in connection with safety issues and the necessity to use long cables that they will easily oscillate, even in very low wind conditions, causing fluctuating inputs which again act as disturbances during the calibration process. For these reasons, this method is rarely used to calibrate strain gage bridges installed on large turbines.
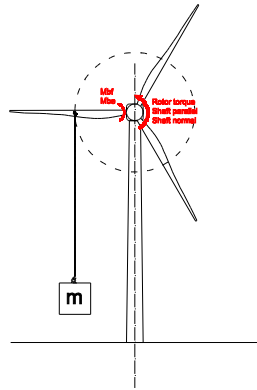
Figure 49 Blade and Shaft moments genereted by external mass hangs to the blade
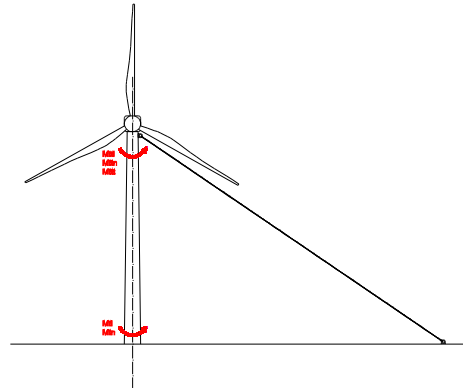
Figure 50 Tower top and tower bottom moments genereted by pulling the tower by ropes

4.4.3 Load sensor calibration through unbalanced masses of the turbine

This method allows to calibrate the full bridges installed in the turbine by using known unbalanced masses to load the parts under calibration. Figure 51 describes the concept of model-based calibration: the calibration plot reports in abscissa known input moments obtained by running a kinematic/dynamic model for a known status and geometrical configuration of the turbine, while on the ordinate it is reported the voltage output from the strain gage bridge recorded for that given status/configuration. If the model would be perfect, the actual input load would match the computed one; in real life, the model will be an uncertain description of the actual input acting on the turbine.
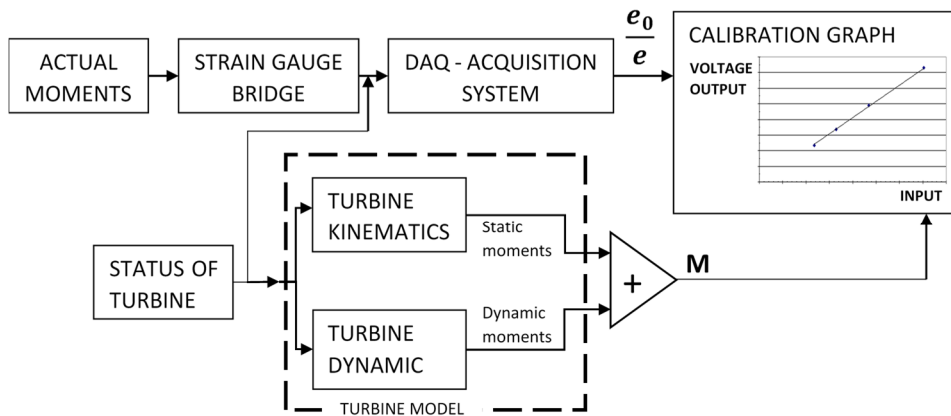
Figure 51 Scheme of analytical calibration: reference input load is based on known unbalanced masses and turbine modelling [156]

An accurate calibration based on models requires a complete static, kinematic and dynamic model of the turbine to be available, through which one knows the input loads applied to the turbine for given pitch, yaw and azimuth angles, as well as for given rotor speed and acceleration.

The following paragraphs present such a model; which can be used to determine the reference input for given turbine position and status; the many parameters appearing in the model have to be known.

This method can only be applied to the bending strain gage bridges of the turbine; however, for some of them, the method does not allow to reach a sufficiently high percentage of loads expected in operation. Therefore, for these bridges also an analytical calibration has to be performed.

However, even if calibration by unbalanced masses is questionable on the side of calibration range and attainable uncertainty, it also is often performed because it offers some advantages over direct application of external loads; in fact, it allows periodic recalibration, without the necessity of complex procedures and no modification to the turbine. Periodic recalibration is important, because strain gage bridges may drift during the long time needed for type certification (often several months of data acquisitions in variable weather conditions). Therefore, the analysis of such a calibration procedure is always relevant and is discussed in this thesis and it has been investigated in [156].

4.4.3.a   Blade bending moment

Known bending moments at the blade can be generated by the imbalance of the mass of the blade itself, given the position of the center of gravity and distribution of mass along the blade. In this case, a rotation of 360 ° of the rotor allows to generate a set of calibration points Figure 52.
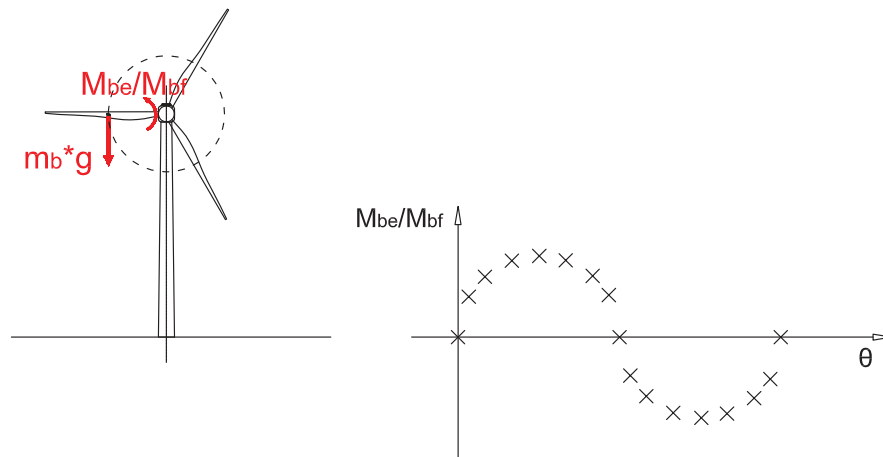
Figure 52 Blade bending moments generated by blade rotation over 360 ° [156]

One limitation of this method is represented by the limited range to the bending moment generated, typically 70 % of the edge and 35 % of the flap bending moments expected in operation; in most cases this is acceptable. The method assumes the blade to be rigid body, which is an approximation.

The proposed model is able to describe during static and dynamic operation the bending moments M_{be} and M_{bf} at the blade root (equations 12 and 13); similar models can be developed for blade bending moment distribution (blade moment distribution blade moment blade and blade edgewise bending moment distribution). These equations have been obtained with a simplified model that considers the mass of the part of the blade to the right of the strain gages (mb) applied on its center of gravity (G_b) and that G_b lies on the blade axis.

$$
\begin{aligned}
Mbe = M_{xb} = &-Ca_x - \dot{\omega} * \big(I_b xz * sin(\gamma) + I_b xx * cos(\beta) * cos - \\
&I_b xy * cos(\gamma) * sin(\beta)\big) - AG_b * \big(-Ta_y + AB\, mb\, \dot{\omega}\, cos(\beta) + \\
&AG_b mb\, \dot{\omega}\, cos(\gamma)\, cos(\beta) - AG_b\, mb\, \omega^2 sin(\beta)\, sin(\gamma) - \\
&AG_b\, mb\, \omega^2 sin\,(\beta)\, cos(\gamma)\, sin(\gamma)\big) - \omega^2 * sin(\gamma) * \big(I_b xy * cos(\beta) * \\
&cos(\gamma) - I_b yz * sin(\gamma) + I_b yy * cos(\gamma) * sin(\beta)\big) + \omega^2 * cos(\gamma) * \\
&sin(\beta) * \big(I_b zz * sin(\gamma) - I_b xz * cos(\beta) * cos(\gamma) + I_b yz * cos(\gamma) * \\
&sin(\beta)\big) + AG_b mb\, g * [sin(\beta) * (sin(\alpha) * cos(\gamma) + cos(\alpha) * cos(\vartheta) * \\
&sin(\gamma)) + cos(\alpha) * cos(\beta) * sin(\vartheta)]
\end{aligned}
\tag{12}
$$

$$
\begin{aligned}
Mbf = M_{yb} = &-Ca_y + \dot{\omega} * \big(I_b xy * cos(\beta) * cos(\gamma) - I_b yz * sin(\gamma) + \\
&I_b yy * cos(\gamma) * sin(\beta)\big) + AG_b * \big(-Ta_x + AB\, mb\, \dot{\omega}\, sin(\beta) + \\
&AG_b\, mb\, \dot{\omega}\, cos(\gamma)\, sin(\beta) + AB\, mb\, \omega^2 cos(\beta)\, sin(\gamma) + \\
&AG_b\, mb\, \omega^2 cos(\beta)\, cos(\gamma)\, sin(\gamma)\big) - \omega^2 * sin(\gamma) * \big(I_b xz * sin(\gamma) + \\
&I_b xx * cos(\beta) * cos(\gamma) - I_b xy * cos(\gamma) * sin(\beta)\big) + \omega^2 * cos(\gamma) * \\
&cos(\beta) * \big(I_b zz * sin(\gamma) - I_b xz * cos(\beta) * cos(\gamma) + I_b yz * cos(\gamma) * \\
&sin(\beta)\big) + AG_b\, mb\, g * [cos(\beta) * \big(sin(\alpha) * cos(\gamma) + cos(\alpha) * cos(\vartheta) * \\
&sin(\gamma)\big) - cos(\alpha) * sin(\beta) * sin(\vartheta)]
\end{aligned}
\tag{13}
$$

The parameters entered in the equations 12 and 13 are shown in Figure 53, where:
α → Tilt angle of the nacelle;
γ → Cone angle of the rotor;
θ → Rotation azimuth of the rotor;
β → Pitch angle of the blade relative to the reference system assumed, for the strain gages;
ω → Angular speed of the rotor;
$\dot{\omega}$ → Angular acceleration of the rotor;
mb → Mass of the part of the blade to the right of the strain gages.
$T_a; C_a$ → Force and moment of the Aerodynamic Load;

$AG_b \rightarrow$ Distance between the application section of the strain gages and the center of gravity of the part of the blade to the right of the strain gages;

$AB \rightarrow$ Distance between the application section of the strain gages on the blade and the rotation axis of the shaft;

$I_b \rightarrow$ Inertia matrix of the blade.
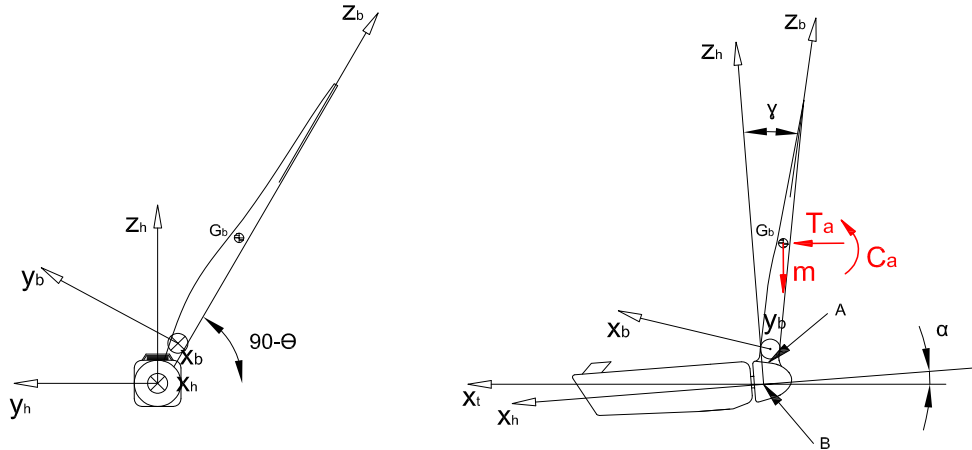
Figure 53 Reference systems and characteristic angles [156]

A model able to describe the dynamic loads is particularly useful for the periodic calibration checks required by the standard. In fact, they may be performed remotely, avoiding the presence of specialized personnel on the test site and the stop of the machine that would be necessary for static calibration, as long as the weather conditions are acceptable.

Wind effects below cut-in velocity are negligible, this is why the model neglects aerodynamic actions, whose knowledge would also be rather uncertain. In general, it is recommended not to use such a model for wind speeds larger than 3 *m/s*.

Despite the ability of the model to describe any condition of operation, it is recommended not to perform calibration in transient operating conditions. The above is justified by the objective difficulty of knowing:

1. accurate values of the moments of inertia of the blade;
2. aerodynamic contributions.

However, even the dynamic contribution in stationary conditions introduces a degree of uncertainty due to the uncertainty inherent in the dynamic parameters (such as rotation speed) and the aerodynamic contributions still acting at low rotation speed. For this reason, it is advisable to perform the calibration process in static conditions; the model reduces to equations 14 and 15. This calibration model will present the lower degree of uncertainty that can be achieved.

$$Mbe = M_{xb} = AG_b * mb * g * [sin(\beta) * (sin(\alpha) * cos(\gamma) + cos(\alpha) * cos(\vartheta) * sin(\gamma)) + cos(\alpha) * cos(\beta) * sin(\vartheta)] \tag{14}$$

$$Mbf = M_{yb} = AG_b * mb * g * [cos(\beta) * (sin(\alpha) * cos(\gamma) + cos(\alpha) * cos(\vartheta) * sin(\gamma)) - cos(\alpha) * sin(\beta) * sin(\vartheta)] \tag{15}$$

The output of the model is a function of the angular position of the blade and the angle of pitch. In order to maximize the mechanical load imposed on each bridge, it will be convenient to perform calibration for pitch values that allow to maximize the moments *Mbe* and *Mbf*. In particular, the moment *Mbe* assumes highest values for a pitch angle of 0° and the moment *Mbf* for a pitch angle of 90°.

By inserting the hypothetical values for a 2 *MW* machine, typical maximum moments that will be obtained during calibration procedure at low wind speed are (Equations 16 and 17):

$$Mbe_{max}(\vartheta = 0) \cong 1200000 \, [Nm] \tag{16}$$

$$Mbf_{max}(\vartheta = 90) \cong 1200000 \, [Nm] \tag{17}$$

Typically, on a 2 *MW* machine this method can produce an input bending moment up to 70 *%* and 35 *%* of the design bending moments *Mbe* and *Mbf* expected in operation for a class II turbine. Even if it is impossible to cover the full input range expected in operation, such percentage is acceptable if one considers the simplicity of the test if compared to the complexity of a calibration performed by pulling the blade with cables.

4.4.3.b   Shaft bending moment

The generation of *Shaft parallel* and *Shaft normal bending* moments on the rotating shaft can take place on the field by means of the weight of the rotor. A rotation of 360 ° of the rotor allows to generate a full cycle of bending, with change of sign and zero crossing. Limit of this method is the dependence of the calibration range on the mass of the rotating parts, their spatial distribution and the position of the center of gravity.

The proposed model is able to describe during static and dynamic operation of the machine the bending moments *Shaft parallel b.m.* and *Shaft normal b.m.* that act on the shaft in correspondence of the zone of application of the strain gages (equations 18 and 19). Where, *Shaft parallel b.m.* and *Shaft normal b.m.* are the parallel and normal bending moment with respect to the azimuth angle, so they are referred to a "rotating" frame on the shaft.

$$Shaft\ parallel\ b.m. = M_y = I_c xy * \dot{\omega} + I_r xy * \dot{\omega} + I_c xz * \omega^2 + I_r xz * \omega^2 - EG_c * g * m_c * cos(\alpha) * cos(\vartheta) - EG_r * g * m_r * cos(\alpha) * cos(\vartheta)$$ (18)

$$Shaft\ normal\ b.m. = M_z = I_c xz * \dot{\omega} + I_r xz * \dot{\omega} - I_c xy * \omega^2 - I_r xy * \omega^2 + EG_c * g * m_c * cos(\alpha) * sin(\vartheta) + EG_r * g * m_r * cos(\alpha) * sin(\vartheta)$$ (19)

The parameters entered in the equations 18 and 19 are shown in Figure 54:
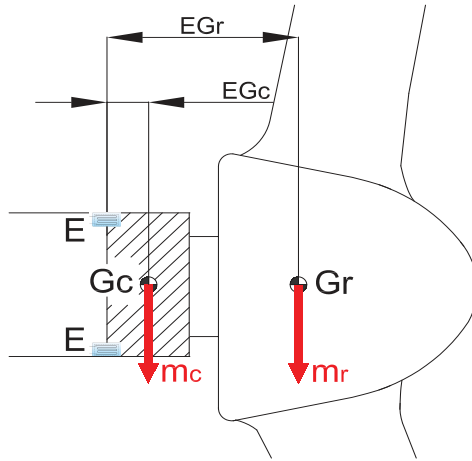
Figure 54 Development of known bending moments on the shaft [156]

EGc → Distance between the strain gages position and center of gravity of the part of shaft to the right of the strain gages;

EGr → Distance between the strain gages section and center of gravity of the system: rotor+hub;

mr → Mass of the system rotor and hub;

mc → Mass of the part of shaft to the right of the strain gages;

Ir → Inertia matrix of the system: rotor+hub;

Ic → Inertia matrix of the part of shaft to the right of the strain gages.

However, as mentioned before for the blade calibration, the dynamic contribution in stationary conditions introduces a degree of uncertainty due to the uncertainty inherent in the dynamic parameters and the aerodynamic contributions still acting at low rotation speed. For this reason, it is advisable to perform the calibration process in static conditions and at low wind speed. By inserting typical values for a 2 *MW* class II turbine, typical maximum moments that will be obtained during calibration procedure are (equations 20 and 21):

$$Shaft\ parallel\ b.m._{max}\ (\vartheta = 0) \cong 830000\ [Nm]$$ (20)

$$Shaft\ normal\ b.m._{max}\ (\vartheta = 90) \cong 830000\ [Nm]$$ (21)

Therefore, typically this method can produce an input bending moment up to 25 *%* of the design bending moment expected in operation for a class II turbine.

4.4.3.c   Tower bending moment

Known bending moments at the tower can be generated by the mass imbalance induced by the system nacelle, hub and rotor. In this case, a variation of the angle

of yaw of the nacelle of 360 ° allows to generate a set of calibration points, Figure 55.

A serious drawback of this method is the limited range to the bending moment generated by the imbalance of the masses with respect to what happens in operation, especially if the nacelle and rotor center of gravity is central to the tower. Contrary to what said for the blade, the load calibration thus obtained represents a very low percentage with respect to maximum design loads expected in operation, sometimes lower than 5-10 *%;* which is too low for a proper calibration.
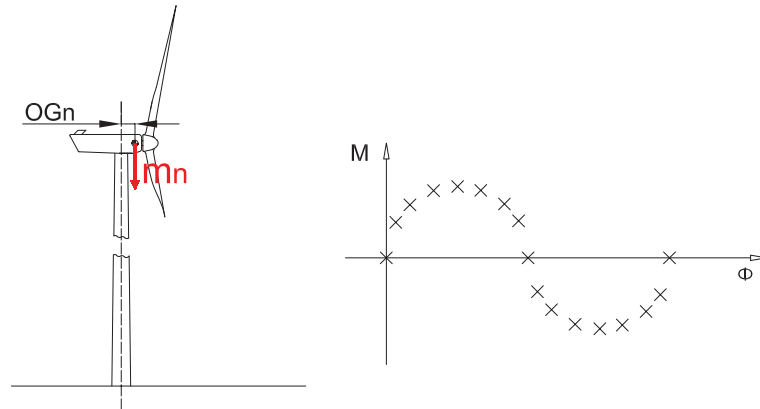
Figure 55 Development of bending moments known exploiting the imbalance of mass induced by the system nacelle, hub and rotor [156]

The applicability of this method is limited only to situations in which the center of gravity of the system nacelle, hub and rotor is not on the axis of the tower.

The bending moments *Mtl* and *Mtn* at tower base, the bending moments *Mtml* and *Mtmn* at tower mid and the bending moments *Mttl* and *Mttn* at tower top can be expressed as a function of yaw angle over 360 ° by equations *22*a-b-c and 23a-b-c. Where, the bending moment at tower bottom, tower mid and tower top are defined in normal direction (*Mtn*, *Mtmn* and *Mttn*) and lateral direction (*Mtl, Mtml* and *Mttl*) with respect to the zero angle of the yaw co-ordinate system defined. Therefore, the tower moments are referred to a non-rotating frame on the tower.

$$Mtl = -OGn * g * mn * cos(\phi) \qquad \text{(22-a)}$$

$$Mtml = -OGn * g * mn * cos(\phi) \qquad \text{(22-b)}$$

$$Mttl = -OGn * g * mn * cos(\phi) \qquad \text{(22-c)}$$

$$Mtn = -OGn * g * mn * sin(\phi) \qquad \text{(23-a)}$$

$$Mtmn = -OGn * g * mn * sin(\phi) \qquad \text{(23-b)}$$

$$Mttn = -OGn * g * mn * sin(\phi) \qquad\qquad (23\text{-}c)$$

where:

- *OGn*: Distance between tower axis and the center of gravity of the system nacelle, hub and rotor;
- *g*: Acceleration of gravity;
- *mn*: Massa of the system nacelle, hub and rotor;
- ϕ : yaw angle of the nacelle, ϕ = 0 for nacelle axis coinciding with axis passing through the bridges *Mttn, Mtmn* and *Mtn*.

Since *OGn* is function of pitch of the blade, it is recommended, in order to maximize the load, to perform the calibration process by placing the blades in a configuration that allows to maximize the generated moment.

By inserting typical values for a 2 *MW* class II turbine with nacelle center of gravity rather close to tower axis, typical maximum moments that will be recorded for static operation conditions of the machine and for the wind speed equal to zero (equations *24* and 25):

$$Mttl_{max}(\phi = 0) = Mtml_{max}(\phi = 0) = Mtl_{max}(\phi = 0)$$
$$\cong 260000\ [Nm] \qquad\qquad (24)$$

$$Mttn_{max}(\phi = 90) = Mtmn_{max}(\phi = 90) = Mtn_{max}(\phi = 90)$$
$$\cong 260000\ [Nm] \qquad\qquad (25)$$

4.5 Main shaft torque: measurement problems and calibration procedure through measuring power output and rotor speed

The methods used to measure torque on wind turbine shaft can be divided into two categories, either direct or indirect.

Direct methods use in-line torque transducers, already calibrated by the manufacturer, which are integrated into the drive shaft. The major obstacle to the industrial application of direct measurement systems is the costly and intrusive nature of the required equipment, which is impractical for wind turbine application.

Indirect methods are based on the measurement of torque-related parameters and subsequent torque calculation. These methods have the advantage of avoiding modifications to the original shaft, therefore minimising the impact on mechanical design and not modifying the static and dynamic behaviour of the shaft. The conventional indirect systems are based on measurement of surface strain or angle of twist [151].

Among the different solutions, the IEC 61400-13 recommends to use full strain gage bridges, as shown in *Figure 41*, because it can optimize cost, sensitivity and has a

low intrusiveness. However, the main limitations of this method are the complexity of installation of the sensors on cylindrical surfaces, the need to install electronics on the rotating shaft, the requirement for specialised personnel required for installation, usability, resolution, noise susceptibility and the requirement for regular calibration. Moreover, unwanted forces can create unintended directional disturbance, such as cross talk phenomena, that can increase the uncertainty in the measured loads and reduce accuracy [152]. In order to overcome some of the limits associated with strain gages application for torque analysis on wind turbines, a non-intrusive and low cost solution is presented in chapter 6. However, strain gages are at present the most widely used solution for this application.

Transferring a load to a sensor sometimes it is intentional and sometimes not; when the transfer is not intentional the measurement will be subject to errore, called cross talk. In strain gage measurement on wind turbine, this error often occurs in rotor blade bending measurements [155] and shaft bending and torsion measurements due to the non-homogeneity of polymeric blade materials and the local stress concentration in the measurement sections of the shaft. The IEC 61400-13 [50] recommends to calculate a calibration matrix to find and eventually compensate this effect.

For torsional bridge of the shaft, the check of cross talk problem can be performed through a low speed rotor revolution in no-wind conditions. The purpose is to load only the bending bridges of the shaft; therefore, if the measured torque signal shows a trend dependent by the azimuth rotor position, as shown in Figure 56, the torsional sensor is affected by cross talk. Typically, on wind turbines application, this error, represented by the ratio between the cross talk amplitude A_{CT} and the maximum expected torque T_{rotor_max}, can reach values up to 10%.
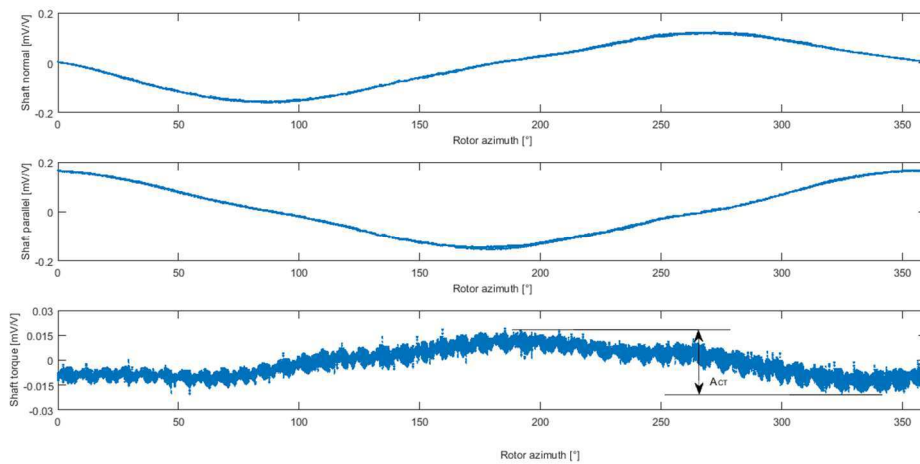
Figure 56 Signals during a series of rotor rotation under no-wind show cross-talk between channels

The calibration of indirect sensor for shaft torsional measurement, like strain gage sensor, can be achieved by analytical calibration or external loads, according to *Table 14*. The application of external load is usually obstructed by saftey issues, as described in section 4.4.2. However, an external load can be applied in workshop, prior to transport the machine to the field; for example, applying a load by a crane. This calibration procedure is rather easy and fast but the applicable torque values are often very small compared to the maximum load expected in operation. Alternatively, calibration can be done by accelerating the rotor, while recording angular velocity and acceleration, synchronous to the recording of the output of the bridge measuring torque. By knowledge of the moment of inertia of the rotating parts in front of the section where torque is measured, torque T_{rotor} can be computed as the product of angular acceleration $\dot{\omega}$ to inertia *I,* according to equation (26). This torque will be used as the input value for calibrating the torque measurement.

$$T_{rotor} = I\,\dot{\omega} \tag{26}$$

Given the problems of cross-talk just described, the implementation of this method is often not feasible.

The last solution, often used and recommended by the standard [50], performs main shaft torque calibration by measuring the power output P_{El_a} and rotor speed ω, taking the drive train and generator efficiency η, as shown in equation (27). Due to cross talk problems, that often affect torque signal, and the noise that could afflict the torque and power signals, it would be advisable to carry out the comparison among average data from 10 minutes time histories. Moreover, in order to have a reference value for torque input with a sufficiently small uncertainty, it would be advisable to use only recordings of the electric active power output with low standard deviation, usually less than 5.0% of the mean electric power.

$$T_{rotor\_ref} = \frac{P_{El\_a}}{\omega\,\eta} \tag{27}$$

The generator efficiency is usually determined by the calibration data of the generator which are obtained by a back-to-back test procedure according to the standards IEC-60034. Generator performance is usually certified for some speed and power values but for a single temperature value. However, in order to obtain the generator efficiency for each average power data and average speed data, a three-dimensional interpolation curve must be calculated, as shown in Figure 57.
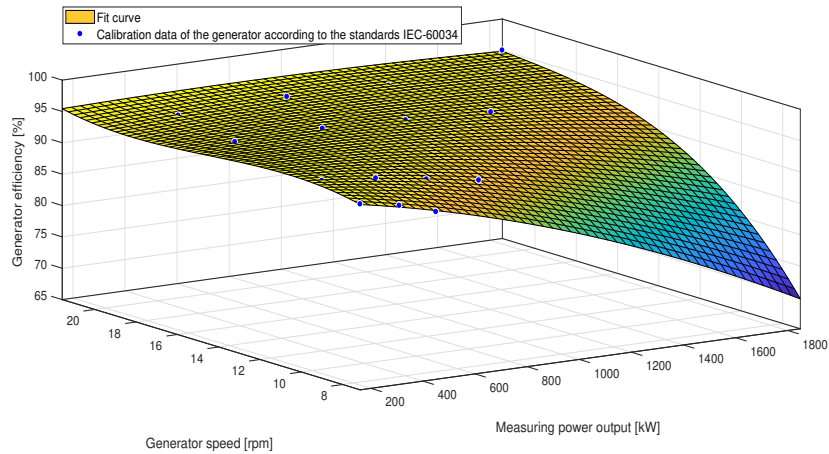
Figure 57 – Generator efficiency vs. angular speed and power

The generator temperature during the calibration process of the shaft torsional bridge could not coincide with that of certification of the generator performance, this could lead to hardly controllable and compensable errors in the calibration process of torsional bridge.

Despite the limits regarding shaft torque measurement on wind turbine, this measure is worthy of great attention because allows the optimization of the generated electric power, monitoring of dynamic performance, condition monitoring for predictive maintenance and control of mechanical systems.

5 MEASUREMENT OF MECHANICAL LOADS IN LARGE WIND TURBINES: UNCERTAINTY ANALYSIS

In case of Gravity loads method, such as those presented in the previous chapter, the uncertainty on each parameter used in the model will determine a combined uncertainty of the input reference load which often can reach large values. Literature suggests that the reference input used in a calibration process should have an uncertainty lower or equal to 1/4 of the measurement uncertainty of the device being calibrated, see for example [158]. The calibration process would then provide scattered data, which allow a statistical estimation of uncertainty (Type A according to the GUM [157]). The overall calibration uncertainty could then be computed (Type B according to the GUM) by combining reference uncertainty with the statistical one. However, in Paragraph 5.2 we will show that the contribution of the input reference uncertainty can be neglected if it is one order of magnitude lower than desired uncertainty set for the load measurement, which is 3 *%* according to the IEC-61400-13. We propose to use this approach in a model based calibration, therefore we will discuss to which extent the uncertainty of the reference input generated by unbalanced masses can meet this goal and then become negligible.

Even if measurements should take place in isothermal effects, this is not always the case in real world practice. Therefore, the thermal effects on strain gage bridges are also discussed, putting into evidence its influence on calibration and signal uncertainty both for full bridges in T configuration and in parallel configuration.

5.1 Total uncertainty analysis according to the standard IEC 61400-13:2015 [50]

The total standard uncertainty of an uncombined quantity is given by equation (28),

$$U^2_{t\_M_i} = U^2_{cal\_M_i} + U^2_{sig\_M_i} \qquad (28)$$

where $U_{cal\_M_i}$ is the calibration uncertainty and $U_{sig\_M_i}$ the signal uncertainty.

The calibration curves, as described in chapter 4, are determined by correlating the input data loads and the recorded electrical output given during the calibration process. In most of the cases the transfer function is defined by a slope and an offset, but also higher order functions could be possible. Different calibration techniques can be applied according to the standard [50]: Analytical calibration, External load calibration and Gravity loads calibration. Every calibration method contains various contribution of Type A and Type B uncertainties which should be taken into account in the analysis of calibration uncertainty. An example of calibration uncertainty for Gravity loads calibration is presented in paragraph 5.3.

Ideally, all the operating conditions of the transducer should be tested during the calibration process, so that the total uncertainty can be estimated by calibration uncertainty. In reality, additional effects, defined as signal uncertainty, occur during the measurement campaign and can significantly contribute to total uncertainty. The most important signal uncertainty contributions are:

- additional noise (electromagnetic distortion)
- temperature effects (drift effects)

This chapter, at paragraph 5.4 and 5.5, will discuss how the thermal phenomenon can affect total uncertainty. In particular, it will be discussed how and how much the thermal contribution can affect the signal uncertainty $U_{sig\_M_i}(T)$ and the calibration uncertainty $U_{cal\_M_i}(T)$, if temperature effects occur during the calibration process.

5.2 Temperature compensation according to the standard IEC 61400-13:2015 [50]

Strain gauge measurements are influenced by the temperature of the measured material. In most cases, temperature effects can be compensated by selecting the type and the configuration of the strain gage bridge according to the component material and the wind turbine section. However, in any case temperature drifts can occur.

In order to avoid high-offset drift, the standard recommends to install a temperature measurement close to the position of each strain gauge and to obtain a calibration curve including temperature dependencies. For example, Figure 58 shows a typical linear regression through the offsets derived from the different calibration runs.

In addition, the standard recommends to apply a filter based on the measured thermal phenomenon, which it will allow to filter out the recorded data during extreme thermal events, that may still be uncertain even if thermal compensation is applied. This means additional improvement in accuracy for the resulting signal.

According to the standard, thermal effect acting on a strain gage bridge affects the offset of the transducer; therefore, only the maximum loads may be subject to thermal errors while no effect is expected on the rainflow spectra results. However, paragraph 5.4 will demonstrate how a thermal contribution induces a sensitivity shift, therefore in contradiction to what declared in the standard also an error on rainflow spectra due to thermal effect is expected.
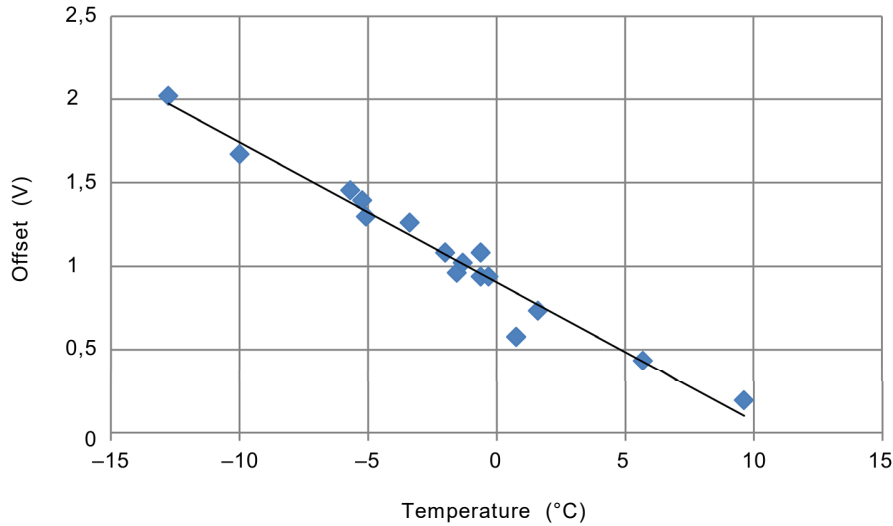
Figure 58 Linear regression through the offsets derived from the different calibration runs [50]

5.3 Calibration uncertainty – real case application

The calibration process is realized by *N* pairs of samples $(M_i; \frac{e_{oMi}}{e})$. In fact, during the calibration process, we record the electric output voltage $\frac{e_{oMi}}{e}$ of the measurement system and we plot it versus the input moment M_i simulated by shunt calibrator or provided by external loads or by the models introduced in paragraphs 4.4.3.a, 4.4.3.b and 4.4.3.c. A least square linear regression will provide the calibration function, while the scatter of calibration data estimated through a classical residual analysis, will provide information on calibration uncertainty $U_{cal\_M_i}$.

Figure 59 reports a typical data set acquired on a blade; the reference bending moment M_{be} reported in the abscissa is computed by the mechanical model of equation (12), while the bridge electrical output $\frac{e_{oMbe}}{e}$ reported in the ordinate is recorded by the DAQ system.

These calibration data allow to determine the regression line by a least square fit, which returns the straight line

$$\frac{e_{oMi}}{e} = f(M_i) = m_i M_i + b_i \qquad (29)$$

Where:

m_i = slope of the calibration line of the i-th bridge, i.e. sensor sensitivity;

b_i = ordinate at the origin of the calibration line of the i-th bridge;
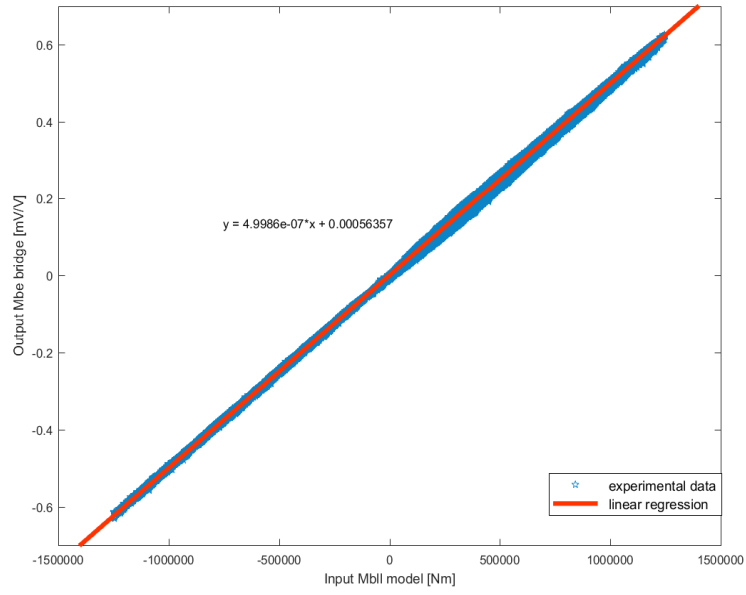
Figure 59 Calibration data for Mbe [156].

The standard deviations of m_i and b_i can be computed by Type A method, i.e. by performing a statistical analysis of the residuals of the *N* calibration data with respect to their interpolating line $\frac{e_{oMi}}{e} = m_i M_i + b_i$:

$$s_{m_i} = \sqrt{\frac{N S^2_{\left(\frac{e_{oMi}}{e}\right)}}{N \sum_{k=1}^{N} M_{i_k}^2 - \left(\sum_{k=1}^{N} M_{i_k}\right)^2}} \tag{30}$$

$$s_{b_i} = \sqrt{\frac{S^2_{\left(\frac{e_{oMi}}{e}\right)} \sum_{k=1}^{N} M_{i_k}^2}{N \sum_{k=1}^{N} M_{i_k}^2 - \left(\sum_{k=1}^{N} M_{i_k}\right)^2}} \tag{31}$$

$$s^2_{\left(\frac{e_{oMi}}{e}\right)} = \frac{1}{N-2} \sum_{k=1}^{N} \left(m_i M_{i_k} + b_i - \frac{e_{0M_{i_k}}}{e}\right)^2 \tag{32}$$

While the standard deviation of the input moment M_i is:

$$s_{M_i} = \sqrt{\frac{1}{N-2} \sum_{k=1}^{N} \left(\frac{\frac{e_{0M_{i_k}}}{e} - b_i}{m_i} - M_{i_k}\right)^2} \tag{33}$$

MEASUREMENT OF MECHANICAL LOADS IN LARGE WIND TURBINES

In physical terms, s_{M_i} is the uncertainty caused during the calibration process by strain gage installation, Wheatstone bridge, connecting cables, amplifier and digital acquisition system as well as any non-linearity which are not accounted for in the kinematic/dynamic model; but it is only a component of the calibration uncertainty.

The calibration uncertainty $U_{cal\_M_i}$ of each moment M_i is computed according the GUM as expanded uncertainty with a coverage factor k_p=2, allowing for a 95 *%* confidence level,

$$U_{cal\_M_i} = k_p U_{CMi} \tag{34}$$

where U_{CMi} is the combined standard uncertainty of each *Mi* moment and is computed as type B uncertainty as shown in equation (35), according with the GUM.

$$U_{cal\_M_i} = \sqrt{u_{M\,calibration-i}{}^2 + s_{M_i}{}^2} \tag{35}$$

Equation (35) shows that the uncertainty of the reference input load $u_{M\,calibration-i}$ is a component of the combined uncertainty of the instrument to be calibrated. However, its relative contribution to the combined uncertainty depends on the ratio R_U between desired combined uncertainty $Desired\_U_{CMi}$ and uncertainty of the reference $u_{M\,calibration-i}$. Table 15 shows, for a given desired uncertainty set equal to 1, the resulting combined standard uncertainty for different R_U.

$Desired\_U_{CMi}$	1.000									
$R_U = \dfrac{Desired\_U_{CMi}}{u_{M\,calibration-i}}$	1	2	3	4	5	6	7	8	9	10
$u_{M\,calibration-i}$	1.000	0.500	0.333	0.250	0.200	0.167	0.143	0.125	0.111	0.100
U_{CMi}	1.4142	1.1180	1.0541	<u>1.0308</u>	1.0198	1.0138	1.0102	1.0078	1.0061	<u>1.0049</u>

Table 15 Combined standard uncertainty for ratios, R$_U$s, between 1 and 10 [156].

Literature reports a minimum recommended ratio $R_U \geq 4$ in a calibration process [158]; this is justified because at this ratio, the contribution of the reference uncertainty does not impact on the first significant digit of combined standard uncertainty, as it can be seen on the Table 15 when comparing attainable U_{CMi} to $Desired\_U_{CMi}$. However, in this thesis, we suggest a ratio equal to 10; it is preferable because in such case the contribution of the reference uncertainty drops to the third digit of combined uncertainty and therefore $u_{M\,calibration-i}$ may be neglected in the calculation of U_{CMi}.

When the reference bending moments have been simulated by shunt calibrator, the uncertainty of the reference $u_{M\,calibration-i}$ has to be calculated according the annex B of the standard IEC 61400:13 − 2015; the achievement of the target $R_U =$

10 dependents on the uncertainty with which as know the parameters used to convert the variation of resistance, introduced with the shunt calibrator, in mechanical moment, according to paragraph 4.4.1. While, in case of calibration trough gravity loads, the uncertainty of the reference input depends on the parameters used in the models described in paragraphs 4.4.3.a, 4.4.3.b and 4.4.3.c.

In the presented models for load sensor calibration through unbalanced masses of the turbine some parameters are correlated, for example, blade angular position, angular velocity and angular acceleration. However, if one decides to perform the calibration process under static conditions (i.e. wind turbine parked and low wind, typically 3 m/s), for the reasons discussed earlier, it can be assumed that the parameters in the equations of the models are independent quantities. Then the combined standard uncertainty can be computed according to the expression of uncertainty propagation for uncorrelated quantities (equation (36)).

$$u_{M_{calibration-i}} = \sqrt{\sum_{j=1}^{N} \left(\frac{\partial f}{\partial x_j}\right)^2 * u_{x_j}^2} \qquad (36)$$

From the analysis of this relationship it is also possible to observe that if it is decided to perform a calibration process in non-static conditions the uncertainty of the input moments and then of the calibration process would tend to increase significantly. This point is further strengthened by the fact that terms appearing in dynamic operating conditions (moment of inertia, aerodynamic contributions …) are known with relatively large uncertainty.

Table 16 reports for each bending moment ($M_{calibration-i}$), computed in static condition, the typical values of all parameters x_j with the associated uncertainty values used in the model. These data are referred to and are representative of a typical direct drive wind turbine having 2 MW power, an 80 m tall cylindrical tower made in steel, a rotor with 3 blades in fiber glass composite 45 m long. The uncertainty associated to each parameter u_{x_j} has been reported according to the GUM specifications [157]. In particular, it is reported the standard deviation s_j for those x_j parameters for which such statistical information is available from measured data, whose distribution is assumed Gaussian and uncertainty $u_{x_j} = s_j$, while for the other parameters it is reported the half-width tolerance a_j available from design specifications. We recall that in case of half-width tolerances it is assumed a continuous uniform probability distribution having width (2 a_j), whose standard deviation $u_{x_j} = \frac{a_j}{\sqrt{3}}$.

X_j			Standard deviation s_j	Half-width Tolerance a_j
Symbol	Name	Value		
α	Nacelle tilt	7°		0.5 °
γ	Rotor cone angle	2.5°		0.3 °
β	Blade pitch	0° or 90°		0.1 °
θ	Rotor azimuth	0°÷360°		0.1 °
mb	Mass of the part of the blade to the right of the strain gages	9000 kg	55 kg	
AG_b	Distance between the application section of the strain gages and the center of gravity of the part of the blade to the right of the strain gages	15.0 m		0.1 m
mc	Shaft mass between the section of the strain gages and the shaft end	2800kg		2.5 %
mr	Rotor mass	46000 kg		2.5 %
EGc	Distance between the strain gages section and the center of gravity of the shaft section	0.2 m		2 %
EGr	Distance between the strain gages section and the rotor center of gravity	2.0 m		2 %
m_n	Nacelle mass	103000 kg		5 %
OG_n	Distance between the tower axis and the nacelle center of gravity	0.25 m		2 %

Table 16 Values and uncertainties of all bending moments [156]

Table 17 shows the resulting uncertainty $u_{M calibration-i}$ of all bending moments computed from equation (36) and its value $\frac{u_{M calibration-i}}{Mi\_max}$ relative to the expected design loads. These uncertainties are expressed as one standard deviation.

Moment	u_{model_Mi} $[Nm]$	$\frac{u_{model\_Mi}}{Mi\_max}$ $[\%]$
Mbe	9000	0.6
Mbf	9000	0.4
Shaft parallel b.m.	15000	0.5
Shaft normal b.m.	15000	0.5
Mttl, Mttn	5000	0.2
Mtl, Mtn	5000	0.2

Table 17 Uncertainty of all bending moments [156]

All uncertainties are one order of magnitude lower than target uncertainty (3 %) set by the GUM and IEC-61400/13. Therefore, based on what has been said before, the input bending moments, calculated by the model described above, can be adopted as a suitable reference input in the calibration process.

5.4 Calibration and signal uncertainty due to temperature effects – real case application

Several reasons cause temperature differences between the points where strain gages are installed. The most relevant are: a) solar radiation, which heats the parts exposed to it; b) heat sources internal to the WT, which depends on power production; c) convective heat exchange with external and internal air flows.

In order to have an insight into thermal distribution in wind turbine, we have used infrared images for a qualitative estimate of temperature distribution and temperature sensors (Pt100) inside the tower, close to locations where strain gages are installed, to have local measurements.

During full production thermal effects are very large, as it can be observed from the infra-red images reported in Figure *60* and Figure *61*. Infrared images are taken on a 2 *MW* turbine operating at full power. Images are acquired at night, in clear sky with no clouds in order to observed only internal heat production and convective heat exchange without disturbing radiation from sun or environment. Air temperature was about 15 *°C* and severe thermal gradients are clearly visible in the infrared images. The temperature sensors placed inside the tower close to the strain gages showed temperature differences up to 20°C.
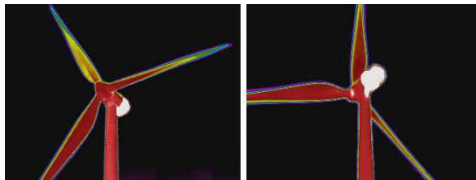
Figure 60 Thermal image of the tower top
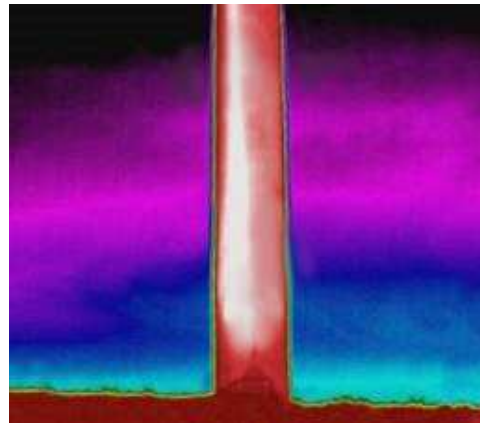
Figure 61 Thermal influence of the power converters on the strain gages on the tower bottom

Even if during calibration the low wind speed and the low power tend to reduce thermal effects, still, in a sunny day, it is easy to measure temperature differences larger than 10 *℃*, due mainly to solar radiation.

Therefore, in order to approach isothermal conditions, it would be advisable to perform calibration with overcast sky or at night, so to minimize direct solar radiation. However, even in such conditions, during the calibration process, which may last 30 to 60 min, one may observe time dependent variation of temperature of several degrees Celsius. Therefore, it becomes important to investigate thermal effects on calibration uncertainties $U_{cal\_M_i}(T)$ and signal uncertainty $U_{sig\_M_i}(T)$.

In addition to the measurement signal that depends on mechanical strain, each strain gage bridge generates also a superimposed signal dependent on temperature. Thermal effects on a strain gage transducer appear as the combination of two phenomena: zero drift and sensitivity shift.

Zero drift is a variation in the transducer output due to its temperature variation. The causes of this drift are the change in the resistance of the grid, the different coefficient of the foil and the base material on which the strain gages are glued [160]; which they will cause an apparent strain on each strain gage of the bridge defined as:

$$\varepsilon_{sL} = \left(\frac{\alpha_r}{K} + \alpha_b - \alpha_m\right) * T_s \qquad (37)$$

Where:
ε_{sL} = apparent strain of the strain gauge;
α_r = temperature coefficient of the electrical resistance of the measuring grid foil;
α_b = thermal expansion coefficient of the measurement object;
α_m = thermal expansion coefficient of the measuring grid material;
k= gauge factor of the strain gauge;
T_s = strain gage operating temperature minus strain gage calibration temperature (typically 20 °C).

Countermeasures to minimize apparent strain can be implemented during the choice of the strain gauges. Indeed, it can be used a strain gage with a thermal coefficient of electrical resistance of the measuring grid foil equal to the material on which the sensor will be installed, so that the terms of the equation cancel each other out; *α_r = (α_m - α_b) * k*.

However, the apparent strain shown in equation (37) is a simplified representation, containing only the linear components. A residual errors ε_{sR}, for each batch of strain gauges is made available by the manufacturer in form of a diagram and polynomial curve and should to be taken into account.

Therefore, the apparent overall strain will be:

- $\varepsilon_{sTOT} = \varepsilon_{sL} + \varepsilon_{sR}$: for strain gauge not auto compensated for the material over which is installed;
- $\varepsilon_{sTOT} = \varepsilon_{sR}$: for strain gauge auto compensated for the material over which is installed.

The apparent overall strain ε_{sTOT}, of each strain gage of the bridge, contributes to the apparent electrical output, according to the bridge equation defined in Figure 40 and Figure 41.

Zero drift due to thermally induced apparent strain is usually compensated by realizing a full bridge. However, this solution is effective only if the apparent strain is equal for all the four strain gages of the bridge. This occurs when the strain gages are at the same temperature and have the same apparent strain curve, i.e. the strain gages have the same behaviour under the same thermal effects.

Data available in literature for strain gage load cells [160] report a thermal output from a full bridge in the order of $0.15 \; \frac{\mu V}{V°C}$ even if the four stain gages were coming from the same batch and isothermal conditions occur. This means that a perfect matching of strain gages is impossible to achieve. Considering that a typical bridge output at full scale is in the order of 1÷2 *mV/V*, then thermal drift account for approximately 0.015 *%/°C*, which will lead to about 0.1 *%* for a temperature variation of 5÷7 *°C* during the calibration process.

In case the calibration process is not executed under isothermal condition and thermal gradients are present between the strain gages of the full bridge, then results will chance significantly depending on type of bridge configuration. For a T configuration the thermal gradients will not affect the results. In a parallel configuration, thermal differences between the two sides of the bridge are not compensated and they account for about $2 \; \frac{\mu V}{V°C}$ even if using strain gages auto-compensated for the material. Over a typical bridge output at full scale of 1÷2 *mV/V*, the thermal drift with parallel strain gages account for approximately 0.2 *%/°C*, which means about 1 % for a temperature difference of 5 *°C* between the two sides of the bridge during the calibration process.

Sensitivity shift is defined as the change in sensitivity *m* of the transducer as function of average temperature among the strain gages of the bridge T_{mean}.

The sensitivity of a strain gage-based transducer is defined as ratio of sensor output $\frac{e_0}{e}$ to input moment *M*:

$$m = \frac{\frac{e_0}{e}}{M} = \frac{k\varepsilon}{M} = f(k, \frac{1}{E}, \frac{1}{R_m^3}) \qquad (38)$$

where:

- e_0 = electric output voltage;
- e = excitation voltage;
- M = Bending moment;
- E = Young's modulus in the section of application of the strain gages;

- R_m = mean radius in the section of application of the strain gages;
- ε = deformation;
- k = Gage factor of the strain gage.

Temperature changes will affect all the three parameters which appear in the expression for sensor sensitivity of a strain gage-based transducer [160]. In fact, the temperature modifies:

- the geometry of the transducer body, $R_m(T_{mean})$;
- the Young's modulus of the transducer body, $E(T_{mean})$;
- the gage factor of the strain gage, $k(T_{mean})$.

If the strain gages characteristics have not been selected so to compensate their thermal dependence between each other, then we can consider R_m, E and k uncorrelated parameters. Therefore, sensitivity m has a standard deviation s_m per unit temperature variation represented in the following equation:

$$\frac{1}{T_{mean}} \frac{S_m}{m} = \sqrt{\left(\frac{1}{T_{mean}} \frac{u_k}{k}\right)^2 + \left(\frac{1}{T_{mean}} \frac{u_E}{E}\right)^2 + \left(\frac{1}{3} \frac{1}{T_{mean}} \frac{u_{R_m}}{R_m}\right)^2} \qquad (39)$$

Assuming:

- to use a batch of strain gages having k=2.07 and a temperature coefficient $\frac{u_k}{T_{mean}} = 93 * 10^{-6}$ 1/°C;
- that the Young's modulus of steel material of the tower and shaft is equal to 200 GPa with a temperature coefficient $\frac{u_E}{T_{mean}} = 51 \, MPa/°C$ [161];
- that the coefficient of thermal expansion of the steel is equal to $\frac{u_{R_m}}{T_{mean}} = 12 * 10^{-6}$ 1/°C.

The sensitivity shift for a typical bridge glued on steel materials is in the order of 0.03 %/°C, which will lead to about 0.2 % for a temperature variation of 5÷7 °C during the calibration process. Approximately, this result may be also extended to the case of strain gage glued on fiberglass material.

Now the calibration uncertainty due to thermal effects $U_{cal\_M_i}(T)$ is estimated by combining zero drift and sensitivity shift. For a full bridge in T or parallel configuration, the calibration uncertainty will reach about $U_{cal\_M_i}(T) = 0.2$ % for a temperature variation of 5÷7 *°C* during the calibration process. If we consider also a temperature difference of 5 *°C* between the two sides of the bridge during the calibration process, in case of a full bridge in parallel configuration the value becomes larger, about $U_{cal\_M_i}(T) = 1$ %, while it does not change significantly in T configuration. Taking into account these results, we conclude that during calibration temperature should remain as constant as possible, with maximum acceptable variations of 5 *°C* for bridges in T configuration and lower than 1 °C for parallel bridges.

The thermal effects described above will present also during all measurement campaign. The large range of the operating temperature of the full bridges and thermal gradients between the strain gages could lead the uncertainty at larger values. Therefore, care should be taken to avoid that this error, i.e. signal uncertainty, becomes larger than the target uncertainty (3 *%*) set by the standard.

For that purpose, the T configuration should be preferred in tower top and bottom bending moment, because it allows compensating the temperature difference between the two sides of the bridge. Experimental evidence of such thermal problems on bridge in parallel configuration measuring tower bending is presented in Figure 62, which reports data recorded during a non-windy day. The solar radiation, which heats a part of the tower, causes severe thermal induced drift from sunrise to sunset. In a cloudy day this problem disappears.
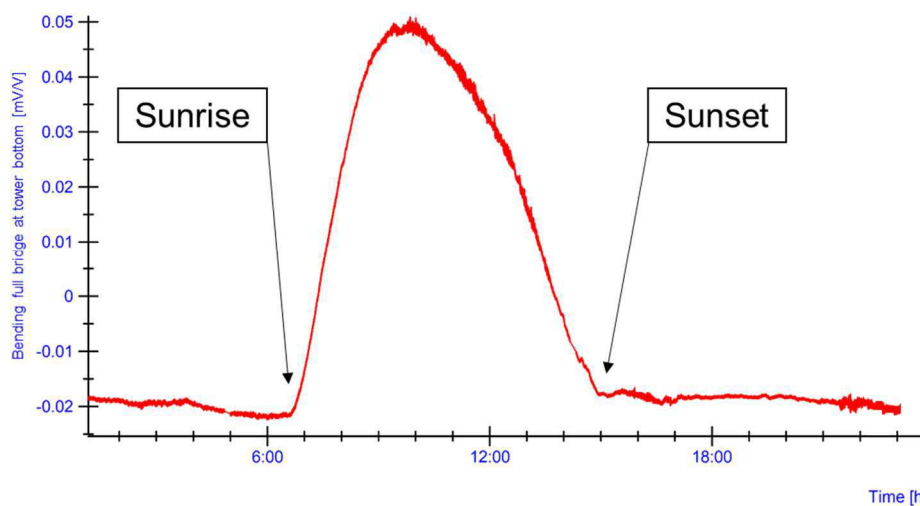
Figure 62 Thermal influence caused by solar radiation on full bending bridge at tower bottom in parallel configuration

MEASUREMENT OF MECHANICAL LOADS IN LARGE WIND TURBINES

Concerning shaft measurements, given that the shaft is rotating, it is possible to assume that the strain gages are isothermal. The parallel configuration should be than preferred, considering that its sensitivity is bigger than a full bridge in T configuration.

Finally, for blade in composite material the parallel bridge configuration should be preferred [159], because due to the anisotropy of the fiberglass, the behaviour under temperature and humidity variation is different along different axes. This makes useless the application of T-rosettes, which will not compensate thermal effects having different value over different direction.

5.5 Temperature compensation – real case application

The electrical output of the bridge depends on the average temperature T_{mean} and the temperature gradients ΔT between the strain gages of the bridge, as described above. A thermal calibration process, able to establish the relationship between the apparent electrical output of the transducer and its operating temperature, would allow thermal compensation. The calibration curve can be obtained either experimentally, as recommended by the standard, or numerically; but in either case the installation of a temperature sensor for each strain gage of the bridge is required.

The calibration curve obtained experimentally requires performing tests for different environmental conditions, i.e. several seasons, several days (e.g. sunny and cloudy) and during different parts of the day, in order to test all possible thermal conditions; therefore, the tests could extend for several days/weeks. The regression line, which interpolates the points of the calibration curve with the method of straight least square, represents the relationship between the thermal phenomenon and the apparent electrical output of the transducer; while the scatter data around the regression line defines the signal uncertainty due to thermal effects.

If a calibration curve cannot be obtained via experimental data, a numerical analysis can be applied. This analysis, based on the apparent thermal stress ε_{sTOT}, estimates the apparent electrical output of the bridge for all operation T_{mean} and ΔT.
For example, Figure 63 shows the apparent electrical voltage calculated in output from a bending strain gage bridge in parallel configuration glued on steel, for different T_{mean} and different ΔT. Where the strain gages used for this analysis are self-compensating for steel with the following characteristics:

1. Temperature coefficient of the material $\alpha_m - \frac{\alpha_r}{k} = 10.8 * 10^{-6} [1/°C]$;
2. Polynomial residual error $\varepsilon_{sR} \pm u_{\varepsilon_{sR}} = -29.65 + 2.86 * T_s - 7.61 * 10^{-2} * T_s^2 + 3.06 * 10^{-4} * T_s^3 \pm (T - 20) * 0.30 + 0.219 * (T_s - 20) [\mu m/m]$;

3. Gauge factor $k \pm u_k = 2.07 \pm 1\%$.
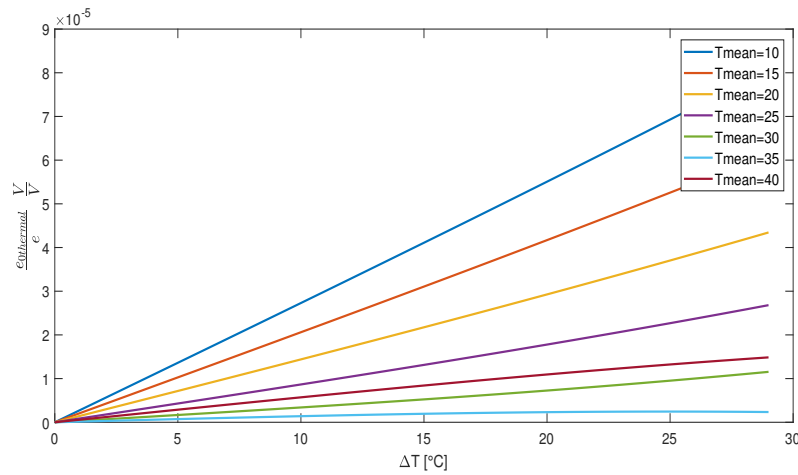
Figure 63 Apparent electric voltage expected in output from a bending strain gage bridge in parallel configuration glued on steel

where:

- $\frac{e_{0thermal}}{e}$: the apparent electric voltage;
- ΔT: the temperature difference between adjacent strain gages of the bridge. For full bending bridge in parallel configuration: $\Delta T = T1 - T2 = T3 - T4$;
- T_{mean}: the mean temperature of the bridge. For full bending bridge in parallel configuration: $T_{mean} = \frac{T1+T2}{2} = \frac{T3+T4}{2}$.

The signal uncertainty associated with thermal compensation by numerical calibration $U_{sig\_M_i}(T)$ is estimated by type B analysis, according to equation (*36*). The terms that create uncertainty are:

1.   Different response of strain gages of the bridge under thermal effects $U_{sig\_M_i-SG}(T)$; in fact even if the four stain gages were coming from the same batch, it is impossible to achieve perfect matching of strain gages. As described above this term will be in the order of $0.15 \frac{\mu V}{V°C}$ and can be estimated, for full bending bridge in parallel configuration, using the equation (*40*):

$$U_{sig_{M_i}-SG}(T)^2 = u_k^2 * \left(\frac{\partial \frac{e_{0thermal}}{e}}{\partial k}\right)^2 + u_{\alpha_r}^2 * \left(\frac{\partial \frac{e_{0thermal}}{e}}{\partial \alpha_r}\right)^2 + u_{\alpha_b}^2 * \left(\frac{\partial \frac{e_{0thermal}}{e}}{\partial \alpha_b}\right)^2 + u_{\alpha_m}^2$$

$$* \left(\frac{\partial \frac{e_{0thermal}}{e}}{\partial \alpha_m}\right)^2 + u_{\varepsilon_{sR13}}^2 * \left(\frac{\partial \frac{e_{0thermal}}{e}}{\partial \varepsilon_{sR13}}\right)^2 + u_{\varepsilon_{sR24}}^2 * \left(\frac{\partial \frac{e_{0thermal}}{e}}{\partial \varepsilon_{sR24}}\right)^2$$

(40)

2.	Uncertainty due to temperature measurement $U_{sig\_M_i-T}(T)$, which in case of full bending bridge in parallel configuration is given by the following equation:

$$U_{sig_{M_i}-T}(T)^2 = u_{T_{13}}{}^2 * \left(\frac{\partial \frac{e_{0thermal}}{e}}{\partial T_{13}}\right)^2 + u_{T_{24}}{}^2 * \left(\frac{\partial \frac{e_{0thermal}}{e}}{\partial T_{24}}\right)^2 + 2\left(\frac{\delta \frac{e_{0thermal}}{e}}{\delta T_{13}}\right)\left(\frac{\delta \frac{e_{0thermal}}{e}}{\delta T_{24}}\right) \quad (41)$$

$$* u(T_{13}, T_{24})$$

where:

- $u_{T_{13}}$ and $u_{T_{24}}$:   variance associated with T_{13} and T_{24} measurement;
- $u(T_{13}, T_{24})$:   covariance of T_{13} and T_{24} measurements.

However the equation (*40*) and (*41*) are a simplified representation, they consider that only one temperature sensor is applied for each pair of strain gauges; a solution often adopted given the proximity between the strain gages of a pair.

The covariance contribution $u(T_{13}, T_{24})$, reported in equation (*41*), defines the degree of correlation between T_{13} and T_{24} measurements and must be considered when they are recorded by simultaneous observations and they have the same [149]:

1. measuring instrument;
2. physical measurement standard;
3. measurement methodology;
4. reference datum (having a significant standard uncertainty).

The covariance computation, according equation (*42*), would require that temperature measurements are repeated h-times in order to build a satisfactory sample.

$$u(T_{13}, T_{24}) = \frac{1}{h(h-1)} \sum_{k=1}^{h} \left(T_{13,k} - \overline{T_{13}}\right)\left(T_{24,k} - \overline{T_{24}}\right) \quad (42)$$

However, since temperature measurements are taken in sequence and may vary in time, it is necessary to compute covariance in real time. This computation can be done through two techniques:

a) by comparing h contemporary thermal measurements from h equivalent sensors arranged in the same measuring point, that it is not really feasible;
b) by comparing h sequential thermal measurements recorded from the same sensor, solution more easy and recommended.

In case the second technique was adopted, a suitable choice of the number of samples must be done in order to obtain a satisfactory result from the covariance analysis. The number of samples should be appropriate for a statistical analysis, i.e.

they must contain all possible measurement errors, but they should not be affected by thermal drifts. For example, Figure 64 and Figure 65 show the comparison between two thermal data sets affected and not affected by thermal drifts; in this case, only the data set shown in Figure 65 can be used for covariance analysis.
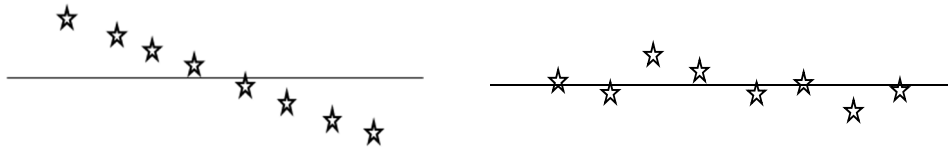
Figure 64 Thermal data influenced by the thermal drift

Figure 65 Thermal data not influenced by the thermal drift

If measurements not affected by thermal drifts are not available, a reduction of covariance estimation error can be achieved through a detrending of the data set with the straight least square interpolation curve.

In order to provide an experimental estimate of covariance in a real case application, a set of T_{13} and T_{24} data was recorded, with a sample frequency of 2 Hz, by resistance temperature detectors mounted near to bending strain gage bridges in parallel configuration located at tower top. The covariance results for one day are shown in Figure 66. Each value of covariance was calculated using 120 samples, equal to 60 s time history.
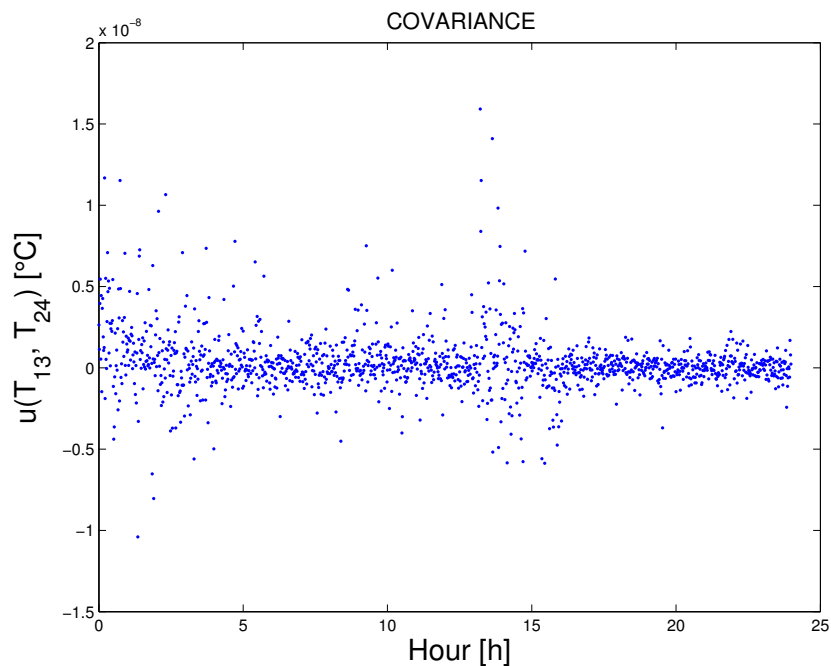
Figure 66 Covariance

The covariance results are approximately equal to $u(T_{13}, T_{24}) = 0.5 * 10^{-8}$. Since, the temperature variance in measurements by resistance temperature detectors is

MEASUREMENT OF MECHANICAL LOADS IN LARGE WIND TURBINES

usually equal to $u_{T_{13}} = u_{T_{24}} = 0.1\ ^{\circ}C$, the covariance contribution may be neglected in the computation of signal uncertainty due to temperature measurement $U_{sig\_M_i-T}(T)$.

In case of a full strain gage bridge in parallel configuration and temperature measurements by thermal resistor, the uncertainty due to temperature measurement is in the order of $U_{sig\_M_i-T}(T) = 0.085\ \frac{\mu V}{V^{\circ}C}$.

Now, the signal uncertainty due to thermal effects for thermal compensation through numerical analysis has to be calculated by combining uncertainty due to different response of strain gages of the bridge under thermal effects and temperature measurement, according to equation (*43*).

$$U_{sig\_M_i}(T)^2 = U_{sig\_M_i-SG}(T)^2 + U_{sig\_M_i-T}(T)^2 \qquad (43)$$

In case of a full strain gage bridge in parallel configuration and temperature measurements by thermal resistor, the signal uncertainty due to thermal effects is in the order of $0.17\ \frac{\mu V}{V^{\circ}C}$. Considering that a typical bridge output at full scale is in the order of 1÷2 *mV/V*, then signal uncertainty due to thermal effects for thermal compensation through numerical analysis account for approximately 0.017 *%/°C*.

6 NON-INTRUSIVE TORQUE MEASUREMENT FOR ROTATING SHAFTS USING OPTICAL SENSING OF ZEBRA-TAPES

Non-intrusive, reliable and precise torque measurement is critical to dynamic performance monitoring, control and condition monitoring of rotating mechanical systems as wind turbine drive train. This chapter presents a novel, contactless torque measurement system consisting of two shaft-mounted zebra tapes and two optical sensors mounted on stationary rigid supports and it is based on a publication [141], now under review, in which the Author has been involved. The Author developed this research after joining the research group at Durham University where the first idea was originated. Unlike conventional torque measurement methods, the proposed system does not require costly embedded sensors or shaft-mounted electronics. Moreover, its non-intrusive nature, adaptable design, simple installation and low cost make it suitable for a large variety of advanced engineering applications. Torque measurement is achieved by estimating the shaft twist angle through analysis of zebra tape pulse train time shifts. This chapter presents and compares two signal processing methods for torque measurement: rising edge detection and cross-correlation. The performance of the proposed system has been proven experimentally under both static and dynamic conditions and both processing approaches show good agreement with reference measurements from an in-line, invasive torque transducer. The uncertainty according to the ISO GUM (Guide to the expression of uncertainty in measurement) standard is shown to be ±0.3% and ±0.8% of full-scale torque for the rising edge and cross-correlation approaches, respectively. A type B estimate of uncertainty is also provided by the Montecarlo method. Finally, a feasibility analysis for two real shaft configurations and real wind turbines has been performed.

6.1 Torque transducer: a general overview

Torque is a fundamental operating parameter of rotating mechanical systems. Some of the most common industrial applications of torque measurement include both conventional [162][163] and emerging [164][131] power generation, electric motor testing [165], robot arms [166], marine [167] and automotive [168] industry. Power and efficiency optimisation based on highly accurate and reliable torque measurement, besides enabling significant energy savings, fits to the steadily increasing requirements of the international regulation, especially for large mechanical drives with high nominal torque [169], such as marine engines [170]. Despite torque measurement and control being critical to dynamic performance monitoring, condition monitoring for predictive maintenance and control of

mechanical systems, reliable measurements can be difficult to obtain in a cost-effective and non-intrusive manner.

The methods used to measure torque can be divided into two categories, either direct or indirect.

Direct methods use in-line torque transducers, usually calibrated by the manufacturer, which are integrated into the drive shaft. These sensors have some susceptibility to noise and require bearings for support, which also implies maintenance. The major obstacle to the industrial application of direct measurement systems is the costly and intrusive nature of the required equipment, which is impractical for short-term use, particularly on large systems. The act of mounting the in-line transducer may also change system dynamics and, consequently, torque values. Moreover, direct measurements cannot be implemented when the rotating mechanical system design does not allow adapting the shaft design or lengthening the drivetrain to accommodate the in-line transducer.

Indirect methods are based on the measurement of torque-related parameters and subsequent torque calculation. These methods have the advantage of avoiding modifications to the original shaft, therefore minimising the impact on mechanical design and not modifying the static and dynamic behaviour of the shaft. The conventional indirect systems are based on measurement of surface strain or angle of twist [151]. Surface strain measurement systems typically use either strain gauges, directly bonded on the shaft body in a Wheatstone bridge configuration, or magnetostrictive methods. These methods rely on the change of resistance [171] or magnetization properties of the material [152], respectively, when torque is applied. Strain gauges are the most commonly used in industrial applications thanks to their low cost and high sensitivity. However, the main limitations of this method are the complexity of installation of the sensors on cylindrical surfaces, the need to install electronics on the rotating shaft, the requirement for specialised personnel required for installation, usability, resolution, noise susceptibility and the requirement for regular calibration. Moreover, unwanted forces can create unintended directional disturbance, such as crosstalk phenomena, and local stress concentration that can increase the uncertainty in the measured loads and reduce accuracy [152]. Angle of twist measurement methods are based on the measurement of the phase shift between two points on the shaft, separated by a suitable distance, through magnetic or optical angular position sensing [168]. The first use toothed gears which are angularly displaced with respect to each other as the shaft shift twist angle increases, thereby increasing the electrical phase difference between the signals measured by magnetic pickups [152]. Conventional optical methods use slotted discs which move with respect to each other as torque

is applied, thereby changing the on-times of light pulses created by the shutter actions of the rotating discs [172][173]. Both systems can be retrofitted to existing systems and do not have the inherent complexity of strain gauge installations. However, they require the installation of quite large rings and plates around the shaft which can be impractical in some industrial applications, such as in-vehicle and mobile measurements, due to space constraints. They also suffer from environmental factors such as dust, humidity, temperature, vibration, electromagnetic interference and aging. In addition to performance limitations, these methods usually suffer from low range-to-resolution ratio [151]. A laser torquemeter was first presented in [174] and later analysed in [175][176][177]. This instrument is based on the cross-correlation of the periodic speckle patterns generated by two axially separated laser beams on a rotating shaft, having known mechanical proprieties. Even if this is a smart non-contact approach, it suffers from decorrelation of speckle patterns due to shaft displacement and tilt, making its practical application difficult. Several advanced contactless torque measurements techniques have been researched recently, such as the photo-elastic torque sensor based on the birefringence effect of optically anisotropic materials [178] and the non-contact Hall effect design sensor [142]. However, most of these sensors have significant limitations such as requiring sensitive materials to be attached on the shaft surface, such as ferromagnetic and piezoelectric materials, and limited speed range and resolution. Moreover, very few solutions can provide both shaft torque and speed measurement from the same sensor, which is useful whenever one desires to measure mechanical power.

This paper presents a novel and simple contactless torque and speed measurement system consisting of two zebra tape codes directly glued around the shaft with two optical sensors mounted on non-rotating supports. This technique operates entirely contact-free and allows torque measurement on standard installations, across their operational life, avoiding the use of permanently installed in-line intrusive torque meters, by simply instrumenting the existing shaft with the two zebra tapes located as far as possible from each other. The use of optical sensors and zebra tapes on rotating shafts is not new; however literature reports only application for torsional vibration measurement [142][143], while this research proposes their use for torque measurement. This paper introduces the operating principle of the proposed non-intrusive torque measurement system and its experimental implementation and validation. Two different approaches for processing the optical probe pulse train signals and estimating the shaft twist, and hence the applied torque, are then presented. After calibrating the system under stationary conditions, its response and performance under both static and dynamic torque conditions is demonstrated by comparing the results of the two proposed

signal processing approaches against the reference measurements from an in-line torque transducer mounted on the test bench shaft.

6.2 Methodological approach

A torque acting on a shaft causes the shaft itself to twist, with one end rotating with respect to the other by an angle displacement θ_r. Assuming a uniform circular cross-section and linear homogenous elastic material, the relationship between the torque applied to a rotating shaft, T_{rotor} [Nm], and the relative rotation of the ends of the shaft section, θ_r [rad], is described [180] by:

$$T_{rotor} = I_s \ddot{\theta}_r + C \dot{\theta}_r + K \theta_r \tag{44}$$

where I_s is the rotating system moment of inertia [kgm^2], C is the shaft damping coefficient [$kgm^2 s^{-1} rad^{-1}$] and K is the shaft torsional stiffness [Nm/rad].

The non-intrusive torque measurement system proposed in this thess employs a set of two zebra tapes and two optical probes, one at each end of the shaft, as shown in Figure 67.
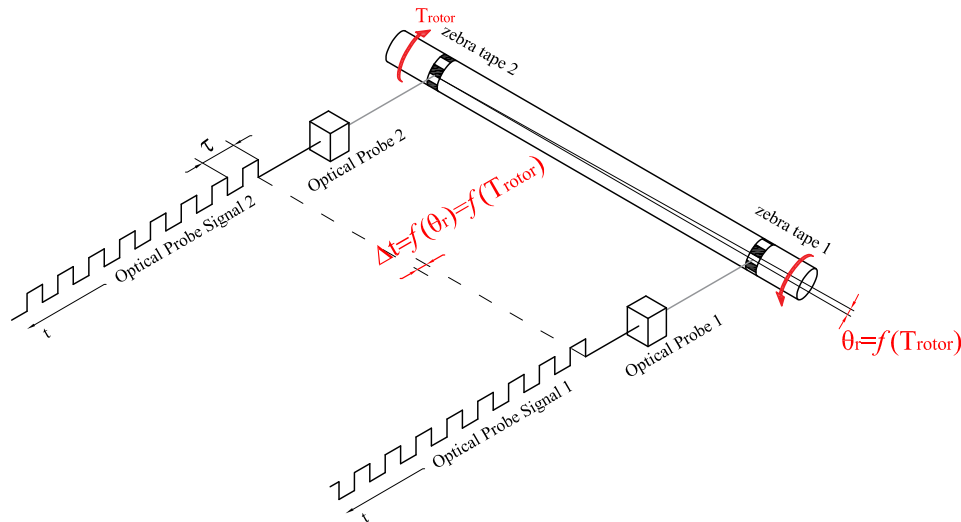
Figure 67 Operating principle of the non-intrusive torque measurement system

The zebra tapes feature an equal number of equidistant black and white stripes and are glued around the shaft. As the shaft rotates, each optical sensor, mounted on a non-rotating component, generates a pulse train signal proportional to the light intensity reflected by the zebra tape stripes. When a torque, T_{rotor}, is applied to the shaft, the relative rotation of the ends of the shaft section, θ_r, results in a time shift, Δt, between the two pulse train signals. The principle of the proposed method is to quantify the shaft relative twist angle by measuring the phase difference between

the two pulse signals and thence deriving the applied torque, from a known torque-twist relationship. This is achieved according to the following procedure:

Estimation of the time shift, Δt [s], between the pulse trains measured by the two optical probes;

Measurement of the pulse trains period, $\tau [s]$, and calculation of the shaft rotational speed, n [rpm]:

$$n = \frac{60}{\tau\ ppr} \tag{45}$$

where ppr is the number of pulses per shaft revolution;

Conversion of time shift to absolute angular shift, ϑ_a, according to [181]:

$$\theta_a = \frac{2\pi}{60} n \Delta t \tag{46}$$

The shaft absolute twist angle, ϑ_a, could be different to the shaft relative twist angle, θ_r, due to the mounting misalignment between the two optical probes and/or the two zebra tapes. This error manifests itself as an apparent angular shift, $\vartheta_{a,0}$, at the no load condition;

Calculation of the shaft relative twist angle, θ_r, according to the following equation:

$$\theta_r = \theta_a - \theta_{a,0} \tag{47}$$

Estimation of the shaft torque based on the known calibration curve, that is the relationship between the shaft relative twist angle θ_r and torque T_{rotor} for a given shaft and material.

One of the main advantages of this approach is that it allows the measurement of a wide torque range by carefully designing the zebra tapes and their distance along the shaft. This makes it suitable for a large variety of engineering applications.

6.3   Experimental Set-up

Experiments were performed to calibrate and validate the proposed non-intrusive torque measurement system. The calibration has been performed by comparing the zebra tape torque meter with a reference state-of-art measurement technique; in particular, we have used an industrial in-line torque meter based on the principle of a variable, torque-proportional transformer coupling. This technology is robust against electromagnetic interference and temperature effects; therefore, the system can be effectively used as a reference for calibration. Figure 68 provides a schematic of the torque test rig developed at Durham University, in collaboration

with Università Politecnica delle Marche. Figure 69 shows the implemented test stand with its main components and instrumentation.

The test rig comprises a 4-pole 4 kW grid-connected induction generator driven by a 4-pole 4 kW induction motor controlling the speed profile. Both machines are manufactured by ABB Motors. The motor shaft speed is varied via an inverter drive up to 2100 rpm. The generator is connected to a variable transformer to vary its stator voltage and hence the shaft torque in the range from 0 to 16 Nm.

The main rig solid shaft, shown schematically in Figure 70, features a reduced diameter cross-section in its central part for experimental purposes in order to enhance sensitivity with respect to the test rig torque range and hence achieve a higher twist angle θ_r for the same applied torque. Indeed, this allows angular shifts of the same order of magnitude as would be observed in the case of larger torques applied to larger diameter shafts in industrial applications, despite the limitations of the maximum torque possible using this test rig.
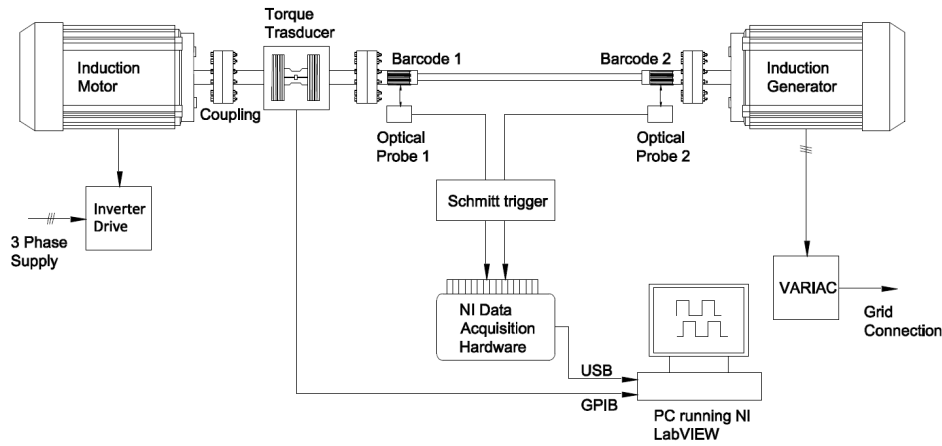
Figure 68 Schematic diagram of the torque test rig

Figure 69 Main components and instrumentation of the torque test rig

A high-quality, laser-printed zebra tape is glued around each end of the shaft. The passage of the alternating light and dark stripes is measured by two Optek

OPB739RWZ reflective line reader sensors placed at the optimum distance of 0.76 mm from the target, as shown in Figure 71.
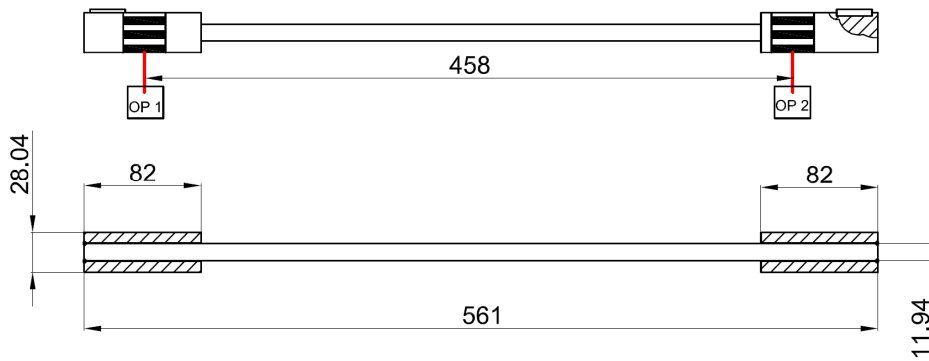
Figure 70 Solid shaft layout and location of the two zebra tapes
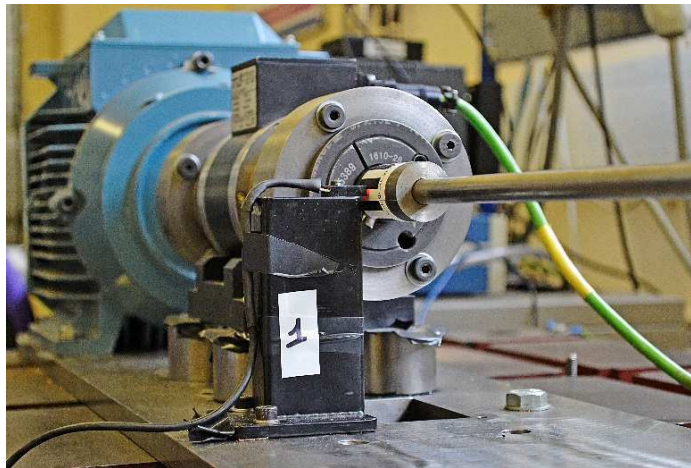
Figure 71 Detail of the contactless shaft torque measurement system

First, the output from the two optical probes is transformed into a series of square pulses through a Schmitt trigger. The pulses are then acquired by a National Instruments (NI) 16-bit data acquisition system (USB-6211 DAQ) driven by the LabVIEW data acquisition environment. The sampling frequency, f_{OP}, is set at 125 kHz, the maximum possible for the NI USB-6211 DAQ hardware.

An in-line Magtrol TMB 313/431 torque transducer, with a rated torque of 500 Nm and a combined error of linearity and hysteresis less than ±0.15% of the rated torque, acts as a reference for calibration and comparison with the optical non-intrusive system output. The transducer is capable of outputting 60 pulses per revolution for speed measurement, so it is also used as a reference tachometer. The torque transducer output is collected through a Magtrol 6400 torque display

which is connected by a GPIB/IEEE-488 interface to the LabVIEW data acquisition environment. The time synchronisation between the torque transducer and the optical probes' readings is obtained by comparing the Unix timestamp of the two system acquisitions.

6.3.1 Zebra tape design

The design of the zebra tape, particularly the number of pulses per revolution, has a significant impact on the precision of the torque measurements [182]. For a given shaft and zebra tape design, the maximum measurable phase difference between two pulse signals is given by half the zebra tape period, that is half the length of each of its black-white segments, corresponding to 180° phase shift. Indeed, any twist larger than half the period of the zebra tape would be confused with a lower one, as always happens in periodic signals.

When designing the zebra tapes, the minimum zebra tape period, P_{min} [m], can be calculated as a function of the maximum torsion angle of the shaft expected during operation, θ_{max}:

$$P_{min} > 2\theta_{max}\, r \tag{48}$$

where $\theta_{max,}$ [rad] is given by:

$$\theta_{max} = \frac{T_{rotor-max}L}{J_s G} \tag{49}$$

where $T_{rotor-max}$ is the maximum torque expected during operation [Nm], L is the distance between the two optical probes [m], J_s is the shaft polar moment of inertia [m^4] and G is the shear modulus of elasticity for the shaft material [Pa]. The corresponding zebra tape maximum allowable number of pulses per revolution, ppr_{max}, can then be calculated as:

$$ppr_{max} = int\left(\frac{2\pi r}{P_{min}}\right) < \frac{2\pi r}{2\theta_{max}\, r} \tag{50}$$

where r [m] is the shaft radius and int the integer part function.

In the case of the experimental test bench described in this work, given the shaft geometry and the maximum torque achievable during operation (16 Nm) equation (50) provides a maximum allowable number of pulses per revolution of 45. Within this constraint, the choice of the zebra tape design is a key factor influencing the performance of the proposed torque measurement system. The larger the number of pulses per revolution, the larger the samples required per revolution, that is the larger the sample frequency of the proposed torque transducer, but the more the computational cost needed to implement the data processing. For the purpose of

NON-INTRUSIVE TORQUE MEASUREMENT

this work, the test bench shaft was instrumented with two bar codes featuring 8 equal stripe pairs, with a stripe width of 5.5 mm, fitting exactly around the shaft. The selection of 8 pulses per revolution represents a trade-off between uncertainty and computational cost. The zebra tape design was selected so that the resulting pulses have a 50% duty cycle which makes phase shift measurement processing easier.

Table 18 summarises the features of the zebra tapes used in the test bench.

Symbol	Description	Value
P	Zebra tape period (length of each black-white segment)	11.0 mm
ppr	Number of pulses per revolution	8
θ_{full_scale}	Maximum measurable shaft torsion angle	$\dfrac{\pi}{8}$

Table 18 Features of the experimental zebra tape.

6.3.2 Optical sensor output

Figure 72.a shows how the zebra tape passage determines the sensor output. The optical probe emits an unfocussed beam which lights the zebra tape surface. An unfocussed optical probe has been chosen because it allows for variations of sensor to shaft distance over a larger depth of field with respect to focused probes. However, it produces pulses with lower rising and falling edge gradients, with respect to focused probes. Scattered light is collected back through a detector with a certain angle of aperture. Light scattering intensity from the white surface is significantly larger than that from the black surface. Therefore, even if the zebra tape surface has a step profile (Figure 72.b), the scattered light intensity changes continuously from low to high during the passage of the white stripe. The change in the radiation reflected to the detector is not abrupt, but undergoes a gradual transition along a switching distance X_T (Figure 72.c) [183]. The optical probe (OP) voltage output results from this gradual change in scattered light intensity due to the motion of the black-white stripe through the illuminated area (called trip effect) and the first order dynamic response of the photodetector (Figure 72.d). A Schmitt trigger is implemented to square the probe output voltage when it crosses a pre-set threshold, S_L (Figure 72.e), and to convert it into a train of constant amplitude pulses. The photodetector signal is squared to produce pulses with almost vertical rising and falling edges, easing timing and analysis.

This train of square pulses will be phase shifted by torque variations, as described earlier. In case of variation of the distance between the shaft and the optical probes, the amplitude of the output voltage from the photodetectors will vary, resulting in an amplitude modulated signal. This would affect the train of pulses

from the Schmidt trigger, which operates on a fixed threshold. The effects of this source of uncertainty will be discussed later in the paper.
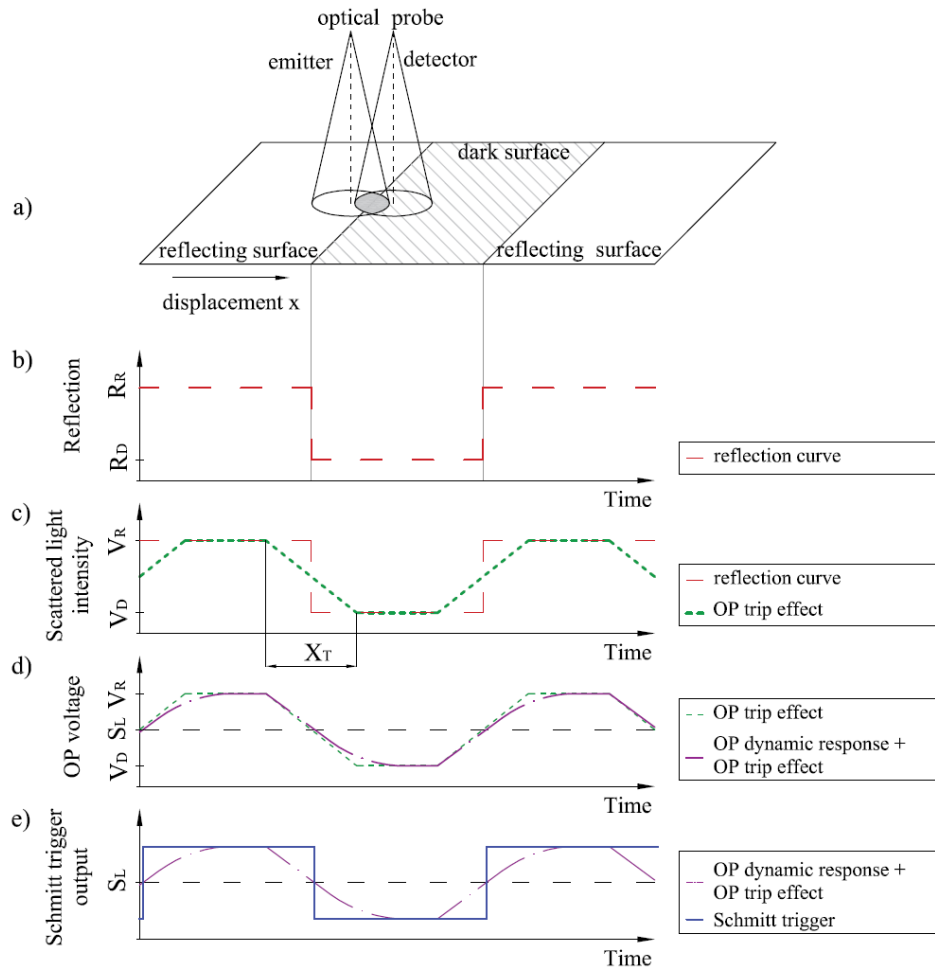
Figure 72 Optical probe response to zebra tape

6.3.3 Data processing

6.3.3.a Signal pre-processing

In order to automatically extract the values of the shaft angular shifts from the two zebra tape optical signals, dedicated programmes, known as Virtual Instruments (VIs), were developed and built in the LabVIEW environment. Figure 73 shows the data processing flow chart of the VIs implemented for pulse train analysis.
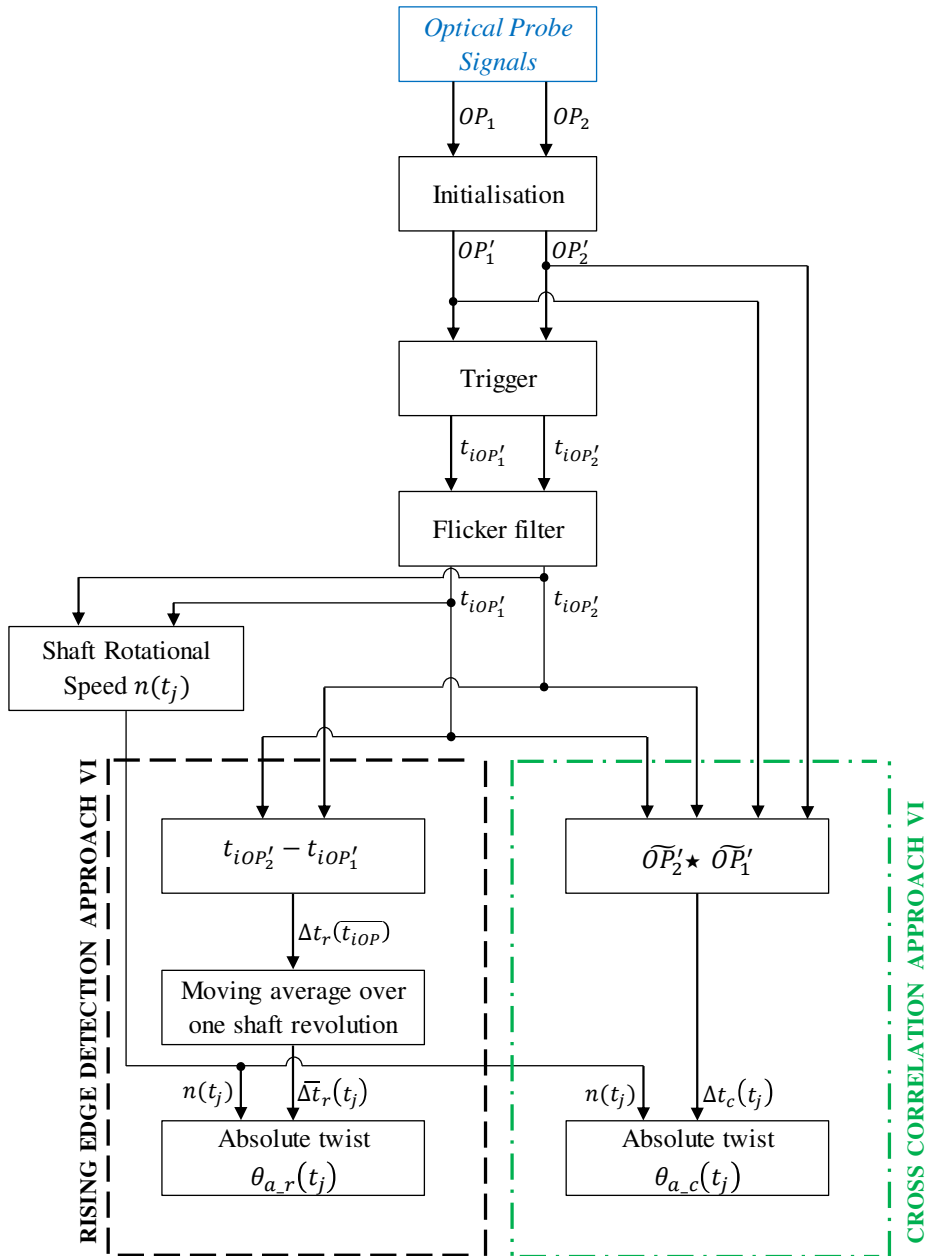
Figure 73 Data processing flow diagram

The data processing consists of two steps:

1) The shaft rotational speed is calculated by estimating the time per shaft revolution from the rising edges of the two pulse trains;

2) The shaft absolute twist is calculated by adopting the rising edge detection and the cross-correlation approaches.

Optical probe installation and zebra tape mounting offset could cause initial misalignment of the pulse trains at the start of recording with a consequent erroneous estimation of the initial time shift, and hence angular shift. To overcome this problem, the signals recorded by the optical probes are first initialised when the data system acquisition is started. Figure 74.a-b shows an example of two pairs of similar pulse trains; they feature the same time shift, Δt_r, however their recording starts at two different positions with respect to the pulses. The time shift measured between their first two rising edges will be different, Δt_{r_a} and Δt_{r_b}, respectively. In order to avoid this error in the measurements, the optical probe signals, OP_1 and OP_2, are initialised by forcing the recording to start only when both signals are in the high or low state, i.e. at the instant t_p in Figure 74.c-d. Now, the same time shift, Δt_r, is measured based on the time between the first rising edges of the initialised signals, OP'_1 and OP'_2.
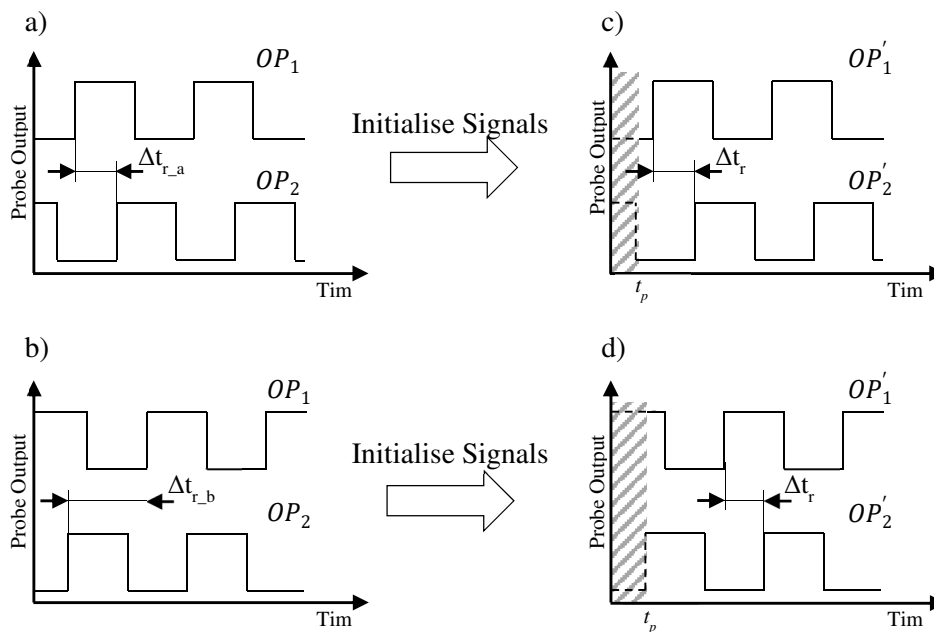
Figure 74 Signal initialisation

The time at which the rising edges of the two initialized signals occur is defined as $t_{iOP'_k}$, where i = 1,2, ...m, with m equal to the number of rising edges in the initialized signals, and k = 1,2 is the index that identifies the two optical probes. The rising edge time instants $t_{iOP'_k}$ are captured by triggered acquisition where the threshold level is set equal to half of the peak-to-peak signal amplitude. A flicker filter is also applied to remove rising edge timing errors resulting from possible signal flickering around the trigger level. Flickering would result in more than one output from the

NON-INTRUSIVE TORQUE MEASUREMENT

trigger block for each signal rising edge, i.e. $t_{2OP'_k}$ and $t^*_{2OP'_k}$ in Figure 75. For each pulse train, the filter compares the time interval between two consecutive rising edges against that estimated from the expected shaft rotational speed, 1500-1900 rpm, and the number of pulses per revolution, 8. When the two values do not match, the filter acts on the signal to keep only the first output from the trigger block and remove all other unwanted outputs, that is $t^*_{2OP'_k}$ in Figure 75. For each signal, the output of the flicker filter is a one-dimensional array containing *m* elements representing the rising edge times of the train of pulses.
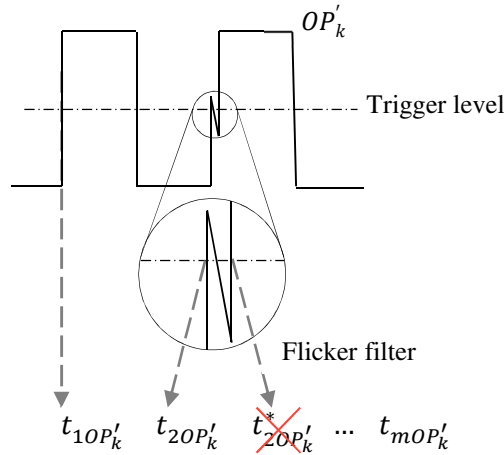
Figure 75 Flicker filter

6.3.3.b   Shaft rotational speed

For each zebra tape, the identified rising edge times, $t_{iOP'_k}$, where *k* = 1,2, are then used to estimate the corresponding shaft speed, $n_k(t_{k,j})$ [*rpm*], by applying conventional speed encoder techniques, according to equation (46), as follows:

$$n_k(t_{k,j}) = \frac{60}{t_{(ppr+l-1)OP'_k} - t_{lOP'_k}} \qquad (51)$$

where *l* = 1,2,..,(m-ppr) and $t_{k,j}$ is the mean time of the windows $t_{(ppr+l-1)OP'_k} - t_{lOP'_k}$, calculated as:

$$t_{k,j} = \frac{\sum_{n=j+1-\left|\frac{ppr}{2}\right|_{up}}^{j+\left|\frac{ppr}{2}\right|_{down}} t_{nOP'_k}}{ppr} \qquad (52)$$

where $j = \left(\left|\frac{ppr}{2}\right|_{up}\right), ..., \left(m - \left|\frac{ppr}{2}\right|_{down}\right)$, with $\left|\frac{ppr}{2}\right|_{up}$ and $\left|\frac{ppr}{2}\right|_{down}$ equal to half of *ppr* rounded up and down, respectively.

The shaft rotational speed, $n(t_j)$, is then calculated as the average of those two speeds to minimise the error:

$$n(t_j) = \frac{n_1(t_{1,j}) + n_2(t_{2,j})}{2} \qquad (53)$$

where t_j is given by:

$$t_j = \frac{t_{1,j} + t_{2,j}}{2} \qquad (54)$$

6.3.3.c   Shaft absolute twist

6.3.3.c.1   Time shift measurement by direct timing of rising edges

The rising edge detection approach is the most straightforward method for determining the time delay between the pulses. It is based on the measurement of the times at which the rising edges of the two pulse trains occur and on the calculation of their relative phase shift, as shown in Figure 76. In the rising edge detection approach VI, the time shift between the two pulse trains associated with the signals' average rising edge times, $\Delta t_r(\overline{t_{\iota OP'}})$, is calculated as:

$$\Delta t_r(\overline{t_{\iota OP'}}) = t_{iOP'_2} - t_{iOP'_1} \qquad (55)$$

where *i* = 1,….., *m* and $\overline{t_{\iota OP'}}$ is defined as:

$$\overline{t_{\iota OP'}} = \frac{t_{iOP'_1} + t_{iOP'_2}}{2} \qquad (56)$$

As already pointed out, tangential and radial displacements between shaft and optical probes, typically caused by vibrations or shaft deformation, introduce noise in timing of pulses. This noise is expected to be periodic, at the rotational frequency or its harmonics. Therefore, a moving average filter is implemented to measure a time delay averaged over a full revolution $\overline{\Delta t}_r(t_j)$. This is implemented as moving average filter over the eight delays $\Delta t_r(\overline{t_{\iota OP'}})$ measured during a full revolution, with seven-point overlap over time, allowing the calculation of an averaged delay for each pulse, that is one value per zebra tape pulse.

The eight-point averaged time shift, $\overline{\Delta t}_r(t_j)$, is calculated as:

$$\overline{\Delta t}_r(t_j) = \sum_{i=j+1-\left|\frac{ppr}{2}\right|_{up}}^{j+\left|\frac{ppr}{2}\right|_{down}} \frac{\Delta t_r(\overline{t_{\iota OP'}})}{ppr} \qquad (57)$$

NON-INTRUSIVE TORQUE MEASUREMENT
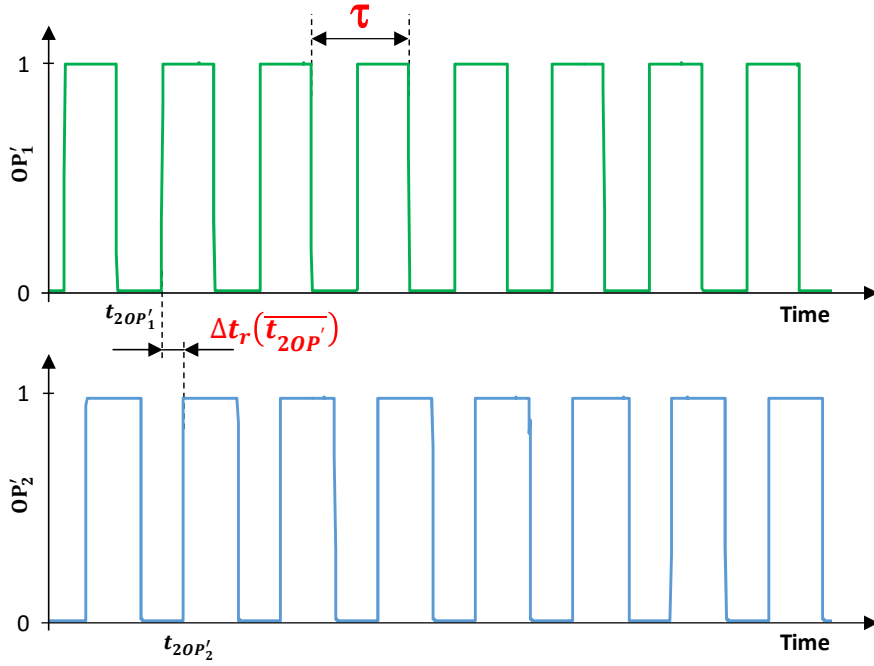
Figure 76 Phase shift estimation through the rising edge detection approach

6.3.3.c.2   *Time shift measurement by cross-correlation*

The cross-correlation approach allows the measurement of the similarity of the two time series, OP_1' and OP_2', as a function of the time-lag applied to one of them. Unlike the rising edge detection approach, the cross-correlation VI uses the full initialised signals OP_1' and OP_2' to estimate their time shift and not only the times at which the rising edges occur (Figure 77).
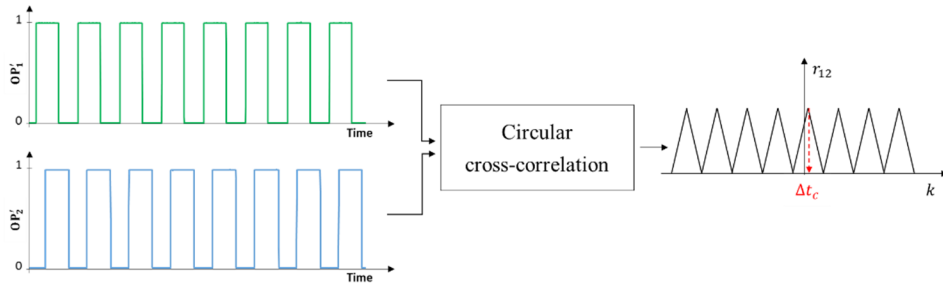
Figure 77 Phase shift estimation through the cross-correlation approach

Cross-correlation is implemented according to [21], as circular cross-correlation, defined as:

$$r_{12}(k) = \frac{1}{N}\sum_{n=0}^{N-1} OP_1'(n)\, OP_2'(k-n) \qquad (58)$$

where $k = 0,…$, N-1 and N, the length of the two signals, is chosen equal to the shaft revolution. This algorithm does not require zero padding, but considers the pulse train to be periodic.

Circular cross-correlation provides an output with 8 peaks, equal to the number of pulses per revolution (Figure 77), that correspond to 8 possible time delays, as usual in a periodic function. The delay of interest is the smallest one, Δt_c, provided that the zebra tape period is larger than the maximum shift, as discussed in Paragraph 6.3.1, equation (48). The other peaks appear because the train of pulses is a periodic function.

The signals OP_1' and OP_2' are progressively circular cross-correlated giving one value of the time shift per zebra tape pulse, $\Delta t_c(t_j)$, similarly to the case of the rising edge detection approach $\overline{\Delta t}_r(t_j)$.

In both approaches, the calculated time shifts, $\overline{\Delta t}_r(t_j)$ and $\Delta t_c(t_j)$, respectively, depend on the shaft speed. According to equation (47), they are converted into shaft absolute angular shifts, $\theta_{a\_r}(t_j)$ and $\theta_{a\_c}(t_j)$, respectively,

$$\theta_{a\_r}(t_j) = \frac{2\pi}{60} n(t_j) \overline{\Delta t}_r(t_j) \tag{59}$$

$$\theta_{a\_c}(t_j) = \frac{2\pi}{60} n(t_j) \Delta t_c(t_j) \tag{60}$$

6.3.4   Range, resolution and sampling frequency

For a given zebra tape design (ppr), shaft speed (n) and optical probe sampling frequency (f_{OP}), the non-intrusive torque measurement system features are:

Range: $\qquad \theta_{RANGE} = [-\theta_{full\_scale} \div \theta_{full\_scale}] = \left[-\frac{\pi}{ppr} \div \frac{\pi}{ppr}\right]$ $\quad$ (61)

Resolution: $\qquad\qquad\qquad\qquad \delta\theta_r = \frac{2\pi n}{60} * \frac{1}{f_{OP}}$ $\qquad\qquad$ (62)

Using the calibration curve $\theta_r = m_{T_{rotor}} * T_{rotor}$, equations (61) and (62) allow the estimation of the corresponding torque range and resolution.

$$T_{rotor\_RANGE} = \frac{\theta_{RANGE}}{m_{T_{rotor}}} \tag{63}$$

$$\delta T_{rotor} = \frac{\delta\theta_r}{m_{T_{rotor}}} \tag{64}$$

NON-INTRUSIVE TORQUE MEASUREMENT

$$f_c = \frac{2\pi n}{60} * \frac{ppr}{2\pi} = \frac{n * ppr}{60} \qquad (65)$$

Torque samples are then obtained at a non-constant frequency which is dependent on the shaft speed.

6.4 Results

6.4.1 System calibration

The non-contact optical torque system was calibrated against reference torque measurements from the in-line torque transducer in order to fully characterise the torque-twist angle relationship described by equation (44). The calibration curve allows the estimation of the torque acting along the shaft by simply recording the zebra tape pulse trains, calculating their time shift and hence the shaft angular shift, using either method.

Steady state tests were performed on the test rig at four different shaft speeds: 1600, 1700, 1800 and 1900 rpm. For each speed, the calibration procedure consisted of the following steps:

1) Run the motor to the required testing speed.
2) Record the signals from both the optical probes and the torque transducer at no-load (0 volts applied to the generator stator) for around 10 s.
3) Vary the generator stator voltage to increase the shaft torque in steps of 2 Nm, starting from an initial torque value of 1 Nm in the case of the tests run at 1600 and 1800 rpm and 2 Nm in the case of the tests run at 1700 and 1900 rpm. For each speed, to avoid damage to the generator during operation, the stator voltage was varied up to a precautionary safety limit of its armature winding current of 8 amps; this determined the maximum operational torque. Given the available experimental set-up, the calibration range was limited to 16 Nm, even though the zebra tape had been designed with a period allowing measurements up to 62 Nm, which therefore represents its full-scale input range.
4) Record the signals from both the optical probes and the torque transducer for around 10 seconds for each applied torque level.
5) Post-process the optical probe pulse data and calculate the shaft twist using the rising edge detection and cross-correlation approaches presented in section 3.3.
6) Build calibration curves by plotting the shaft relative twist, calculated according to equation (45), against the corresponding reference torque measured by the in-line transducer, whose signal was resampled to match the time delay sampling frequency.

The calibration curves resulting from the rising edge and the cross-correlation approaches are shown in Figure 78 and Figure 79, respectively, and compared in Table 19. They result from the linear regression of experimental data by a straight line using the least square method.
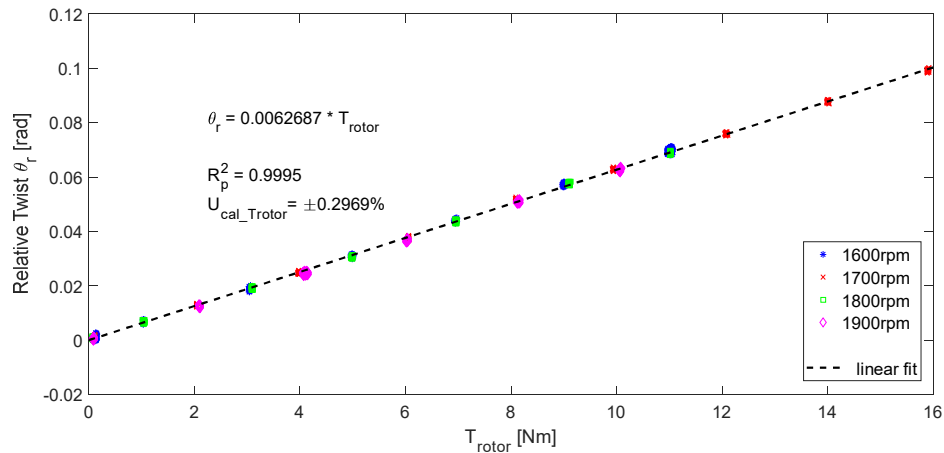
Figure 78 Calibration curve: Rising edge detection approach
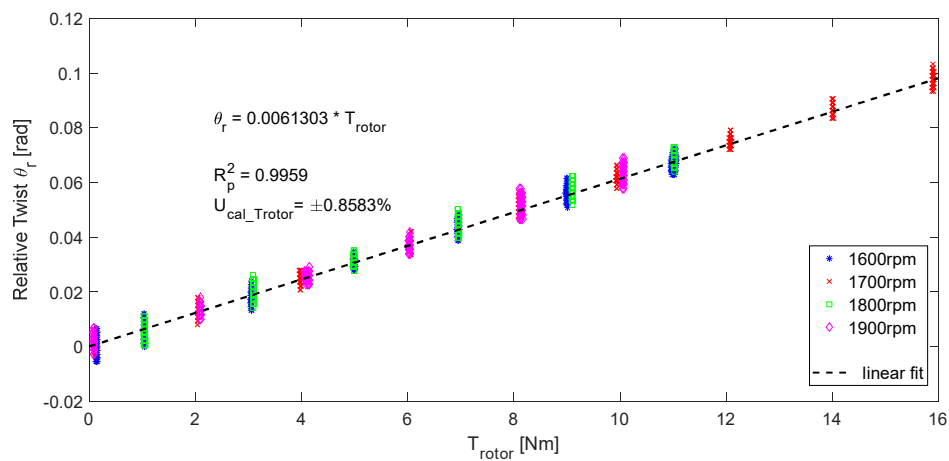
Figure 79 Calibration curve: Cross-correlation approach

As predicted by equation (44), the torque-twist trend is linear under steady state conditions. The two calibration curves show a similar trend with satisfactory R-squared levels, indicating a good fit of the experimental data by the regression line. A difference in sensitivity of around 2% is observed.

6.4.2 Measurement Uncertainty Evaluation

The measurement uncertainty has been estimated according to the ISO GUM (Guide to the expression of uncertainty in measurement); in particular, the statistical processing of series of experimental data have allowed a Type A estimate of uncertainty obtained in the laboratory conditions of the test set-up used in this work, while a more comprehensive Type B analysis has been performed by a Montecarlo method, which allows to estimate measurement uncertainty taking into account a number of influencing parameters and disturbances which could affect the measurement system in a real world application.

6.4.2.a Type A uncertainty

The regression of calibration data has allowed the statistical estimation of the Type A uncertainty of measurement, $U_{cal\_T_{rotor}}$, according to the GUM:1995 [157] (Table 19). For each case, the standard deviation of the input torque, $s_{T_{rotor}}$, has been estimated by statistical analysis of the residuals of the *N* calibration data with respect to their interpolating line as:

$$s_{T_{rotor}} = \sqrt{\frac{1}{N-2} \sum_{k=1}^{N} \left(\frac{\theta_{r_k}}{m_{T_{rotor}}} - T_{rotor_k} \right)^2} \tag{66}$$

where θ_r is the shaft relative twist predicted by the calibration line and *m* is the calibration line slope. The type A uncertainty $U_{cal\_T_{rotor}}$ associated to each approach has then been calculated, in compliance with the ISO GUM:1995 [157], as expanded uncertainty with a coverage factor $k_p = 2$, allowing for a 95% confidence level, as:

$$U_{cal\_T_{rotor}}[\text{Nm}] = k_p \, s_{T_{rotor}} \tag{67}$$

and expressed as a percentage of the measurement system full scale torque, $T_{rotor-max}$, as:

$$U_{cal\_T_{rotor}}[\%] = \frac{U_{cal\_T_{rotor}}[\text{Nm}]}{T_{rotor-max}[\text{Nm}]} 100 \tag{68}$$

where:

$$T_{rotor-max} = \frac{\theta_{full\_scale}}{m_{T_{rotor}}} \tag{69}$$

and θ_{full_scale} is the measurement system full scale twist output given in Table 18.

All this analysis on type A uncertainty takes into account repeated experiments at various speed, various torque which were performed during and repeated during several days and with different operators. This provides information on repeatability and reproducibility of the proposed method.

For the experimental set-up used in this work, the maximum measurable angular shift of the system corresponds to a full-scale input torque of $T_{RANGE} = 62\ Nm$, which is approximately four times larger than the calibration range. Within this range the system has a resolution $\delta T_{rotor} = \frac{\delta\theta_r}{m_{T_{rotor}}} = 0.27\ Nm$ if only one rising edge is used; however, resolution decreases by *ppr* if the angular shift is determined by averaging a series of ppr angular shifts θ_r. In our case we used *ppr=8*.

Unexpectedly, the cross-correlation approach results show a higher dispersion around their best fit curve when compared to the rising edge detection approach, resulting in higher uncertainty of the method (Table 19).

Method	Linear Fit Equation	R^2_{-p}	$U_{cal\_T_{rotor}}[\%]$
Rising Edge	θ_r = 6.27 10^{-3}*T$_{rotor}$	0.999	±0.3
Cross-Correlation	θ_r = 6.13 10^{-3}*T$_{rotor}$	0.995	±0.8

Table 19 Parameters of the two calibration curves and relative Type A uncertainty, $U_{cal\_T_{rotor}}$

Cross-correlation underperforms with respect to direct timing because of the changes in duty cycle throughout one shaft revolution and the time shift introduced by the Schmidt trigger operating on an amplitude modulated photodetector signal. As mentioned, amplitude modulation may affect the optical signal because of possible vibrations, shaft misalignment or bending; all these phenomena would affect the sensor to shaft distance during shaft rotation. In these conditions, after the Schmidt trigger, the variation of duty cycle and time shift causes a displacement of the pulse centre equal to $\delta_d = (\delta t_r + \delta t_f)/2$, as shown in Figure 80.

Cross-correlation is more sensitive to pulse shape than rising edge timing. Moreover, cross-correlation is intrinsically sensitive to the position of the centre of each square pulse. These effects together explain the larger dispersion of data seen for cross-correlation whenever the optical signal experiences amplitude modulation and a Schmidt trigger is applied. It would therefore be expected that cross-correlation would better perform on the original photodetector signal, before being squared by the Schmidt, but this has not been implemented in this paper.

NON-INTRUSIVE TORQUE MEASUREMENT
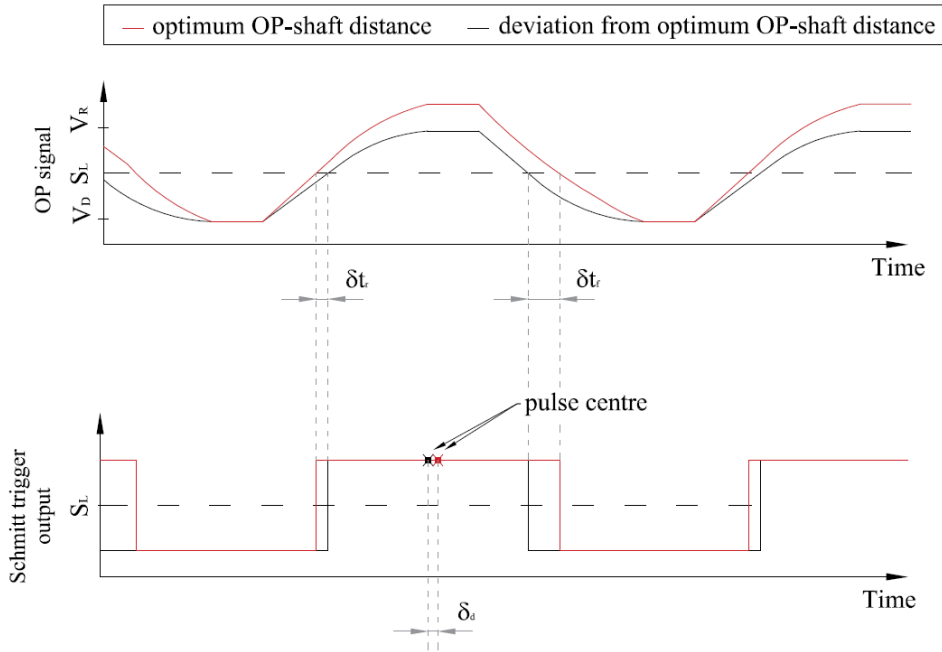
Figure 80 Effect of sensor to shaft distance variation on the optical probe output

6.4.2.b   Uncertainty analysis using Monte Carlo Method (MCM)

The propagation of distributions through a mathematical model of the zebra tape torque meter system has been implemented by MCM for the evaluation of uncertainty of measurement according to the GUM:1995 Supplement 1 [184]. The measurement uncertainty evaluation has been performed with respect to the shaft rotational speed of 1700 rpm at which the maximum torque achievable during operation was measured.

A mathematical model of the zebra tape torque meter, shown schematically in Figure 84, has been built to relate the output quantity T_{rotor} (i.e. the quantity intended to be measured) with the input quantities $\textbf{\textit{X}}$ (i.e. K, n and Δt) upon which T_{rotor} depends. Table 20 summarises the model equations for the two approaches.
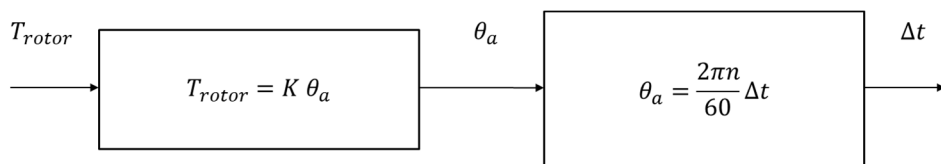
Figure 81. Zebra tape torque meter model.

Method	Model
Rising Edge	$T_{rotor} = K \dfrac{2\pi n}{60} \overline{\Delta t_r}$
Cross-Correlation	$T_{rotor} = K \dfrac{2\pi n}{60} \Delta t_c$

Table 20 Measurement system model equations.

The shaft torsional stiffness, *K*, has been estimated as the inverse of the slope of the rising edge calibration linear fit equation and its standard deviation, s_K, has been computed by Type A method according to the GUM [157], i.e. by performing a statistical analysis of the residuals of the *M* calibration data with respect to its inverse interpolating line $T_{rotor} = K\theta_r$ as:

$$s_{\mathrm{K}} = \sqrt{\dfrac{N s_{T_{rotor}}^2}{N \sum_{j=1}^{N} \theta_{r_j}^2 - \left(\sum_{j=1}^{N} \theta_{r_j}\right)^2}} \qquad (70)$$

The uncertainty of the shaft angular speed *n* is computed by Type A method, by performing a statistical analysis of the time series of experimental data from the torque test rig at steady state, according to the GUM [157]. The standard uncertainty s_n is therefore computed as standard deviation of *n*, and results to be:

$$s_n = 0.23 \, [rpm] \qquad (71)$$

In the case of the rising edge approach, the Probability Density Function (PDF) for the time shift measured by direct timing of each pair of rising edges, $g_{\Delta t_r}(\eta)$, has been computed through MCM, where 10^6 simulations have been performed to deliver a 95% coverage interval for the output quantity according to [184]. In this case $g_{\Delta t_r}(\eta)$ depends on the propagation through the model of the PDFs of the following independent input quantities (Figure 82), each with its own statistical dispersion:

- the time interval between the optical probe samples, with an associated rectangular PDF having a width equal to $2a_{\frac{1}{f_{OP}}}$, where:

$$a_{\frac{1}{f_{OP}}} = \dfrac{1}{2 * f_{OP}} \qquad (72)$$

- the zebra tape laser-printing resolution, with an associated rectangular PDF and $2a_p$ width, where, assuming a 1200 dpi laser printer, the printing tolerance, a_p, is given by:

NON-INTRUSIVE TORQUE MEASUREMENT

$$a_p = \frac{(25.4 * 10^{-3})}{1200} = 2.128 * 10^{-5}[m] \qquad (73)$$

- the shaft cylindricity error, with rectangular PDF and $2a_d$ width, where assuming an IT8 tolerance class of the shaft, its dimensional tolerance, a_d is given by [185];
- the shaft radial movements (possibly due to vibrations), assumed acting in the direction perpendicular to the optical sensor axis, with Gaussian PDF and standard deviation:

$$s_v = 60 * 10^{-6}[m] \qquad (74)$$
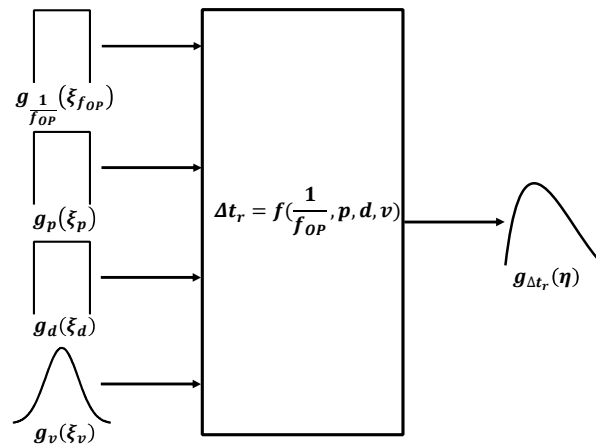
Figure 82. PDF propagation of the four independent input quantities to provide the PDF of $\varDelta t_r$ (adapted from [184]).

Table 21 summarises the input parameters contributing to the uncertainty of $\varDelta t_r$, $u_{\varDelta t_r}$, each with its associated uncertainty intervals used in the model; the amplitude of these intervals is assumed based on knowledge of the technology implemented in the system; it is either the width of a flat PDF or a standard deviation of a gaussian PDF, depending on the type of parameter. The table provides also a sensitivity analysis, i.e. an estimate of the contribution to the overall uncertainty budget for each input parameter, showing that the zebra tape laser-printing and the shaft cylindricity errors are the major contributors to uncertainty $u_{\varDelta t_r}$.

Within each shaft revolution, the standard deviation of $\overline{\Delta t_r}$, $s_{\overline{\Delta t_r}}$, has been then obtained through MCM as the average of the eight pulse train rising edges, Δt_r, and their PDFs, $g_{\Delta t_r}$.

Xj		Standard deviation sj	Half-width tolerance aj	Sensitivity analysis $\left(\dfrac{d\hat{f}}{dx_j}\right)^2 ux_i^2$
Symbol	Name			
$\dfrac{1}{f_{OP}}$	Optical probe sampling frequency		$4.00 * 10^{-6}$ s	$1.33 * 10^{-12}$ s
p	Zebra tape laser-printing		$2.12 * 10^{-5}$ m*	$2.76 * 10^{-7}$ s
d	Shaft cylindricity error		$33 * 10^{-6}$ m*	$4.30 * 10^{-7}$ s
v	shaft movements	$60 * 10^{-6}$ m*		$5.63 * 10^{-10}$ s

* *model assumption*

Table 21. Uncertainties and sensitivity analysis of the quantities contributing to $u_{\Delta t_r}$.

In the case of the cross-correlation approach, the same Gaussian PDF, with the uncertainty $u_{\Delta t_r}$, has been assumed for all the time shifts measured between the rising and falling edges, respectively. Unlike the rising edge detection approach, in this case the standard deviation of Δt_c, $s_{\Delta t_c}$, has been obtained by type B analysis [157] as:

$$s_{\Delta t_c} = \frac{u_{\Delta t_r}}{\sqrt{2ppr}} \tag{75}$$

The PDF for T, $g_T(\eta)$, depends on the propagation through the model of the PDFs of the independent input quantities, K, n and Δt (i.e. $\overline{\Delta t_r}$ or Δt_c, depending on the approach adopted) as described in Figure 83.
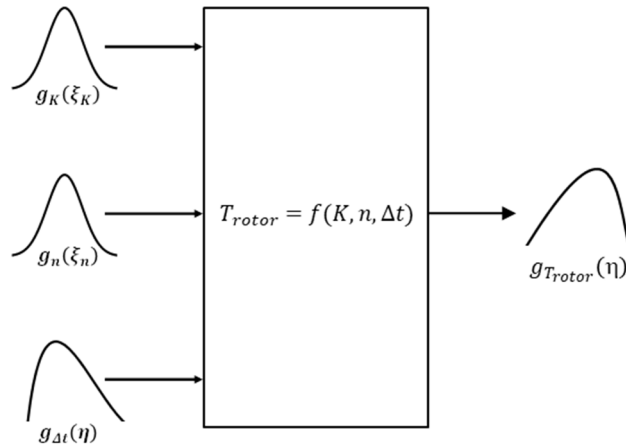
Figure 83. PDF propagation of *K*, *n* and *Δt* to provide the PDF of *T_rotor* through the zebra tape torque meter model (adapted from [184]).

Table 22 summarises the quantities used for the estimation of the uncertainty of T_{rotor}, $u_{T_{rotor}}$, and their sensitivity analysis, showing that, in both approaches, the estimation of Δt is the major contributor to $u_{T_{rotor}}$.

X_j			Standard deviation s_j	Sensitivity analysis	
Symbol	Name	Value		Rising edge	Cross-correlation
K	shaft torsional stiffness	$159.523\ \dfrac{\text{Nm}^*}{\text{rad}}$	$0.0077\ \dfrac{\text{Nm}^*}{\text{rad}}$	$5.965*10^{-7}$ Nm	
n	shaft rotational speed	1700 rpm*	0.23 rpm*	$4.686*10^{-6}$ Nm	
$\overline{\Delta t_r}$	Time shift measurement by direct timing of rising edges	$5.63*10^{-4}$ s*	$1.27*10^{-5}$ s**	0.131 Nm	
$\overline{\Delta t_c}$	Time shift measurement by cross-correlation	$5.51*10^{-4}$ s*	$1.27*10^{-5}$ s**		0.137 Nm

*experimental result; **MCM result

Table 22. Uncertainties and sensitivity analysis of the quantities contributing to $u_{T_{rotor}}$.

For both approaches, Table 23 shows the torque measurement type B expanded uncertainty at 95% confidence level (i.e. corresponding to two standard deviations) obtained by applying the MCM in compliance with the ISO GUM [184] and expressed as a percentage of the system full-scale torque $T_{rotor-max}$.

Method	u$_{MCM}$ [%]
Rising Edge	±1.2
Cross-Correlation	±1.2

Table 23. Torque meter system Type B expanded uncertainty, u$_{MCM}$.

In both cases, the results show that the application of the MCM to a simplified model of the measurement system overestimates the overall system uncertainty when compared to the type A uncertainty obtained by experimental results in laboratory conditions, as reported in Table 19 Parameters of the two calibration curves and relative Type A uncertainty, $U_{cal\_T_{rotor}}$Table 19. The rising edge detection approach shows the larger difference between the values of u$_{MCM}$ and $U_{cal\_T_{rotor}}$. Indeed, it is reasonable that a type A evaluation based on laboratory data underestimates uncertainty, because the MCM method takes into account all possible sources of uncertainty which may occur in a real world application; however, in a laboratory experiment, not all of them will act therefore the uncertainty estimated thought a statistical processing of experimental data can be lower. Therefore, the uncertainty estimated by MCM method sets an upper limit to possible uncertainty attainable in a real world application.

6.4.3 Experimental results

Tests have been performed to validate the proposed algorithms under both static and dynamic conditions. The torque measurements obtained by the zebra tape torque meter have been compared with measurements from in-line torque transducer (Magtrol) which we considered as the reference system for all the work, being a well established technique at state-of-art. Shaft speed was also recorded by the zebra tapes.

6.4.3.a   Steady state test results

Figure 84 shows speed and torque results for two steady state tests performed at 1700 rpm, 4 Nm and 1900 rpm, 10 Nm. Both the cross-correlation (azure line) and rising edge (red line) approaches show good agreement, on average, with reference transducer measurements (black dotted line) however the zebra tape data appears noisier. This is particularly apparent for torque measurements obtained by cross-correlation. The causes of noise in this data have been already outlined when showing the calibration results however it should also be noted that the reference transducer is sampled at a much lower rate, possibly reducing its own noise levels.

NON-INTRUSIVE TORQUE MEASUREMENT

The frequency at which noise appears for the optical system is significantly higher than any relevant frequencies expected in the mechanical torque signal therefore such noise could be reduced by low pass digital filtering.
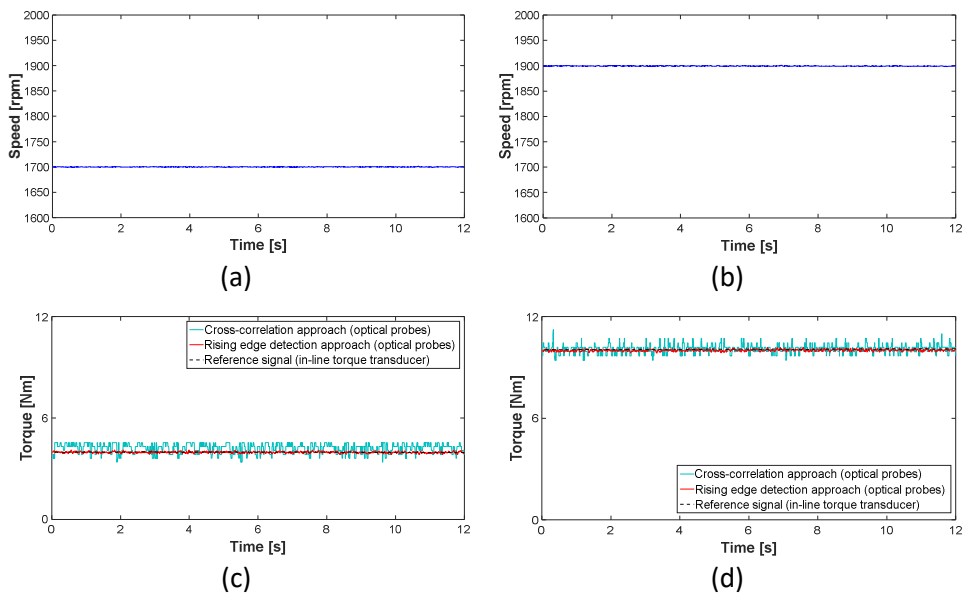
Figure 84 Optical system speed and torque measurement under steady state conditions: (a) and (c) 1700 rpm and 4 Nm; (b) and (d) 1900 rpm and 10 Nm

6.4.3.b   Dynamic test results

Finally, dynamic tests have been performed to evaluate and compare the dynamic response of the two approaches. Figure 85 shows the effects of sharp step changes in torque. The shaft speed was initially set at around 1715 rpm and the torque first increased and then decreased in steps of approximately 2 Nm, in the 0-15 Nm operating range. Changes in speed are the result of applied torque that were not countered by the variable speed drive. The zebra tape measurements allow tracking of the rotational frequency as well as the torque during the whole transient. The dynamic response of the zebra tape torque meter is sufficient to track the torque variations imposed on the shaft. Both the rising edge and cross correlation torque estimations follow the step changes well and without any timing delay. However, as already noted, the outputs are noisier, especially when the cross-correlation approach is applied. Low pass filtering would reduce this noise without affecting torque meter dynamic response in the band of frequencies of interest for mechanical torque measurements.
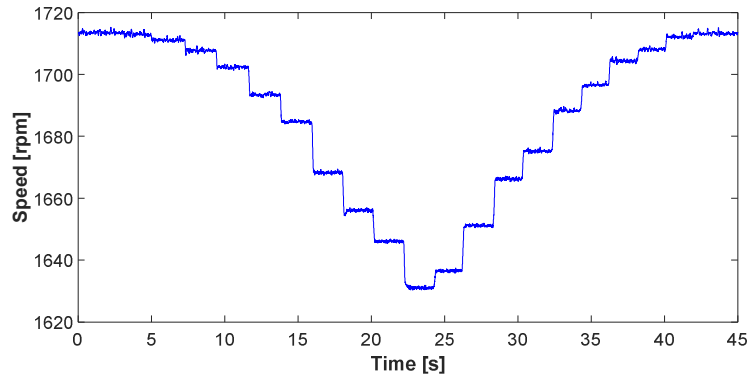
(a)
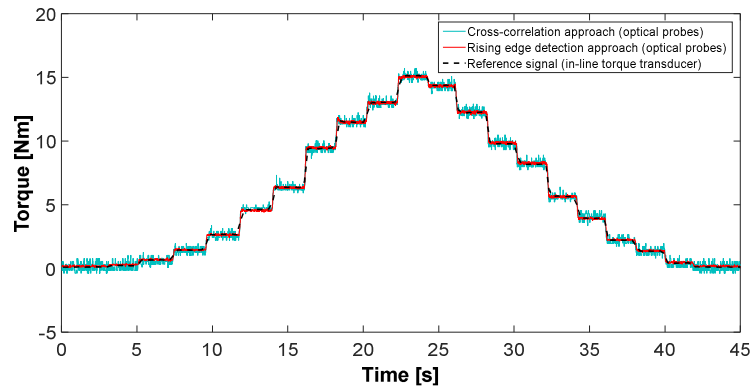
(b)

Figure 85 Optical system speed (a) and torque (b) measurements under sharp step torque changes

Additional dynamic tests have been performed by applying a harmonic input torque at three different frequencies (0.17 Hz, 0.30 Hz and 0.63 Hz) and at a peak-to-peak amplitude of approximately to 6 Nm (Figure 86 a-b), within experimental limitations. Again, the zebra tape torque meter shows a good dynamic response under harmonic changes of input torque, even if affected by greater high frequency noise in the case of the cross-correlation approach.

NON-INTRUSIVE TORQUE MEASUREMENT
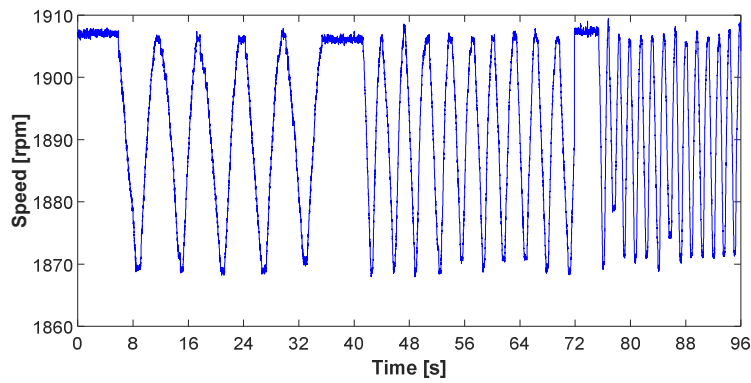
(a)
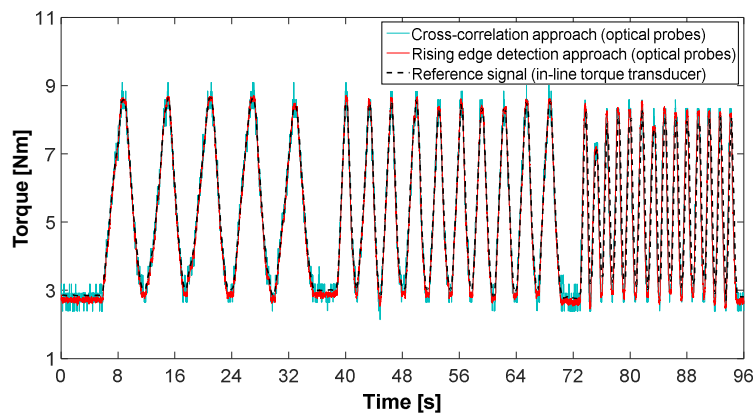
(b)

Figure 86 Optical system speed (a) and torque (b) measurements under torque varying at three different frequencies (0.17 Hz, 0.30 Hz and 0.63 Hz)

6.5 Comparison with conventional twist angle measurement methods

Similarly to the conventional twist angle measurement methods [167][152][172] [173], the time shift between the signals recorded by the two zebra tape torque meter optical probes is a function of the twist of the shaft due to the applied torque. However, the non-intrusive system presented in this paper has the significant advantages of using less-intrusive, cheaper, easier and quicker to install equipment, making it suitable for a larger range of industrial applications, even in confined, challenging or sensitive operating environments, without any significant impact on shaft design and mechanical integrity. In addition to torque measurement, the zebra tape torque meter provides the shaft rotational speed, which allows the measurement of the mechanical power transmitted by the shaft. This results in a reduction in the number of sensors in the system and hence saving in space, weight

and complexity, which is particularly important for many industrial applications, such as in the naval and wind energy sectors. The measurement system is reliable, robust and straightforward to use. The zebra tapes can be designed to be fitted or retrofitted on any shaft diameter and material, while all the electronic components remain on the static part of the system, making the system compatible with harsh and polluted environments. High measurement accuracy and resolution can be achieved by accurately designing the width of the zebra tape black and white stripes to suit the particular application. Thanks to the easy glue-on installation of the zebra tapes, the measurement system can be moved to other similar installations easily in a very short amount of time. This is ideal when torque monitoring forms part of the final check-out of multiple machines. By simply modifying the separation distance of the two zebra tapes along the shaft, when its length allows, different measurement sensitivities can be achieved according to the field application requirements. This would generally result in sensitivities higher than conventional optical torque measurement systems.

6.6   Feasability zebra tate application

The torque measurement on rotating shafts through a pair of zebra tapes showed good metrological performance in laboratory tests, especially if the rising edge approach is applied. These results, obtained by a laboratory experience, should be extended to real situations in order to verify the applicability of the technique. Therefore, this paragraph performs a feasibility analysis for scaling up the zebra tape torque meter to be applicable to two two real shaft configurations of real wind turbines, based on the expected torque uncertainty, according to equation (76). In particular, this uncertainty is evaluated by comparing the time shift uncertainty $U_{\Delta t}[s]$, calculated by experimental data given by test bench results according to equation (77), with the expected maximum time shift Δt_{max}.

$$U_{T_{rotor}}[\%] = \frac{U_{\Delta t}[s]}{\Delta t_{max}[s]} * 100 \qquad (76)$$

$$U_{\Delta t}[s] = \frac{60 * U_{cal\_T_{rotor}}[Nm]}{2\pi n * K} = 0.00000662 \, [s] \qquad (77)$$

where K, the shaft torsional stiffness, is given by the inverse of the slope of the calibration curve and n is the shaft rotational speed.

Evaluating the uncertainty in accordance with equation (76) is approximate, because it considers that all uncertainty contributions that affect a real application have been appropriately considered in the $U_{\Delta t}[s]$ calculation; however, assumption necessary in this thesis given the impossibility to tests the technique on a real wind turbine shaft.

Below is reported a feasibility analysis for two drive train configurations:

NON-INTRUSIVE TORQUE MEASUREMENT

- 60kW wind turbine and drivetrain with gearbox;
- 3 MW wind turbine and direct drivetrain.

6.6.1   60 kW wind turbine and drivetrain with gearbox

Figure 87 shows an example of a drivetrain with a gearbox for a 60 kW wind turbine. The gearbox allows to transfer the torque between the slow shaft, connected to the rotor, with the fast shaft connected to the generator. The fast shaft is usually unfavourable for the application of the zebra tape torque technique because the time shift between the rising edges of the pulse train decreases linearly with the shaft speed and the shaft length; the fast shaft is shorter, since it can be totally or partially embedded within the generator and is faster.

For these reasons, for the drive train with gearbox the feasibility analysis will be performed for a pair of zebra tapes glue on the slow shaft.
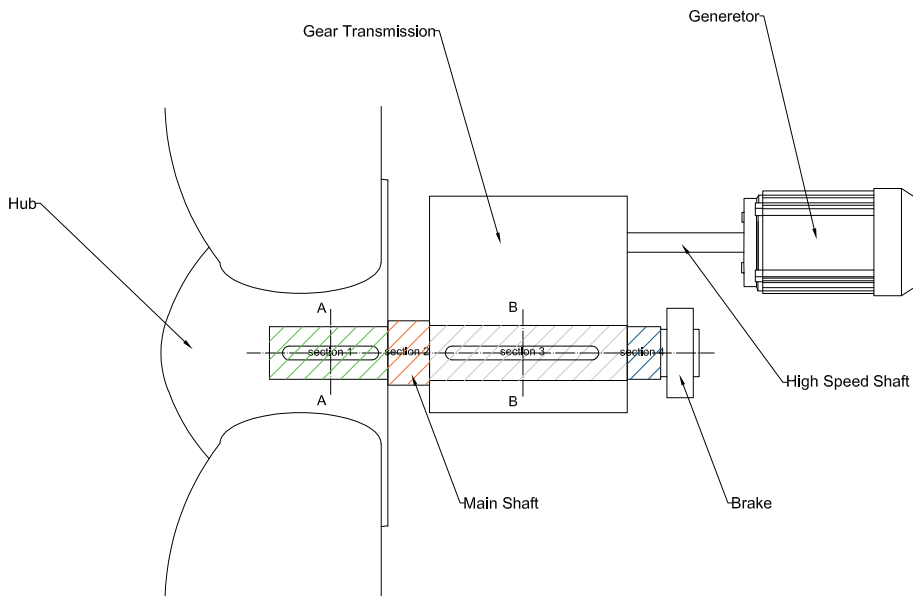
Figure 87 60 kW wind turbine and drivetrain with gear box

The main shaft, shown in Figure 87, can be split in 4 sections:

- Section 1: this part is inserted inside the hub and on it a driving torque is applied, which for simplicity, can be imagined as a torque applied on the A-A axis. This section is usually not easy to access and a zebra tape cannot be install;
- Section 2: It is a free shaft part and is often the first useful section to install a zebra tape;
- Section 3: It is the shaft part inserted inside the gearbox and on it a braking torque is applied, which for simplicity, can be imagined as a torque applied

on the B-B axis. This section is usually not easy to access and a zebra tape cannot be install;

- Section 4: It is the part of shaft that comes out from the gearbox and that precedes the brake. It is the last useful section to install a zebra tape.

According to this list, Figure 88 shows the torque diagram of the shaft and the maximum possible distance between the pair of zebra tape (Z1 and Z2). This zebra tape distance and shaft dimensions represent the standard, for a 60 kW wind turbine and drive train with gear box, in relation to which a feasibility analysis of the torque measurement technique will be performed below.

Figure 88 Shaft of 60 kW wind turbine and drivetrain with gearbox

The maximum torque value, $T_{rotor-max}$, applied to the shaft is not available from the data sheet of the WT but can be calculated, according to equation (78), from the maximum power delivered from the generator and assuming values for the generator's efficiency and the mechanical transmission efficiency of the gearbox. Typical technical values and the maximum expected torque for a 60 kW wind turbine and drivetrain with gearbox are given in Table 24.

$$T_{rotor-max} = \frac{P_{t-max} * 60}{2 * \pi * n_{max} * \eta el * \eta mec} \tag{78}$$

P_{t-max}: Maximum power	60000	[W]
n_{max}: Maximum rotor speed	60	[rpm]
η_{el}: Generator's efficiency	0.95	
η_{mec}: Mechanical transmission efficiency	0.9	
$T_{rotor-max}$: Maximum torque	11169	[Nm]

Table 24 Expected shaft torque for 60 kW wind turbine and drivetrain with gearbox

NON-INTRUSIVE TORQUE MEASUREMENT

The maximum expected angular and time shift between the zebra tape sections (Z1 and Z2) are given by the equations (79) and (80).

$$\theta_{max} = \frac{32 * T_{rotor-max} * L}{\pi * G * (D_e^4 - D_i^4)} \tag{79}$$

$$\Delta t_{max} = \frac{60}{2\pi n} \theta_{max} \tag{80}$$

E: Young modulus	2.1E+11	[GPa]
v: Poisson's ratio	0.3	
G: Shear modulus	80769230769	[Pa]

Table 25 Technical data of 42CrMo4 steel

Assuming that the shaft is made of 42CrMo4 steel, with mechanical properties such as those shown in Table 25, the maximum expected angular and time shift are $\theta_{max} = 0.00207$ [rad] and $\Delta t_{max} = 0.000330$ [s]. Finally, considering the hypothesis that all uncertainty contributions that affect a real application have been appropriately considered in the $U_{\Delta t}$ [s], the uncertainty of the torque measurement through a pair of zebra tape is estimated to be $U_{T_{rotor}} = 2.0$ [%] for a 60 kW wind turbine and drive train with gearbox.

6.6.2 3 MW wind turbines and direct drive train

Figure 89 shows an example of direct-drive train of multi megawatt wind turbines. A low speed shaft connects the rotor to the generator.
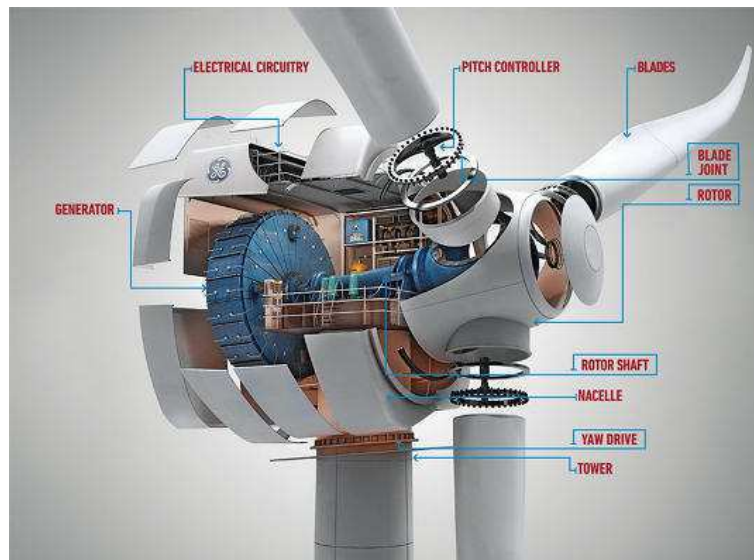
Figure 89 Multi megawatt wind turbine and direct drivetrain [188]

According to Figure 89 the shaft can be split in 5 sections:

- Section 1: this part is inserted inside to the hub and on it a driving torque is applied, which for simplicity, can be imagined as a torque applied on the A-A axis. Also this disc is often used as a brake disc. This section is usually not easy to access; therefore, a zebra tape cannot be install;
- Section 2: It is a free shaft part; however, given its conic trunk section, it is often advisable not install any zebra tape;
- Section 3: It is the shaft part in which the bearing is inserted and a zebra tape cannot be install;
- Section 4: It is the free shaft part at the ends of which a pair of zebra tape can be installed;
- Section 5: It is the shaft part inserted inside the generator and on it a braking torque is applied, which for simplicity, can be imagined as a torque applied on the B-B axis. This section is usually not easy to access and a zebra tape cannot be install.
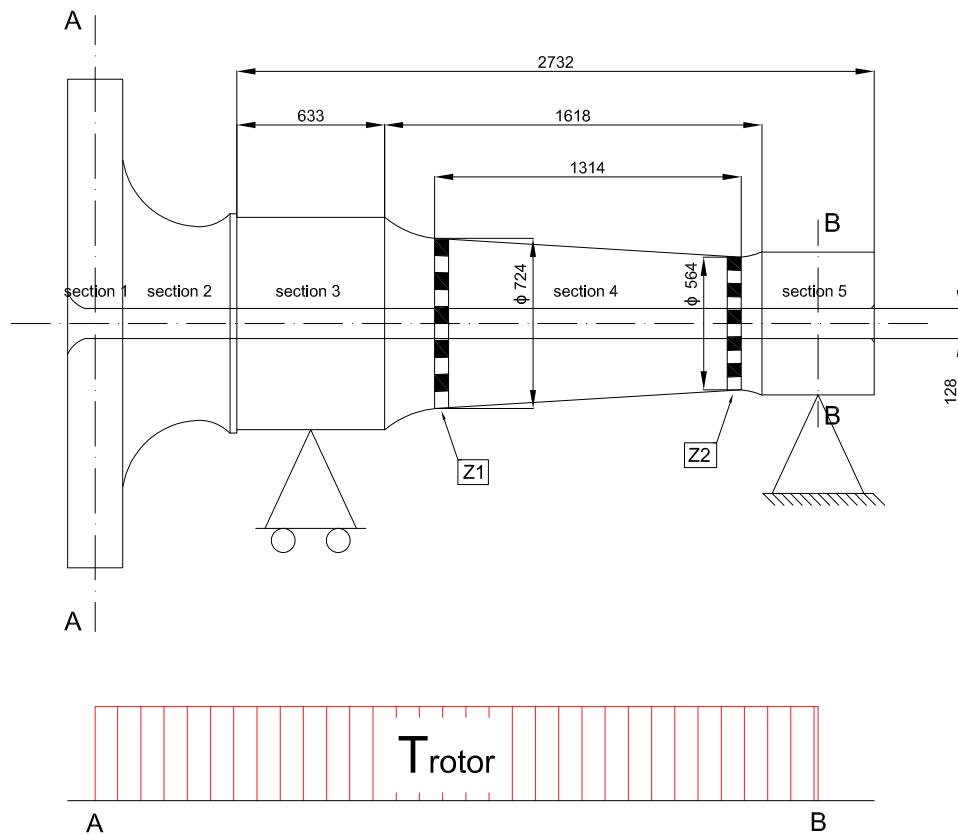
Figure 90 Main shaft for direct drive 3 MW wind turbine [189]

According to this list, Figure 90 shows the torque diagram of the shaft and the maximum possible distance between the pair of zebra tape (Z1 and Z2). This zebra tape distance and shaft dimensions represent the standard, for a 3 MW wind turbine and direct drive train, in relation to which a feasibility analysis of the torque measurement technique will be performed below.
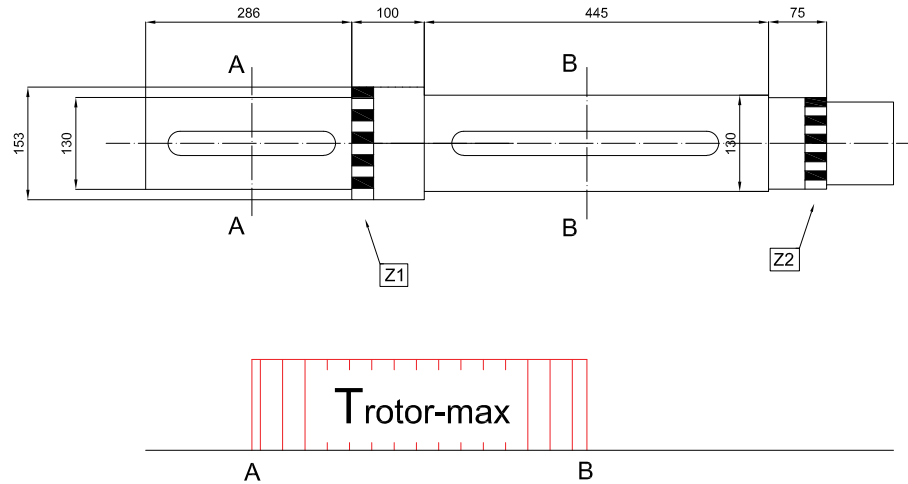
The maximum torque value, T$_{rotor-max}$, applied to the shaft is not available from the data sheet of the WT but can be calculated, according to equation (78), from the maximum power delivered from the generator and assuming values for the generator's efficiency and the mechanical transmission efficiency of the gearbox. Typical technical values and the maximum expected torque for a 3 MW wind turbine and direct drivetrain are given in Table 26.

P_{t-max}: Maximum power	3000000	[W]
n_{max}: Maximum rotor speed	15	[rpm]
η_{el}: Generator's efficiency	0.95	
η_{mec}: Mechanical transmission efficiency	0.98	
$T_{rotor-max}$: Maximum torque	2051406	[Nm]

Table 26 Expected shaft torque for 3 MW wind turbine and direct drivetrain

Assuming that the shaft is made of 42CrMo4 steel, with mechanical properties such as those shown in Table 25, the maximum expected angular and time shift are $\theta_{max} = 0.00198 \text{[rad]}$ and $\Delta t_{max} = 0.00126 \, [s]$. Finally, considering the hypothesis that all uncertainty contributions that affect a real application have been appropriately considered in the $U_{\Delta t} \, [s]$, the uncertainty of the torque measurement through a pair of zebra tape is $U_{T_{rotor}} = 0.5 \, [\%]$ for 3 MW wind turbines and direct drive train.

Finally, comparing the expected uncertainties $U_{T_{rotor}}$ for the two turbine and shaft solutions discussed above, the measurement of torque by a pair of zebra tapes is less uncertain when performed on long and slow shafts.

7 CONCLUSION AND FUTURE WORK

7.1 Conclusion

Wind turbines play a key role in renewable energy sources. This led to a steady increase in wind energy production, but forecasts, which were even more positive, were not reached due to O&M costs. For this reason, wind turbine certification and development of condition monitoring techniques are critical for the future of wind turbines, as these allow to demonstrate that the operational conditions are compliant to the project design (mechanical stress, acoustic emission, power output ...) and that the defects can be predicted in advance enough to avoid serious failures, which would cause long machine stops and long pay back periods. However, it is increasingly complex to extract reliable information about the wind turbines operational conditions, due their increasing complexity and size. Problems in the procedures and methods for obtaining reliable data on the mechanical behaviour for monitoring and certify wind turbines were the central theme of this doctoral work. The thesis at first discussed the criticalities to apply the current standard, IEC 61400/13, for a mechanical certification and gave suggestions and reccomendations to overcome these problems. At the state of the art, there are not many critical analyses in this regard. Then, it presented the deployment and use of the optical trasducer to mesure torque on rotating shaft of wind turbines. The non-intrusive torque measurement system proposed represents the holds most of the novelty of this work. Indeed, no similar technology has ever been studied and applied for the application on wind turbines.

Regarding the mechanical certification of wind turbines, this work provides in Chapter 4 and 5 an insight into the measurement problems associated to model based calibration of strain gage bridges used for mechanical load measurement according to the standard IEC-61400/13.

Chapter 4 discusses the guidelines that need to be followed for defining the strain gage measurement chain, showing the possible configurations of the full strain gage bridges (parallel or T), the possible electrical connection (4 wires or 6 wires) and showing a typical configuration of the DAQ network system. Next, the procedure for analytical and gravity calibration have been discussed. These two calibration have to be performed when it is impossible to perform a calibration by applying real mechanical inputs to the turbine, which is more and more complex for large wind turbines due to their size and due to the magnitude of forces which would be necessary. Concerning gravity calibration, kinematic and dynamic models of the wind turbine have been presented, they can be used to provide a series of reference input loads, which allow to calibrate the various elements of turbine (tower, shaft, blades) using the unbalanced masses of the structure itself. The loads generated through these unbalances, for some turbine sections, will only cover part

of the measurement range; such as bottom tower bending moments, the fraction of the full scale may be really small, lower than 5%, because unbalanced masses cause small bending moments relative to those generated by aerodynamic actions during operation. In these cases, a combination of analytical and gravity loads calibration methods is required.

Chapter 5 then examines the problems to evaluate calibration uncertainty and signal uncertainty of WTs and provides a complete example based on typical 2 MW WT characteristics.

Concerning calibration uncertainty, the uncertainty of the reference inputs is conducted by a type B methodology, according to the ISO-GUM. Literature suggests that the reference input used in a calibration process should have an uncertainty lower or equal to 1/4 of the measurement uncertainty of the device being calibrated; in any case, the choice of a smaller ratio would improve the calibration process. The regression of calibration data would then provide a mean to determine the statistical uncertainty type A. Finally, the uncertainty of the reference input should be combined to the statistical uncertainty of the calibration in order to estimate the overall calibration uncertainty, which in IEC-61400-13 should be lower than 3%. A reduction in the uncertainty of the input reference eases to meet this requirement. The thesis shows that the contribution of the input reference uncertainty in a model based calibration of a large wind turbine can be reduced and therefore in practice neglected, if it is one order of magnitude lower than desired uncertainty set for the load measurement. Results from calibration of a typical class II 2 MW wind turbine show an uncertainty of the input load in the order of 0.2÷0.5 % of full scale, which is one order of magnitude lower than the target 3 % set by IEC-61400-13 standard.

Furthermore, the thesis provides an analysis of the influence of thermal contributions. The analysis shows that these effects cause zero drift and sensitivity drift. Thermal effects occur both during measurement campaign and calibration process, due to the long time required. Therefore, thermal effects should be considered both in signal uncertainty and calibration uncertainty.

For bridges in T configuration, the thermal effect is about 0.2 *%* for 5 *°C* temperature variation or difference, while in case of parallel bridges installed on the tower, these negative effects will easily reach 1 *%*. Although the thermal effects during the calibration process can be limited or kept under control, they are surely present during the measurement campaign and then the signal uncertainty due to thermal effects may reach very high values. Therefore, Chapter 5 has provided the guideline to perform thermal compensation and the equations that have to be used to evaluated the signal uncertainty due to thermal effects, if a thermal compensation can be performed.

However, in order to reduce the uncertainty due to the thermal effects, a careful choice of bridge configuration have to be performed. In particular, the T

CONCLUSION AND FUTURE WORK

configuration should be preferred in tower top and bottom bending moment, because it allows compensating the temperature difference between the two sides of the bridge. Concerning shaft measurements, given that the shaft is rotating, it is possible to assume that the strain gages are isothermal. The parallel configuration should be than preferred, considering that its sensitivity is larger than a full bridge in T configuration. Finally, for blade in composite material the parallel bridge configuration should be preferred, because due to the anisotropy of the fiberglass, the behaviour under temperature and humidity variation is different along different axes. This makes useless the application of T-rosettes, which will not compensate thermal effects having different value over different direction.

In addition to machine certification, condition monitoring is a crucial aspect for the future of wind energy. In particular, many studies have shown that an accurate torque measurement can provide much information about the WT's health and it has been shown to be successful in the detection of faults in the main drive train components. Although WT torsional effects are important, torque measurement on wind turbine shaft is a complex task today; the available solutions are uncertain (like strain gage) or invasive (like inline torque sensor). This thesis has presented and analysed a new non-intrusive technique for shaft speed and torque measurement consisting of a set of two zebra tapes and optical probes; this study rappresentes the holds most of the novelty of this work. As the shaft rotates, each optical sensor generates a pulse train signal proportional to the light intensity reflected by the zebra tape stripes. Shaft rotational speed has been calculated by measuring the times at which the rising edges of the pulse trains occur. Torque has been estimated by measuring the angle of twist from the pulse train time shift measurements through the application of rising edge detection and cross-correlation approaches. The contactless, optical torque measurement system performance has been demonstrated by comparing the results from both approaches against reference measurements from an in-line torque transducer mounted on the test bench shaft. Experimental measurements under steady state conditions, performed to calibrate the contactless system, show a linear relationship between torque and twist, in perfect agreement with theoretical predictions. The rising edge and the cross-correlation torque measurements correlate closely with the in-line transducer measurements under both steady state and dynamic torque conditions, with ±0.3 and ±0.8 uncertainty, respectively. A Montecarlo method has been also used to estimate measurement uncertainty in real world conditions, by simulating statistical variations of the parameters affecting system performance; in the worst case, expanded uncertainty is lower than ±1.2 %. The larger uncertainty associated with the cross-correlation method is shown to be due to the combined effect of its higher sensitivity to the pulse shape and to the position of its centre. Low pass digital filtering would reduce the noise associated with the cross-correlation approach without affecting the torque meter

dynamic response. Unlike conventional in-line torque transducers and the conventional strain gauge technique, the proposed zebra tape torque meter does not require costly embedded sensors, electronics or wires on the rotating shaft. Comparing with conventional twist angle measurement methods, the proposed methodology is less intrusive, simpler and cheaper to implement, making it suitable to a larger variety of engineering applications. Measurement accuracy and resolution can be easily adapted to the field application requirements by carefully designing the zebra tapes and their separation along the shaft. A feasibility analysis for two real shaft configurations and real wind turbines has been performed, 60 kW wind turbine with drive train with gearbox and 3 MW wind turbine with direct drive train. The expected uncertainty for the two solutions is 2.0% and 0.5%, respectively. Therefore, the technique is more reliable to measure torque of slow and long shaft, typical of a large wind turbine with direct drivetrain.

7.2 Further Work

The future works discussed below refer to the two areas of interest presented in this thesis.

Future work about wind turbines certification:

- Development of cross-talk phenomenon compensation models, these models should also provide a study of the uncertainty obtainable following this compensation;
- Development of mathematical models to calibrate the blade pitch actuation.

Future work about the develop of torque measurement technique:

- Reduce the relative movements between the optical probes and the shaft, that have been identified as the main causes of uncertainty; this have to be done by improving the measurement chain and the data processing algorithm. Where, the movements can be caused by radial and tangential vibrations, thermal expansion, non-cylindrical expansion of the shaft, ...;
- Develop and test an optical system that can operate in dirty environments and in aggressive conditions, with strong variations in temperature and humidity, without experiencing sharp sensitivity reduction and therefore causing increased uncertainty in the torque measurement;
- Test the capacity and the sensitivity of the proposed technique to detect drive train faults;
- Test the technique on a real wind turbine shaft;
- Make the data processing algorithms faster, which can get in output real-time torque information.

8 REFERENCES

[1]   Conti J., Holtberg P., Diefenderfer J., LaRose A., Turnure J. T. and Westfall L. (2016). International Energy Outlook 2016, DOE/EIA-0484(2016). Independent statistics & analysis, U.S. energy information administration.

[2]   United Nations 2015 Report of the Conference of the Parties on its twenty-first session (*Paris from 30 November to 13 December 2015*).

[3]   Solomon S., Qin D., Manning M., Chen Z., Marquis M., Averyt K.B., Tignor M. and Miller H.L. (2007). IPCC: Summary for Policymakers. In: *Climate Change 2007: The Physical Science Basis. Contribution of Working Group I to the Fourth Assessment Report of the Intergovernmental Panel on Climate Change*. Cambridge University Press, Cambridge, United Kingdom and New York, NY, USA.

[4]   Santer B.D., Taylor K.E., Wigley T.M.L., Johns T.C., Johns P.D., Karoly D.J., Mitchell J.F.B., Oort A.H., Penner J.E., Ramaswamy V., Schwarzkopf M.D., Stouffer R.J. and Tett S. (1996). A search for human influences on the thermal structure of the atmosphere. *Nature,* 382**,** 39-46, doi:10.1038/382039a0.

[5]   Hegerl G.C., von Storch H., Hasselmann K., Santer B.D., Cubasch U. and Jones P.D. (1996). Detecting Greenhouse-Gas-Induced Climate Change with an Optimal Fingerprint Method. *Journal of Climate*, 9, 2281-2306, doi: *https://doi.org/10.1175/1520-0442(1996)009<2281:DGGICC>2.0.CO;2*.

[6]   Ramaswamy V., Schwarzkopf M.D., Randel W.J., Santer B.D., Soden B.J. and Stenchikov G.L. (2006). Anthropogenic and Natural Influences in the Evolution of Lower Stratospheric Cooling. *Science* 311, 1138-1141, doi: 10.1126/science.1122587.

[7]   Santer B.D., Wehner M.F., Wigley T.M., Sausen R., Meehl G.A., Taylor K.E., Ammann C., Arblaster J., Washington W.M., Boyle J.S. and Brüggemann W. (2003). Contributions of Anthropogenic and Natural Forcing to Recent Tropopause Height Changes. *Science*, 301, 479-483, doi:10.1126/science.1084123.

[8]   Coiew J. (2007) *Climate change: biological and human aspects*, Cambridge, New York: Cambridge University Press.

[9]   Church J. A., and White N. J. (2006), A 20th century acceleration in global sea-level rise. *Geophys. Res. Lett.*, 33, L01602, doi:10.1029/2005GL024826.

[10]   Shaftel H., Jackson R. and Tenenbaum L. (2017). *GLOBAL CLIMATE CHANGE: Vital Signs of the Planet*. Available at https://climate.nasa.gov/, accessed 20 August 2017.

[11]   Levitus S., Antonov J. I., Boyer T. P., R. A. Locarnini, H. E. Garcia and A. V. Mishonov (2009). Global ocean heat content 1955–2008 in light of

recently revealed instrumentation problems. *Geophys. Res. Lett.,* 36, L07608, doi: 10.1029/2008GL037155.

[12]   Polyak L., Alley R.B., Andrews J.T., Brigham-Grette J., M.Cronin T., Darby D.A., Dyke A.S., Fitzpatrick J.J., Funder S., Holland M., Jennings A.E., Miller G.H., O'Regan M., Savelle J., Serreze M., John K. St., White J.W.C., Wolff E. (2010). History of Sea Ice in the Arctic. *Quaternary Science Reviews*, 29, Issues 15–16, 1757-1778, doi: https://doi.org/10.1016/j.quascirev.2010.02.010.

[13]   Kwok R. and Rothrock D.A. (2009). Decline in Arctic sea ice thickness from submarine and ICESat records: 1958–2008. *Geophys. Res. Lett.*, 36, L15501, doi:10.1029/2009GL039035.

[14]   Zemp M., Gärtner-Roer I., Nussbaumer S.U., Hüsler F., Machguth H., Mölg N., Paul F., and Hoelzle M. (2015). Global Glacier Change Bulletin No. 1 (2012-2013)., ICSU(WDS) / IUGG(IACS)/ UNEP / UNESCO / WMO, World Glacier Monitoring Service, Zurich, Switzerland.

[15]   Sabine C.L., Feely R.A., Gruber N., Key R.M., Lee K., Bullister J.L., Wanninkhof R., Wong C.S., Wallace D.W.R., Tilbrook B., Millero F.J., Peng Tsung-Hung, Kozyr A., Ono T., Rios A.F. (2004). The Oceanic Sink for Anthropogenic CO2. *Science*, vol. 305 , 367-371.

[16]   Allison I., Bindoff N., Bindschadler R., Cox P., de Noblet N., England M., Francis J., Gruber N., Haywood A., Karoly D., Kaser G., Le Quéré C., Lenton T., Mann M., McNeil B., Pitman A., Rahmstorf S., Rignot E., Schellnhuber H.J., Schneider S., Sherwood S., Somerville R., Steffen K., Steig E., Visbeck M. and Weaver A. (2017). The Copenhagen Diagnosis: Updating the World on the Latest Climate Science. Available at http://www.copenhagendiagnosis.org/default.html, accessed 20 August 2017.

[17]   Derksen C. and Brown R. (2012). Spring snow cover extent reductions in the 2008–2012 period exceeding climate model projections. *Geophys. Res. Lett.,* 39, L19504, doi:10.1029/2012GL053387.

[18]   Renewable energy Moving towards a low carbon economy. Available at: https://ec.europa.eu/energy/en/topics/renewable-energy, accessed 20 August 2017.

[19]   EUROPEAN COMMISSION (2015). REPORT FROM THE COMMISSION TO THE EUROPEAN PARLIAMENT, THE COUNCIL, THE EUROPEAN ECONOMIC AND SOCIAL COMMITTEE AND THE COMMITTEE OF THE REGIONS: Renewable energy progress report, Brussels.

[20]   Serrano-González J. and Lacal-Arántegui R.(2016). Technological evolution of onshore wind turbines—a market-based analysis. *Wind Energ.*, 19:2171–2187, doi: 10.1002/we.1974.

[21]   Way A. C. and Van Zijl G.P.A.G. (2015). A study on the design and material costs of tall wind turbine towers in South Africa. *Journal of the*

South African Institution of Civil Engineering, 57(4), Art. 1231, doi:10.17159/2309-8775/2015/v57n4a6.

[22]   Hansen AD, Iov F, Blaabjerg F and Hansen LH (2004). Review of contemporary wind turbine concepts and their market penetration. *Wind Engineering*, Vol 28, Issue 3, 247–263, doi: 10.1260/0309524041590099.

[23]   Burton T., Sharpe D., Jenkins N. and Bossanyi E (2001). *Wind Energy Handbook*, Wiley: Chichester, UK.

[24]   Polinder H., Bang D.-J., Li H. and Chen Z. (2007). Concept Report on Generator Topologies, Mechanical and Electromagnetic Optimization. *Project UpWind*, Mekelweg, the Netherlands and Aalborg East, Denmark, Tech. Rep.

[25]   Aho J., Buckspan A., Laks J., Fleming P., Jeong Y., Dunne F., Churchfield M., Pao L. and Johnson K. (2012). A Tutorial of Wind Turbine Control for Supporting Grid Frequency through Active Power Control. *Proceedings of American Control Conference (ACC)*, pp. 3120-3131, doi: 10.1109/ACC.2012.6315180.

[26]   Soriano L.A., Yu W. and Rubio Jose de Jesus (2013). Modeling and Control of Wind Turbine. *Mathematical Problems in Engineering*, Volume 2013, Article ID 982597, 13 pages, doi: http://dx.doi.org/10.1155/2013/982597.

[27]   Petersson A., Thiringer T., Harnefors L. and Petru T. (2005). Modeling and experimental verification of grid interaction of a DFIG wind turbine. IEEE Transactions on Energy Conversion, vol. 20, no. 4, pp. 878-886, doi: 10.1109/TEC.2005.853750.

[28]   Salman S. K., Badrzadeh B. and Penman J. (2004). Modelling wind turbine-generators for fault ride-through studies. *Proceedings of the 39th International Universities Power Engineering Conference*, Bristol, UK, vol.1, pp. 634–638.

[29]   Wu F., Zhang Xiao-Ping and Ju P. (2008). Modelling and control of the wind turbine with the Direct Drive Permanent Magnet Generator integrated to power grid. *Proceedings of t*hird International Conference on Electric Utility Deregulation and Restructuring and Power Technologies, Nanjuing, pp. 57-60, doi: 10.1109/DRPT.2008.4523379.

[30]   Peng L., Li Y. and Francois B. (2008). Modeling and control of doubly fed induction generator wind turbines by using causal ordering graph during voltage dips. *Proceedings of the 11th International Conference on Electrical Machines and Systems*, Wuhan, pp. 2412–2417.

[31]   Yin M., Li G., Zhou M. and Zhao C. (2007). Modeling of the wind turbine with a permanent magnet synchronous generator for integration.

Proceedings of the IEEE Power Engineering Society General Meeting, Tampa, pp. 1–6, doi: 10.1109/PES.2007.385982.

[32] Barlas, T. and van Kuik, G.A.M. (2010). Review of state of the art in smart rotor control research for wind turbines. *Progress in Aerospace Sciences*, Volume 46, Issue 1, Pages 1-27, doi: https://doi.org/10.1016/j.paerosci.2009.08.002.

[33] Lio W.H., Jones B.Ll., Lu Q. and Rossiter J.A. (2015). Fundamental performance similarities between individual pitch control strategies for wind turbines. *International journal of control*, Volume 90, Issue 1, pp. 37-52, doi: http://dx.doi.org/10.1080/00207179.2015.1078912.

[34] Lu Q., Bowyer R. and Jones B. Ll. (2015). Analysis and design of Coleman transform-based individual pitch controllers for wind-turbine load reduction. *Wind Energy*, Volume 18, Issue 8, pp. 1451–1468, doi:10.1002/we.1769.

[35] Ela E., Gevorgian V., Fleming P., Zhang Y.C., Singh M., Muljadi E., Scholbrook A., Aho J., Buckspan A., Pao L., Singhvi V., Tuohy A., Pourbeik P., Brooks D. and Bhatt N. (2014). Active Power Controls from Wind Power: Bridging the Gaps. *Technical Report*, No NREL/TP-5D00-60574, doi:10.2172/1117060.

[36] Pitteloud J.-D. and Gsänger S. (2016). 2016 Small Wind World Report - Distributed by World Wind Energy Association. WWEA's Member Survey.

[37] INTERNATIONAL ELECTROTECHNICAL COMMISSION (2005). IEC 61400-1 Wind turbines – Part 1: Design requirements, 3rd Edition.

[38] Swart R.J., Coppens C., Gordijn H., Piek M., Ruyssenaars P., Schrander J.J., Smet P. de, Hoogwijk M., Papalexandrou M., Visser E. de, Horalek J., Kurfürst P., Jensen F.P., Petersen B.S., Harfoot M., Milego R., Clausen N.E. and Giebel G. (2009). Europe's onshore and offshore wind energy potential: An assessment of environmental and economic constraints. *EEA Technical report*, No 6/2009.

[39] Corbetta G., Ho A., Pineda I., Ruby K., Velde L.V.de, Bickley J. (2015). Wind energy scenarios for 2030. *European Wind Energy Association*.

[40] Spenser Anderson (2013). Comparing Offshore and Onshore Wind, HSA 10-5 The Economics of Oil and Energy.

[41] Fried L., Shukla S., Sawyer S., Teske S. (2016). Global Wind Energy Outlook 2016. *Global Wind Energy Council, Institute for Sustainable Future*.

[42] Higgins P., Foley A. (2014). The evolution of offshore wind power in the United Kingdom. *Renewable and Sustainable Energy Reviews,* Volume 37, pp. 599-612, doi: https://doi.org/10.1016/j.rser.2014.05.058.

[43] Snyder B., Kaiser M.J. (2008). Ecological and economic cost-benefit analysis of offshore wind energy. *Renewable Energy,* Volume 34, Issue 6, pp. 1567-1578, doi: https://doi.org/10.1016/j.renene.2008.11.015.

[44] Klug H (2002). Noise from Wind Turbines: Standards and Noise Reduction Procedures. *Proceedings of the Forum Acusticum*, Sevilla.

[45] Pedersen E., Waye K.P. (2004). Perception and annoyance due to wind turbine noise–a dose–response relationship. *The Journal of the Acoustical Society of America*, Volume 116, Issue 6, doi: 10.1121/1.1815091.

[46] Butterfield C.P., Musial W., Jonkman J. (2007). Overview of offshore wind technology: preprint. *Proceedings of Chinese renewable energy industry association conference* (Shanghai from 31 October to 3 November 2007).

[47] Gipe P. (2004). *Wind power: renewable energy for home, farm, and business*. Chelsea Green Pub Co, White River Junction, Vermont.

[48] Fingersh L, Hand M, Laxson A (2006). Wind turbine design cost and scaling model. *National Renewable Energy Laboratory*, Technical Report, No NREL/TP-500-40566.

[49] L. Fried (2017). GLOBAL WIND STATISTICS 2016. *Global Wind Energy Council*.

[50] INTERNATIONAL ELECTROTECHNICAL COMMISSION (2015). IEC/TS 61400-13: Wind turbine, Part 13: Measurement of mechanical loads, Edition 1.0.

[51] Hauptmann S., Argyriadis K., Capellaro M., Hauptmann S., Kochmann M., Mouzakis F., Rademakers L. and Ristow M. (2009). PROTEST - Deliverable D1: State-of-the-Art-Report. Project: *PROcedures for TESTing and measuring wind energy systems*, ECN Wind Energy, pp. 1-69. Available at http://www.protest-fp7.eu, accessed 20 August 2017.

[52] International Electrotechnical Commission. Available at: http://www.iec.ch/, accessed 20 August 2017

[53] Gasch R., Twele J. (2005) Windkraftanlagen - Grundlagen, Entwurf, Planung und Betrieb. Springer Nature, Berlin, Germany.

[54] Manwell J.F., McGowan J.G. and Rogers A.L. (2002). Wind Energy Explained: Theory, Design and Application, 2nd Edition, Hoboken, New Jersey, USA, John Wiley and Sons.

[55] INTERNATIONAL ELECTROTECHNICAL COMMISSION (2010). IEC 61400-22: Wind turbines – Part 22: Conformity testing and certification, 1st edition.

[56] International Organization for Standardization (2004). ISO/IEC 17000: Conformity assessment -- Vocabulary and general principles, 1st edition.

[57]   International Organization for Standardization (2005). ISO/IEC 17025: General requirements for the competence of testing and calibration laboratories, 2nd edition.

[58]   Woebbeking M., Andreä A., Dombrowski A. (2001). Wind Turbine Certification and Type Certification IEC WT 01: IEC System for Conformity Testing and Certification of Wind Turbines, 2001-04.

[59]   Bezziccheri M., Castellini P., Evangelisti P., Santolini C., Paone N. (2015). Uncertainty associated with strain gauge measurements on wind turbines. *EWEA Annual Event, European Wind Energy Association*, (Paris from 17 to 20 November 2015) abstract available at https://www.ewea.org/annual2015/conference/submit-an-abstract/pdf/2911067515994.pdf.

[60]   INTERNATIONAL ELECTROTECHNICAL COMMISSION (1998). IEC 61400-12: Wind Turbine Generator Systems – Part 12: Wind Turbine Power Performance Testing.

[61]   INTERNATIONAL ELECTROTECHNICAL COMMISSION (2002). IEC 61400-11: Wind Turbine Generator Systems – Part 11: Acoustic Noise Measurement Techniques.

[62]   INTERNATIONAL ELECTROTECHNICAL COMMISSION (2001). IEC 61400-21: Wind Turbine Generator Systems – Part 21: Power Quality Requirements for Grid Connected Wind Turbines.

[63]   INTERNATIONAL ELECTROTECHNICAL COMMISSION (2001). IEC TS 61400-23: Wind Turbine Generator Systems – Part 23: Full Scale Structural Testing of Rotor Blades.

[64]   Germanischer Lloyd Industrial Services GmbH (2010). Guideline for the Certification of Wind Turbines, edition 2010. GmbH, 20457 Hamburg, Germany.

[65]   Cruse T.A. (1997). *Reliability-based mechanical design*. Vanderbilt University, Nashville, Tennessee, Mechanical engineering (Marcel Dekker).

[66]   Ribrant J. (2006). *Reliability Performance and Maintenance—A Survey of Failures in Wind Power Systems*. Master's Thesis, School of Electrical Engineering, KTH Royal Institute of Technology, Stockholm, Sweden.

[67]   Blischke W.R., Karim M.R., Prabhakar Murthy D.N (2011). *Warranty Data Collection and Analysis*. Springer, London, UK.

[68]   Hill R.R., Stinebaugh J.A., Briand D., Benjamin A.S. and Linsday J. (2008). SANDIA REPORT - Wind Turbine Reliability: A Database and Analysis Approach. Prepared by: *Sandia National Laboratories*, Albuquerque, New Mexico 87185 and Livermore, California 94550.

[69]   Tchakoua P., Wamkeue R., Ouhrouche M., Slaoui-Hasnaoui F., Tameghe T.A. and Ekemb G. (2014). Wind Turbine Condition Monitoring: State-

of-the-Art Review, New Trends, and Future Challenges. *Energies 2014*, 7(4), pp. 2595-2630, doi: 10.3390/en7042595.

[70]   Nilsson J. and Bertling L. (2007). Maintenance Management of Wind Power Systems Using Condition Monitoring Systems—Life Cycle Cost Analysis for Two Case Studies. *IEEE Transactions on Energy Conversion*, vol. 22, no. 1, pp. 223-229, doi: 10.1109/TEC.2006.889623.

[71]   Walford, Christopher A. (2006). SANDIA REPORT - Wind turbine reliability: understanding and minimizing wind turbine operation and maintenance costs. Prepared by: *Sandia National Laboratories*, Albuquerque, New Mexico 87185 and Livermore, California 94550, doi: 10.2172/882048.

[72]   IEA-ETSAP and IRENA[©] Technology Brief E07 (2016). Wind Power Technology Brief. Available at: http://www.irena.org/DocumentDownloads/Publications/IRENA-ETSAP_Tech_Brief_Wind_Power_E07.pdf, accessed 20 August.

[73]   Braam H., Obdam T.S., van de Pieterman R.P., Rademakers L.W.M.M. (2011). Properties of the O&M Cost Estimator (OMCE). *Energy Research Centre of the Netherlands*, ZG Petten, the Netherlands.

[74]   IRENA: The International Renewable Energy (2015). Renewable Power Generation Costs in 2014. Abu Dhabi, United Arab Emirates.

[75]   Technical Committee CEN/TC 319 "Maintenance" (2015). Maintenance — Maintenance terminology, prEN 13306.

[76]   Salonen A. (2009). FORMULATION OF MAINTENANCE STRATEGIES. *Mälardalen University Press Licentiate Theses*, No. 100, School of Innovation, Design and Engineering, Printed by Arkitektkopia, Västerås, Sweden.

[77]   Coronado D., Fischer K. (2015). Project Report: CONDITION MONITORING OF WIND TURBINES: STATE OF THE ART, USER EXPERIENCE AND RECOMMENDATIONS. *Fraunhofer Institute for Wind Energy and Energy System Technology IWES Northwest*, Am Seedeich 45, 27572 Bremerhaven, Germany.

[78]   Bloch H. and Geitner F (1983). *Practical Machinery Management for Process Plants: Machinery failure analysis and troubleshooting*, vol. 2, 3rd edition. Gulf Publishing Company, Houston, Texas.

[79]   Wilkinson M., Hendriks B., Spinato F., Gomez E., Bulacio H. and Roca J. (2010). Methodology and Results of the ReliaWind Reliability Field Study. *Proceedings of the Scientific Track of the European Wind Energy Association Conference*, Warsaw, Poland.

[80]   Tavner P.J. (2012). *Offshore Wind Turbines: Reliability, Availability and Maintenance, 1st edition.* IET: The Institution of Engineering and Technology, London.

[81]   Tavner P., Faulstich S., Hahn B. and van Bussel G. J. W. (2010). Reliability & Availability of Wind Turbine Electrical & Electronic

Components. EPE Journal: *European Power Electronics* , vol. 20, issue 4, doi: http://dx.doi.org/10.1080/09398368.2010.11463777.

[82]   Faulstich S., Hahn B. and Tavner P. (2011). Wind turbine downtime and its importance for offshore deployment. *Wind Energy*, vol. 14, pp. 327-337, doi: 10.1002/we.421.

[83]   Crabtree C. J. (2012). Operational and Reliability Analysis of Offshore Wind Farms. *Proceedings of the Scientific Track of the European Wind Energy Association Conference*, Copenhagen, Denmark.

[84]   Spinato F., Tavner P., Van Bussel G. and Koutoulakos E. (2009). Reliability of wind turbine subassemblies. *IET Renewable Power Generation*, vol. 3, no. 4, pp. 387-401, doi: 10.1049/iet-rpg.2008.0060.

[85]   Hahn D.I.B. (1997). Zeitlicher Zusammenhang von Schadenshäufigkeit und Windgeschwindigkeit. *22. FGW-Workshop: Einfluß der Witterung auf Windenergieanlagen*, Institut für Meteorologie, Leipzig.

[86]   Tavner P., Edwards C., Brinkman A. and Spinato F. (2006). Influence of wind speed on wind turbine reliability. *Wind Engineering*, vol. 30, issue 1, pp. 55-72, doi: https://doi.org/10.1260/030952406777641441.

[87]   Tavner P., Xiang J. and Spinato F. (2007). Reliability analysis for wind turbines. *Wind Energy*, vol. 10, pp. 1-18, doi:10.1002/we.204.

[88]   Feng Y., Tavner P. J. and Long H. (2010). Early Experiences with UK Round 1 Offshore Wind Farms. *Proceedings of the Institution of Civil Engineers – Energy*, vol. 163, issue 4, pp. 167-181, doi: https://doi.org/10.1680/ener.2010.163.4.167.

[89]   Crabtree C.J. (2011). *Condition Monitoring Techniques for Wind Turbines*. PhD Theses, Durham University, United Kingdom.

[90]   Wilkinson M., Darnell B., van Delft T. and Harman K. (2014). Comparison of methods for wind turbine condition monitoring with SCADA data. *IET Renewable Power Generation*, vol. 8,no. 4, p. 390-397, doi: 10.1049/iet-rpg.2013.0318.

[91]   Yang W., Tavner P., Crabtree C., Feng Y. and Qiu Y. (2014). Wind turbine condition monitoring: technical and commercial challenges. *Wind Energy*, vol. 17, pp. 673-693, doi:10.1002/we.1508.

[92]   Germanischer Lloyd Industrial Services GmbH (2010). Guideline for the Certification of Condition Monitoring Systems for Wind turbines. GmbH, 20457 Hamburg, Germany.

[93]   A.Greco, S.Sheng, J.Keller, A.Erdemir (2013). Material wear and fatigue in wind turbine Systems. *Wear of Materials*, *Published by Elsevier B.V.*, vol. 302, pp. 1583-1591, doi: https://doi.org/10.1016/j.wear.2013.01.060. Available from: https://www.researchgate.net/publication/256913764_Material_wear _and_fatigue_in_wind_turbine_Systems.

[94]   Beganovic N. and Söffker D. (2016). Structural health management utilization for life time prognosis and advanced control strategy deployment of wind turbines: An overview and outlook concerning

actual methods, tools, and obtained results. *Renewable and Sustainable Energy Reviews*, vol. 64, issue C, pages 68-83.

[95]   Patton R.J., Frank P.M. and Clark R.N. (1989). Fault diagnosis in dynamic systems: theory and application, control engineering series. Englewood Cliffs, NJ: Prentice-Hall.

[96]   Hameed Z., Song Y.S., Cho Y.M., Ahn S.H. and Song C.K. (2009). Condition monitoring and fault detection of wind turbines and related algorithms: a review. *Renewable and Sustainable Energy Reviews*, vol. 13, issue 1, pp. 1-39, doi: https://doi.org/10.1016/j.rser.2007.05.008.

[97]   Nilsson J. and Bertling L. (2007). Maintenance management of wind power systems using condition monitoring systems life cycle cost analysis for two case studies. *IEEE Transactions on Energy Conversion*, vol. 22, no. 1, pp. 223-229, doi: 10.1109/TEC.2006.889623.

[98]   Marquez F.P.G., Tobias A.M., Perez J.M.P. and Papelias M. (2012). Condition monitoring of wind turbines: techniques and methods. Renew Energy, vol. 46, pp.169–78, doi: https://doi.org/10.1016/j.renene.2012.03.003.

[99]   Zaggout Mahmoud Nouh (2013) Wind Turbine Generator Condition Monitoring via the Generator Control Loop. PhD Theses, Durham University, United Kingdom.

[100] Fischer K., Besnard F. and Bertling L. (2012). Reliability-Centered Maintenance for Wind Turbines Based on Statistical Analysis and Practical Experience. IEEE Transactions on Energy Conversion, vol. 27, no. 1, pp. 184-195, doi: 10.1109/TEC.2011.2176129.

[101] Wiggelinkhuizen E.J., Verbruggen T.W., Braam, H., Rademakers L.W.M.M., Xiang J., Watson S., Giebel G., Norton E., Tipluica M.C., MacLean A. (2007). CONMOW: Condition Monitoring for Offshore Wind Farms. *Proceedings of the European Wind Energy Conference* (EWEC2007), (Milan from 7 to 10 May 2007).

[102] IRENA: The International Renewable Energy (2012). *Renewable Energy Technologies: Cost Analysis Series,* Volume 1. Abu Dhabi, United Arab Emirates.

[103] Germanischer Lloyd Industrial Services GmbH (2013). *Guidiline for the Certification of Condition Monitoring Systems for Wind turbines,* edition 2013. GmbH, 20457 Hamburg, Germany.

[104] ISO: Internetional Organizzation for Standardizzation (2002). ISO 13373-1: Condition monitoring and diagnostics of machines -- Vibration condition monitoring -- Part 1: General procedures.

[105] INTERNATIONAL ELECTROTECHNICAL COMMISSION (2010). ISO 614000-25-6: Communication for monitoring and control of wind power plants – Logical note classes and data classes for condition monitoring, 1st edition.

[106]   Fan W. and Qiao P. (2011). Vibration-based Damage Identification Methods: A Review and Comparative Study. *Struct Health Monit*, vol. 10, issue 1, pp 83-111, doi: 10.1177/1475921710365419.

[107]   Shakya P., Darpe A.K. and Kulkarni M.S. (2013). Vibration-based fault diagnosis in rolling element bearings: ranking of various time, frequency and time-frequency domain data-based damage identification parameters. *International Journal of Condition Monitoring*, vol. 3, no. 2, pp. 53–62, doi: 10.1784/204764213808146626.

[108]   Soua S., Van Lieshout P., Perera A., Gan T.H. and Bridge B. (2013). Determination of the combined vibrational and acoustic emission signature of a wind turbine gearbox and generator shaft in service as a prerequisite for effective condition monitoring. *Renew Energy*, vol. 51, pp. 175–181, doi: https://doi.org/10.1016/j.renene.2012.07.004.

[109]   Zhu J., He D. and Bechhoefer E. (2013). Survey of Lubrication Oil Condition Monitoring, Diagnostics, and Prognostics Techniques and Systems. *Journal of Chemical Science and Technology*, vol. 2, no. 3, pp. 110-115.

[110]   Mba D. and Rao R. (2006). Development of Acoustic Emission Technology for Condition Monitoring and Diagnosis of Rotating Machines: Bearings, Pumps, Gearboxes, Engines, and Rotating Structures. *The shock and Vibration Digest*, vol. 38, no. 1, doi: 10.1177/0583102405059054.

[111]   Rolfes R., Tsiapoki S. and Hackell M. (2014). Sensing solutions for assessing and monitoring wind turbines. *Sensor Technologies for Civil Infrastructures,* pp.565-604, doi: 10.1533/9781782422433.2.565.

[112]   Molina C. (2010). *Contributions to the analysis of vibration and acoustic emissions for the condition monitoring of epicyclic gearboxes*. PhD Theses, RWTH Aachen University, Germany.

[113]   Lekou D. (2013). From laboratory to field measurements for wind turbine condition monitoring. WindForce, (Bremerhaven from 4 to 6 June 2013).

[114]   Wei J. and McCarty J. (1993). Acoustic emission evaluation of composite wind turbine blades during fatigue testing. *Wind engineering*, vol. 17, no. 6, pp. 266-274, doi: 10.1016/S0963-8695(97)85542-9.

[115]   Purarjomandlangrudi A. and Nourbakhsh G. (2013). Acoustic emission condition monitoring: an application for wind turbine fault detection. *International Journal of Research in Engineering and Technology*, vol. 2, issue 5, pp. 907–918, doi: 10.15623/ijret.2013.0205031.

[116]   Yang B. and Sun D. (2013). Testing, inspecting and monitoring technologies for wind turbine blades: a survey. *Renewable and Sustainable Energy Reviews*, vol. 22, pp. 515–526, doi: https://doi.org/10.1016/j.rser.2012.12.056.

[117]   Anjar B., Dalberg M. and Uppsall M. (2011). Feasibility study of thermal condition monitoring and condition based maintenance in wind turbines.

[118]   Ralph M. (2009). The continuing story of power plant thermography.

[119]   Yang W., Tavner P., Crabtree C., Feng Y. and Qiu Y. (2014). Wind turbine condition monitoring: technical and commercial challenges. *Wind Energy*, vol. 17, issue 5, pp. 673-393, doi: 10.1002/we.1508.

[120]   Cheng L. and Tian G.Y. (2012). Comparison of Nondestructive Testing Methods on Detection of Delaminations in Composites. *Journal of Sensors*, vol. 2012, Article ID 408437, 7 pages, doi: http://dx.doi.org/10.1155/2012/408437.

[121]   Daneshi-Far Z., Capolino G.A. and Henao H. (2010). Review of failures and condition monitoring in wind turbine generators. *Proceedings of the XIX International Conference on Electrical Machines*, pp. 1-6. (Kuala Lumpur from 29th November to 1st December 2010).

[122]   Barton J.P. and Watson S.J. (2013). Analysis of electrical power data for condition monitoring of a small wind turbine. *IET Renewable Power Generation*, vol. 7, issue 4, pp.341 -349.

[123]   Mohanty A.R. and Kar C. (2006). Fault detection in a multistage gearbox by demodulation of motor current waveform*. IEEE Transactions on Industrial Electronics*, vol. 53, issue 4, pp. 1285-1297, doi: 10.1109/TIE.2006.878303.

[124]   Kar C. and Mohanty A.R. (2006). Multistage gearbox condition monitoring using motor current signature analysis and Kolmogorov – Smirnov test. *Journal of Sound and Vibration*, vol. 290, issues 1-2, pp. 337–368, doi: https://doi.org/10.1016/j.jsv.2005.04.020.

[125]   Kar C. and Mohanty A.R. (2006). Technical note: gearbox health monitoring through multiresolution Fourier transform of vibration and current signals. *Structural Health Monitoring*, 5, issue 2, pp. 195-200, doi: 10.1177/1475921706058002.

[126]   Kar C. and Mohanty A.R. (2008). Vibration and current transient monitoring for gearbox fault detection using multiresolution Fourier transform. *Journal of Sound and Vibration*, vol. 311, issues 1-2, pp. 109-132, doi: https://doi.org/10.1016/j.jsv.2007.08.023.

[127]   Lu B., Li Y., Wu X. and Yang Z. (2009). A review of recent advances in wind turbine condition monitoring and fault diagnosis. *IEEE Conference on Power Electronics and Machines in Wind Applications*, pp. 1-7,

(Lincoln from 24th to 26th June 2009),doi: 10.1109/PEMWA.2009.5208325.

[128] Sheng S., Oyague F. and Butterfield S. (2010). Investigation of Various Wind Turbine Drive Train Condition Monitoring Techniques. *Presented at the 7th International Workshop on Structural Health Monitoring* (Stanford from 9th to 11th September 2009).

[129] Dempsey P. and Sheng D. (2013). Investigation of data fusion applied to health monitoring of wind turbine drivetrain components. *Wind Energy*, vol. 16, issue 4, p. 479-489, doi: 10.1002/we.1512.

[130] Perišić N., Kirkegaard P.H. and Pedersen B.J. (2015). Cost-effective shaft torque observer for condition monitoring of wind turbines. *Wind Energy*, vol. 18, issue 1, pp 1–19, doi: 10.1002/we.1678.

[131] Hackly C. and Schechnery K. (2010). Non-ideal feedforward torque control of wind turbines: Impacts on annual energy production & gross earnings. *Journal of Physics: Conference Series, vol.* 753, pp. 1-10, doi: https://doi.org/10.1088/1742-6596/753/11/112010.

[132] Yang W., Tavner P.J., Crabtree C.J., Feng Y. and Qiu Y (2014). Wind turbine condition monitoring: technical and commercial challenges. *Wind Energy*, vol. 17, issue 5, pp. 673-693, doi: 10.1002/we.1508.

[133] Soker H., Kieselhorst S. and Royo R. (2004). Load monitoring on a mainshaft: A case study. *Proceedings of the German Wind Energy Conference DEWEK*, (Stadthalle Wilhelmshaven from 20th to 21st October 2004).

[134] Yang W., Tavner P.J., Crabtree C.J. and Wilkinson M. (2010). Cost-Effective Condition Monitoring for Wind Turbines. *IEEE Transactions on Industrial Electronics*, vol. 57, issue 1, pp. 263-271, doi: 10.1109/TIE.2009.2032202.

[135] Abdusamad K.B., Gao D.W. and Li Y. (2014). Condition Monitoring System of wind generators based on the effect of electrical torque pulsations and generator temperature. IEEE Symposium on Power Electronics and Machines for Wind and Water Applications, pp. 1-8, (Milwaukee from 24th to 26th July 2014), doi: 10.1109/PEMWA.2014.6912222.

[136] Djurović, S., Vilchis-Rodriguez, D.S., Smith, A.C. (2012). Vibration Monitoring for Wound Rotor Induction Machine Winding Fault Detection. *Proceedings of XXth International Conference on Electrical Machines*, pp. 1906-1912, (Marseille from 2nd to 5th September 2012), doi: 10.1109/ICElMach.2012.6350142.

[137] Wilkinson M.R., Spinato F., Tavner P.J. (2007). Condition Monitoring of Generators & Other Subassemblies in Wind Turbine Drive Trains. *Proceedings of 2007 IEEE International Symposium on Diagnostics for*

Electric Machines, Power Electronics and Drives, pp. 388-392, (Cracow from 6th to 8th September 2007), doi: 10.1109/DEMPED.2007.4393125.

[138] PTB: Messen, Forschen, Wissen. Weltweit größte Anlage für Drehmomentkalibrierungen. Available at: http://www.ptb.de/cms/index.php?id=2447, accessed 20 August 2017.

[139] Kalinin V., Leigh A., Stopps A. and Artigao E. (2013). Resonant SAW Torque Sensor for Wind Turbines. *2013 Joint European Frequency and Time Forum & International Frequency Control Symposium (EFTF/IFC) Joint UFFC*, pp. 462-465, (Prague from 21st to 25th July 2013) doi: 10.1109/EFTF-IFC.2013.6702093.

[140] Nawaz F. and Jeoti V. (2014). SAW sensor read range limitations and perspectives. *Wireless Networks*, vol. 20, issue 8, pp. 2581–2587.

[141] Zappalà D., Bezziccheri M., Crabtree C.J. and Paone N. (2017). Non-intrusive torque measurement for rotating shafts using optical sensing of zebra-tapes. Under review

[142] Seidlitz S., Kuether R.J. and Allen M.S. (2016). Experimental approach to compare noise floors of various torsional vibration sensors. *Experimental Techniques*, vol. 40, issue 2, pp. 661-675, doi: 10.1111/ext.12113.

[143] Janssens K., Van Vlierberghe P., D'Hondt P., Martens T., Peeters B. and Claes W. (2011). Zebra tape butt joint algorithm for torsional vibrations. *Proceedings of the Society for Experimental Mechanics Inc.*, vol. 3, pp 213-224, (New York from 1st to 4th February 2010), doi: 10.1007/978-1-4419-9834-7_19.

[144] INTERNATIONAL ELECTROTECHNICAL COMMISSION (2001). IEC/TS 61400-13: Wind turbine generator systems, Part 13: Measurement of mechanical loads, Edition 1.0.

[145] Hoffmann K. (2001) *Applying the Wheatstone bridge circuit*, Hottinger Baldwin Messtechnik Company, Germany.

[146] Bruhn O., Soeker H., Grapentin M., Braam H., Mouzakis F., Petersen S.M., Kleinselbeck T. and Oiz Vasquez A. (2006). MEASNET LOADS – Commenting IEC Dash-13. *Presented at the 8th German Wind Energy Conference, DEWEK2006* (Bremen from 22nd to 23rd November 2006); also presented at Dewi Magazine no. 31, 2007.

[147] Holierhoek J.G., Korterink H., van de Pieterman R.P., Braam H., Rademakers L.W.M.M., Lekou D.J., Hecquet T. and Söker H (2010). PROTEST - Recommended Practices for Measuring in Situ the 'Loads' on Drive Train, Pitch System and Yaw System. *ECN Wind Energy*, pp. 1-81. Available at http://www.protest-fp7.eu, accessed 20 August 2017.

[148]   Lekou D.J. and Mouzakis F. (2009). WT load measurement uncertainty: load-based versus analytical strain-gauge calibration method. *J. Sol. Energy Eng*, vol. 131, issue 1, doi:10.1115/1.3027508.

[149]   Montero W., Farag R., Diaz V., Ramirez M. and Boada (2010). Uncertainties associated with strain gauge-measuring systems using resistance strain gauges. *The Journal of Strain Analysis for Engineering* Design, vol. 46, issue 1, doi: 10.1243/03093247JSA661.

[150]   Tianwei X. and Zuoxia X. (2013). Study on Testing Method of Mechanical Load of Blade Root. Presented at the 6th China Wind Power Conference, (Beijing from 16th to 18th October 2013).

[151]   Nazar Ul Islam Muhammad, Cheng P. and Oelmann B. (2016). Method of torque measurement based on volumetric strain. *Proceedings of 55th Annual Conference of the Society of Instrument and Control Engineers of Japan (SICE)*, pp. 116-123 (Tsukuba from 20th to 23rd September 2016), doi: 10.1109/SICE.2016.7749205.

[152]   de Silva C.W. (2015). *Sensors and Actuators: Engineering System Instrumentation, 2nd edition.* Boca Raton, Florida, Stati Uniti, CRC Press Taylor & Francis Group.

[153]   Ente Nazionale Italiano di Unificazione (1998). UNI 10478-4: Prove non distruttive: Controllo mediante estensimetri elettrici a resistenza - Circuiti di misura, elaborazione e presentazione dei risultati.

[154]   HBM - Electrical Connection of Force Transducers. Available at: https://www.hbm.com/en/4248/electrical-connection-of-force-transducers/, accessed 20 August 2017.

[155]   Klosse R., Soker H. (2008). Investigations on Cross Talk Analysis for Rotor Blade Bending Measurements. *Presented at the 9th German Wind Energy Conference* (Bremen from 26th to 27th November 2008); also presented at Dewi Magazine no. 33, 2008.

[156]   Bezziccheri M., Castellini P., Evangelisti P., Santolini C. and Paone N. (2017). Measurement of mechanical loads in large wind turbines: problems on calibration of strain gage bridges and analysis of uncertainty. *Wind Energy,* pp. 1–14, doi: https://doi.org/10.1002/we.2136.

[157]   INTERNATIONAL ORGANIZATION FOR STANDARDIZATION (2008). ISO/IEC Guide 98-3:2008 Uncertainty of measurement -- Part 3: Guide to the expression of uncertainty in measurement.

[158]   Doebelin E.O. (2003). *Measurement systems: application and design*. New York, McGraw Hill.

[159]   Morfiadakis E., Papadopoulos K., Seifert H., van der Borg N. and Petersen S.M. Assessment of Wind Turbine Load Measurement

Instrumentation. *Proceedings of European Wind energy conference*, pp. 675-678 (Nice from 1st to 5th March 1999).

[160] Tropea C. and Yarin A.L. (2007). Springer Handbook of Experimental Fluid Mechanics, vol. 1. Berlin, Springer-Verlag.

[161] American Society of Mechanical Engineers (2007). ASME B31.1a – 2008: Addenda to ASME B31.1 - 2007.

[162] van Millingen R.D. and van Millingen J.D. (1991). Phase shift torquemeters for gas turbine development and monitoring. *Proceedings ASME International Gas Turbine and Aeroengine Congress and Exposition,* vol. 5 (Orlando from 3rd to 6th June), doi: doi:10.1115/91-GT-189.

[163] Petek J. and Hamilton P. (2005). *Performance monitoring for gas turbines*. *Orbit, vol.* 25, pp. 65-74.

[164] Vath A. and Grimm S. (2015). Reliability and energy yield increase of wind turbines as a benefit of dynamic load reduction operation. *Proceedings Scientific Track of the European Wind Energy Association Conference* (Paris from 17th to 20th November 2015).

[165] Soong W. and Ertugrul N. (2002). Field-weakening performance of interior permanent-magnet motors. *Conference Record of the 2000 IEEE Industry Applications Conference: Thirty-Fifth IAS Annual Meeting and World Conference on Industrial Applications of Electrical Energy*, vol. 1, pp. 416-423, doi: 10.1109/IAS.2000.881144.

[166] Boyer F., Porez M. and Khalil W. (2006). Macro-continuous computed torque algorithm for a three-dimensional eel-like robot. *IEEE Transactions on Robotics*, vol. 22, no. 4, pp. 763-775, doi: 10.1109/TRO.2006.875492.

[167] Austin C. and Rojon I. (2014). *Ship performance management: The comprehensive guide to monitoring and measurement.* Windsor, Fathom.

[168] Fleming W.J. (1982). Automotive torque measurement: a summary of seven different methods. *Proceedings 32nd IEEE Vehicular Technology Conference*, pp. 71-78, doi: 10.1109/VTC.1982.1623003.

[169] Guy B. (2015). Measurement and traceability of torque on large mechanical drives. *Proceedings AMA Conferences - SENSOR 2015 and IRS2 2015,* pp. 44-45 (Nuremberg from 19th 21th May 2015).

[170] Cichowicz J., Gerasimos T. and Dracos V. (2015). Dynamic energy modelling for ship life-cycle performance assessment. Ocean Engineering, vol. 110, pp. 49-61, doi: https://doi.org/10.1016/j.oceaneng.2015.05.041.

[171] Lee K.E., Kim J.W., Kim C.Y. and Ahn S.H. (2009). Development of micro torque measurement device using strain gauge. *Proceedings IEEE*

International Symposium on Assembly and Manufacturing (ISAM), pp. 101–106 (Seoul, Korea, 17-20 November 2009), doi: 10.1109/ISAM.2009.5376923.

[172] Shams S., Lee J.Y. and Han C. (2012). Compact and lightweight optical torque sensor for robots with increased range. *Sensors and Actuators A: Physical,* vol. 173, issue 1, pp. 81-89, doi: https://doi.org/10.1016/j.sna.2011.10.019.

[173] Hazelden R.J. (1993). Optical torque sensor for automotive steering systems. *Sensors and Actuators A: Physical, vol.* 37–38, pp. 193-197, doi: https://doi.org/10.1016/0924-4247(93)80033-D.

[174] Wilmshurst T.H., Rothberg S.J. and Halliwell N.A. (1991). Laser torquemeter: a new instrument. *Electronics Letters*, vol. 27, issue 2, pp. 186-187, doi: 10.1049/el:19910119.

[175] Tullis I.D.C., Halliwell N.A. and Rothberg S.J. (1996). Laser torquemeter: effects of axial shaft vibration. *Proceedings SPIE 2868 - The International Society for Optical Engineering, Second International Conference on Vibration Measurements by Laser Techniques: Advances and Applications*, vol. 2868, pp. 449-457 (Ancona 23 September 1996), doi: 10.1117/12.248668.

[176] Tullis I.D.C., Halliwell N.A. and Rothberg S.J. (1998). Shaft tilt sensitivity of the laser torquemeter. *Proceedings SPIE - The International Society for Optical Engineering, Third International Conference on: Vibration Measurements by Laser Techniques: Advances and Applications, vol. 3411, pp. 309-316 (Ancona from 16th to 19th June 1998)*, doi: 10.1117/12.307714.

[177] Garinei A. and Marsili R. (2017). Development of a non-contact torque transducer based on the laser speckle contrast method. *Journal of Sensors and Sensor Systems,* vol. 6, pp. 253-258, doi: https://doi.org/10.5194/jsss-6-253-2017.

[178] Hajdu F. and Horváth P. (2012). Contactless torque sensor development. *Acta Technica Jaurinensis,* vol. 5, issue 2, pp. 115-120.

[179] Angleviel D., Frachon D. and Masson G. (2006). Development of a contactless hall effect torque sensor for electric power steering. *Proceedings SAE 2006 Automotive Dynamics Stability and Controls Conference and Exhibition*, (Novi from 14th to 16th February 2006), doi: 10.4271/2006-01-0939.

[180] Friswel M.I., Penny J.E.T., Garvey S.D. and Lees A.W. (2010). *Dynamics of rotating machines,* Cambridge University Press.

[181] Sue P., Wilson D., Farr L. and Kretschmar A. (2012). High precision torque measurement on a rotating load coupling for power generation

operations. *Proceedings IEEE International Instrumentation and Measurement Technology Conference,* pp. 518-523 (Graz, from 13th to 16th May 2012), doi: 10.1109/I2MTC.2012.6229149.

[182] Janssens K. and Britte L. (2014). Comparison of torsional vibration measurement techniques. *Advances in Condition Monitoring of Machinery in Non-Stationary Operations* Springer, pp. 453–463, doi: https://doi.org/10.1007/978-3-642-39348-8_39.

[183] Vishay Semiconductors Application of Optical Reflex Sensors Document Number 80107, 02-02. Available at: http://www.vishay.com/docs/80107/80107.pdf, accessed 20 August 2017.

[184] INTERNATIONAL ORGANIZATION FOR STANDARDIZATION (2008). ISO/IEC 2008 Guide 98-3:2008/Suppl.1:2008 Uncertainty of measurement - Part 3: Guide to the expression of uncertainty in measurement (GUM:1995) – Supplement 1: Propagation of distributions using a Monte Carlo method.

[185] UNI EN 20286-1:1995, ISO System of limits and fits. Bases of tolerances, deviations and fits.

[186] Oppenheim A.V., Schafer R. W. and Buck J. R. (1999). Discrete-Time Signal Processing, New Jersey, Upper Saddle River, Prentice Hall.

[187] Joint Committee for Guides in Metrology (JCM) (2013). Evaluation of measurement data - Guide to the expression of uncertainty in measurement and supplements, Editor. 2013. *Committee for Guides in Metrology*, Bureau International des Poids et Mesures (BIPM): Sèvres, France. Available at http://www.bipm.org/en/publications/guides/gum.html, accessed 20 August 2017.

[188] Kaloterakis N. (2010). How It Works: The Next-Gen Wind Turbine. Available at: http://www.popsci.com/technology/article/2010-03/next-gen-wind-turbine, accessed 20 August 2017.

[189] Main-Shaft of Wind Turbine. Available at: https://www.alibaba.com/product-detail/Main-Shaft-of-Wind-Turbine_218865845.html, accessed 20 August 2017.